Allowable Wind Turbine Set-down Impact

R. T. Blom

Master of Science Thesis
Delft University of Technology

TU Delft

Allowable Wind Turbine Set-down Impact

by

R. T. Blom

to obtain the degree of Master of Science
at the Delft University of Technology,
to be defended publicly on Wednesday August 24, 2022 at 14:00.

Student number:	5147115	
Thesis duration:	December 6, 2021 – August 24, 2022	
Thesis committee:	Prof. dr. A. V. Metrikine,	TU Delft, committee chairman
	Dr. P. C. Meijers,	TU Delft, supervisor
	M. Kraan,	Heerema Marine Contractors, supervisor

This thesis is confidential and cannot be made public until August 24, 2024.

An electronic version of this thesis is available at `http://repository.tudelft.nl/`.

TU Delft

Preface

Three years ago, after successfully finishing my bachelor of science in mechanical engineering (Hanzehogeschool university of applied sciences in Groningen), I decided to pursue the ambition of obtaining the master's degree in 'Offshore and Dredging Engineering' at the TU Delft. It turned out to be a rather eventful three years, on top of which the Covid-19 pandemic forced me to follow the majority of my master online from home. Nonetheless, I completed all courses, and the past nine months I have been working on this thesis in fulfilment of the master's degree. The past nine months have been very interesting, and where I sometimes struggled to determine the right approach, most of the time I made good progress. By keep on working, and with the help of brainstorming with my supervisors, I managed to confidently complete this thesis, which marks the end of my student career.

I would like to speak out my sincere gratitude to Marcel Kraan, my company supervisor from Heerema Marine Contractors, as he proved always willing to help by exchanging ideas and providing constructive criticism. This undoubtedly contributed to the progress made. Approximately every three weeks I met with Marcel and Maarten veldhuizen to discuss the progress made and to discuss their view on my research. Maarten, although not my day-to-day supervisor, provided me with feedback from a project engineering point of view. This often resulted in a refreshing perspective on the challenges I faced, and for this I would like to thank him. Peter Meijers, my supervisor from the TU Delft, was always available to provide me with in-depth technical knowledge. When I ran into difficulties, Peter was always available for a brainstorm session, and after I walked out of his office, my head was full of ideas and solutions for the problems with which I arrived. For this, I am very grateful to Peter. At last, I would like to thank Prof. Andrei Metrikine, my graduation professor (and graduation committee chairman), for his constructive feedback and expertise during the progress meetings with the graduation committee. Particularly on a higher level, his feedback resulted in some fundamental change in direction during the graduation, which would without, presumably, have resulted in a lesser quality of this thesis. I really enjoyed my time studying at TU Delft, and also the past nine months working on my thesis in cooperation with Heerema Marine Contractors have been great. It was a pleasure.

R. T. Blom
Delft, August 2022

Abstract

The increased awareness of the negative consequences of man-made climate change has given rise to a fast growing offshore wind industry. Wind turbines become increasingly larger, and available locations for offshore wind farms are shifting towards deeper waters, where jack-up vessels can no longer be used for installation. Heerema Marine Contractors is planning to install pre-assembled wind turbine generators (WTGs) with the semi-submersible crane vessel 'Thialf'. During installation, the set-down stage is a critical phase in which the WTG is placed on top of the substructure. Due to uncontrollable motions in the WTG (caused by ship motions and wind loads), a significant impact can occur, which can cause considerable loads at the interface between WTG and substructure. The objective of this research is to determine the allowable impact ensuring sufficient structural integrity. The allowable impact is most conveniently expressed in the kinematic parameters impact speed V_i and oblique impact angle α.

Based on structural integrity analysis, two requirements are formulated; occurring stresses in the system shall not exceed the yield stress, and the RNA accelerations are limited to 1.5 g. In order to relate the impact kinematics (V_i and α) to the occurring stresses and accelerations, an impact model is constructed. A special case describes the collinear impact, in which $\alpha = 0°$. The WTG tower and substructure are modelled as rods describing the axial motions. The applicability of the collinear case is limited, as a zero oblique angle is improbable. Yet, this collinear case provides insights in stress wave reflections and system parameter influence. The oblique case appends the classical rod with a classical beam describing transverse motions. The model simulates the oblique impact by imposing a bending moment and shear force at the interface. A contact model is created to approximate the contact stresses at the interface and the force eccentricity which determines the imposed moment.

The results obtained for the collinear case, which are successfully cross-checked with a FEM model, demonstrate that a superposition of incident waves and reflections can result in maximum stresses about three times higher than the induced stress at the interface. The induced stress at the interface is approximately linear proportional to the impact speed V_i. The oblique case shows increasing maximum stresses for increasing oblique angle, as the imposed moment results in bending stresses adding up to the axial stresses. The contact model shows significantly higher stresses than the global model. By including an elementary material damping model, considerably lower stresses are obtained, emphasizing the importance of material damping. Regarding the stress requirement, the contact model approximates an allowable impact speed V_i of 0.47 m/s for the largest possible oblique angle. It is demonstrated that the maximum RNA acceleration requirement imposes even more stringent allowable impact velocity: for the maximum oblique angle, the allowable impact speed V_i is 0.09 m/s.

The constructed models provide approximations of stresses and accelerations in the WTG and substructure. Due to several underlying assumptions, particularly the one-way coupling simplification, it is unfortunately not concluded that the oblique impact model yields conservative stress approximations. Hence, it is recommended for successive research to improve the contact model. Considering the approximated allowable impact speed V_i of 0.43 m/s limited by the yield requirement, the acceleration-limited allowable impact speed V_i of 0.09 m/s shows that RNA accelerations currently limit the impact. Hence, acceleration mitigation in the RNA could allow for significantly higher impact speeds, enlarging the operational window.

Contents

Nomenclature

Abbreviations

Abbreviation	Definition
ALS	accidental limit state
COG	center of gravity
DNV	Det Norske Veritas
DOF	degree of freedom
EN	European Norm
EOM	equation of motion
FDM	finite difference method
FEM	finite element method
FLS	fatigue limit state
HC	heave compensation
HMC	Heerema Marine Contractors
IEA	International Energy Agency
KV	Kelvin-Voight
LCOE	levelized cost of energy
LLT	lower lifting tool
LRFD	load and resistance factor design
LS1	plastic limit state
LS3	buckling limit state
NORSOK	the Norwegian shelf's competitive position
ODE	ordinary differential equation
OWF	offshore wind farm
PDE	partial differential equation
PS	port-side
RL	Rayleigh-Love
RNA	rotor nacelle assembly
SCF	stress concentration factor
SLS	serviceability limit state
SSCV	semi-submersible crane vessel
T&I	transport and installation
ULS	ultimate limit state
USF	upper stabilising frame
WSD	working stress design
WTG	wind turbine generator

Symbols

Symbol	Definition	Value	Unit
A	cross-sectional area		m^2
A_c	contact area		m^2
b	sagitta of a circle segment		m
c_0	wave speed of steel		$\mathrm{m\,s}^{-1}$
c_s	soil damping		$\mathrm{N\,s\,m}^{-1}$
D	pile or tubular outer diameter		m

Symbol	Definition	Value	Unit
D_{top}	diameter of WTG tower at the top		m
dt	time step size		s
dx	spatial step size		m
E	Young's modulus of steel	210×10^9	$\mathrm{N\,m^{-2}}$
e	FEM element		-
F	force		N
$f_{Love\,theory}$	Rayleigh-Love theory frequency limit		$\mathrm{s^{-1}}$
$f_{wave\,equation}$	classical rod theory frequency limit		$\mathrm{s^{-1}}$
g	gravitation	9.81	$\mathrm{m\,s^{-2}}$
G_s	soil shear modulus		$\mathrm{N\,m^{-2}}$
I	area moment of inertia		$\mathrm{m^4}$
J	polar moment of inertia		$\mathrm{m^4}$
k_{LLT}	cable stiffness of lower lifting tool cables		$\mathrm{N\,m^{-1}}$
k_s	soil stiffness		$\mathrm{N\,m^{-1}}$
L	combined height of substructure and WTG tower		m
L_1	WTG tower height		m
L_2	substructure height		m
M	moment		N m
m_{RNA}	RNA mass		kg
N	total number of discrete nodes		-
P	shear force at the interface		N
r	radius		m
R	tubular outer radius		m
R_e	contact area centroid eccentricity		m
$R_{e,e}$	indentation volume centroid eccentricity		m
$r_{g,p}$	polar radius of gyration		m
S	arc length of circle		m
t	time		s
th	substructure and WTG tower wall thickness at the interface		m
u	displacement in axial x-direction		m
v	displacement in transverse y-direction		m
V_i	impact speed of WTG		$\mathrm{m\,s^{-1}}$
x	longitudinal or axial direction coordinate		-
y	transverse direction coordinate		-
Z	pile impedance		$\mathrm{kg\,s^{-1}}$
z	contact model maximum vertical indentation		m
α	oblique angle		rad
β	indentation angle		rad
γ	wavenumber		$\mathrm{rad\,m^{-1}}$
Δ	discrete differential element		-
ε	strain		-
ζ	Laplace transform coefficient		$\mathrm{s\,m^{-1}}$
η	material viscosity		$\mathrm{N\,s\,m^{-1}}$
θ	central angle of a circle		rad
λ	wavelength		m
ν	Poisson's ratio		-
ξ	viscous damping ratio		-
ρ	density		$\mathrm{kg\,m^{-3}}$
σ	stress		$\mathrm{N\,m^{-2}}$
ψ	yaw motion		rad
ω	angular frequency		$\mathrm{rad\,s^{-1}}$

List of Figures

List of Tables

1

Introduction

As climate change and global warming are increasingly considered a real threat to life on earth, alternative, greener energy sources have gained interest. Offshore wind is one of the most popular sources, as it has several benefits compared to solutions on land, for example, the scarcity of available land for onshore wind. Other advantages are less visual- and noise disturbance, and the higher average wind speed at sea. The offshore wind industry has made significant steps the past 10 years, both technologically and economically. This enormous momentum caused the levelized cost of energy (LCOE) to drop, and the turbines to become increasingly bigger. According to the International Energy Agency (2021), this trend will not attenuate any time soon, and they expect the growth in offshore wind installed power to be higher than ever the coming five years. In 2010 the average rated power of an installed offshore wind turbine was around 3 MW, in 2020 this number had already grown to over 8 MW (Ramirez et al., 2020). According to Musial et al. (2021), the three biggest turbine manufacturers, Vestas, General Electric and Siemens Gamesa, all have announced turbines with a rated power between 12 and 15 MW to be installed in 2024.

On top of the increasing turbine size, the growing demand for offshore wind farms (OWF's) results in the need to go to deeper waters for available space (Soares-Ramos et al., 2020). This trend is shown in Figure 1.1. Conventionally, the installation of fixed offshore wind turbine generators (WTG's) is done with jack-up vessels that have their limitations such as water depth, seabed stability or crane capacity. All these limitations and the shift towards deeper waters, therefore, causes installation using floating vessels to be increasingly competitive, and potentially the only option for some projects. Also, heavier cranes will be required to install both the turbine and its substructure.

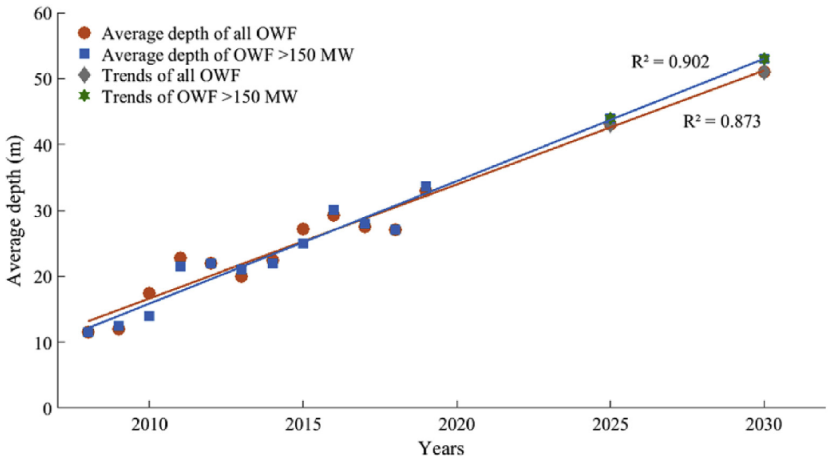

Figure 1.1: Trend of offshore wind farms being located in increasingly deeper waters (Soares-Ramos et al., 2020).

Heavy lifting is where Heerema Marine Contractors (HMC), operator of large crane vessels, excels. Hence, this upcoming market, floating installation of heavy turbines or in deeper waters , would offer

great opportunity for HMC. HMC's core business has for the biggest part of its history been heavy lifting in the offshore environment. HMC operates the biggest crane vessels in the world, with a lifting capacity of 7100 and 10000 tonnes per crane for their vessels 'Thialf' and 'Sleipnir' respectively. Considering this, the market opportunity for HMC lies in the big turbines or substructures for which such heavy cranes would be required, and locations where floating vessels are the only option. Using a floating vessel, however, has the drawback that ship motions will (directly and/or indirectly) cause motions of the WTG when it is lifted by the crane. HMC is planning to install pre-assembled WTG's using the semi-submersible crane vessel (SSCV) Thialf. The tower and rotor nacelle assembly (RNA) are lifted in one piece, after which it is installed onto the fixed substructure. An impression of this single lift operation is shown in Figure 1.2. During the set-down stage of the installation, these motions, together with the wind loading and set-down speed of the WTG in the crane, result in an impact at the interface between the substructure and the WTG. The moment of impact is called 'touch-down'. The touch-down stage is defined as the time interval in which the WTG lands on the fixed substructure and usually lasts less than a second.

Figure 1.2: 17 MW WTG single lift installation impression (Heerema Marine Contractors, 2021).

1.1. Offshore wind turbine installation

The WTG is to be installed with one of the two 7100 mT cranes of the SSCV Thialf. In order to provide sufficient height clearance, a so called 'delta-jib' is installed on the crane. The WTG is assembled on a dedicated frame on the port side (PS) of the vessel. The assembling consists of combining tower segments, adding the nacelle and, finally, installing the blades. Figure 1.3 presents a schematic of the Thialf positioning a pre-assembled WTG above the substructure.

First, the global set-down configuration is presented. An overview of the rigging arrangement, how and where the pre-assembled WTG is lifted, is depicted in Figure 1.4. In this figure, the WTG is already positioned above the transition piece, ready for touch-down.

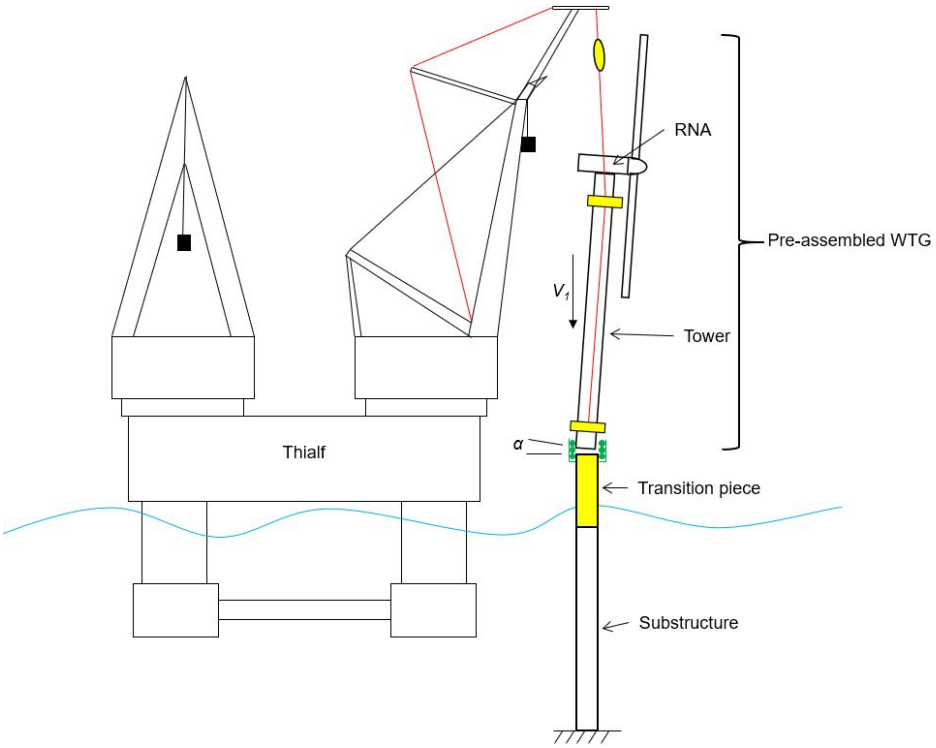

Figure 1.3: Schematic of WTG installation with SSCV Thialf.

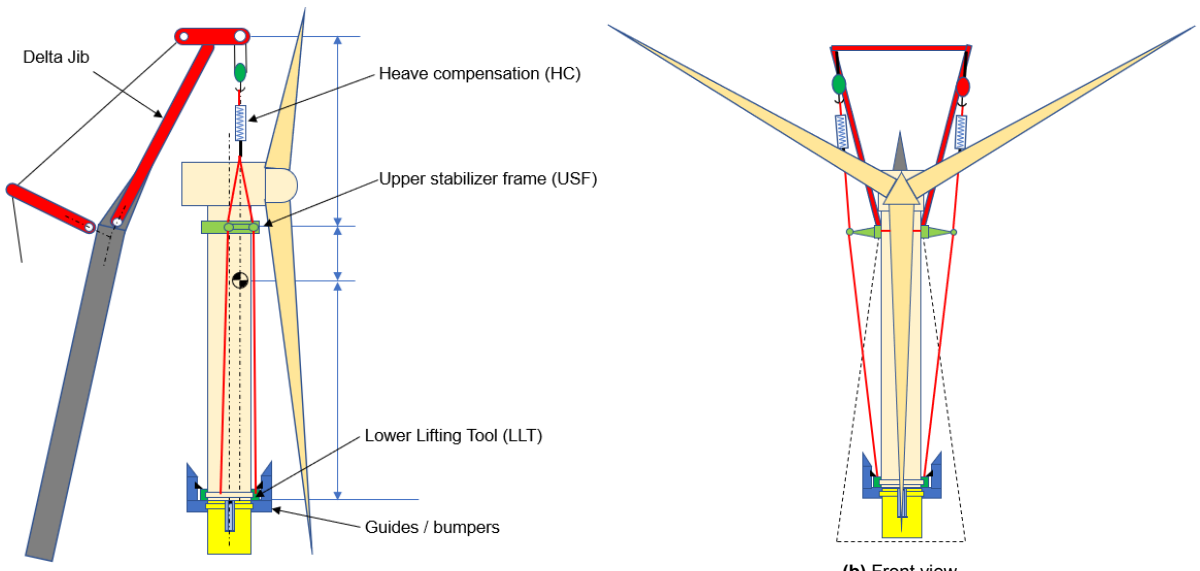

(a) Side view.

(b) Front view.

Figure 1.4: Rigging arrangement schematic (Heerema Marine Contractors, 2021).

As can be observed in Figure 1.4, a heave compensation (HC) system is included in the rigging of the WTG. This, together with inertia and stiffnesses in the cable itself, causes the WTG to not behave like a 'free falling mass' when impacting the substructure. This means that upon touch-down, some part of the mass will be impacting and some will still be completely lifted by the crane. For the *initial* ($t = 0$) impact however, the stress wave magnitude that is induced is independent of mass, as will be explained in chapter 2. Therefore this stiffness in the lift arrangement is not relevant for the stress magnitude induced by the impact, although it can influence the shape and length of the induced stress wave. Furthermore, it affects the WTG's dynamics during and after touch-down, and it influences stress wave reflections.

Moreover, the HC system reduces the heave motion, thus influencing the vertical velocity of the system. Therefore, the HC system is an essential coupling between WTG set-down speed, and crane set-down speed and crane tip heave motion. Hence, the HC system is of importance for the translation from acceptable impact to acceptable ship motions (indirectly sea state). Besides the HC system, also the location where the weight of the WTG is lifted matters. The purpose of this arrangement is to lift the total weight at the lower lifting tool (LLT). For these reasons, the rigging arrangement will be considered in this thesis.

Two separate impact cases will be distinguished, the 'collinear impact' and the 'oblique impact'. The difference between these two cases is that the collinear impact assumes that the WTG's cross-section will impact the substructure perfectly horizontal. In other words, the WTG- and substructure's centerline are both parallel and coinciding. This means that the impact surface will be equal to the cross-sectional surface at the interface, so that the full cross-sectional area participates equally in the impact. For the oblique case, the WTG will impact the substructure under an angle, referred to as the 'oblique angle', denoted α. This oblique impact is what in reality will happen, yet the collinear impact model proves helpful as an intermediate step towards the oblique impact model. This will be further explained in chapter 2. One could also consider the collinear impact to be a special case of the oblique impact, assuming the oblique angle to be zero. Both impact cases are illustrated in Figure 1.5. The exact geometry of the flange at the interface, which is simplified in this figure, is presented in section A.2.

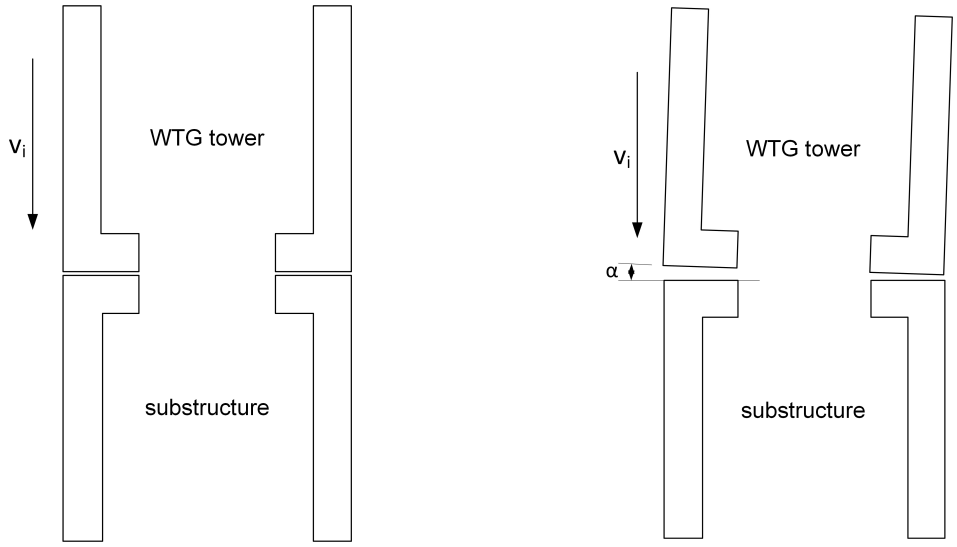

(a) Collinear impact. **(b)** Oblique impact.

Figure 1.5: The two impact cases under consideration, with V_i representing the impact velocity and α the oblique angle.

Taking a closer look at the interface, the local (interface-oriented) set-down configuration will be identified. At the interface, a guide and bumper system will be in place aiming to remove the following degrees of freedom (DOF); surge x, sway y and yaw ψ. These notations and signs are in correspondence with the conventions presented in Figure 1.6. The translational DOF's, surge and sway, are blocked by simply obstructing these motions with the use of guides and bumpers. The yaw DOF is blocked by lining up the bolt holes using pins or something similar. The restriction of these DOF's only holds close to the interface, and the RNA and most part of the WTG tower are not restricted in these directions. Moreover, with only two rotational DOF's remaining, these could always be replaced by one single rotation around a new axis. Consequently, the motion of the WTG close to the interface can be described by one translation, in heave direction, and one rotation, being described by the oblique angle α. Figure 1.7 illustrates the guides and bumper system in blue.

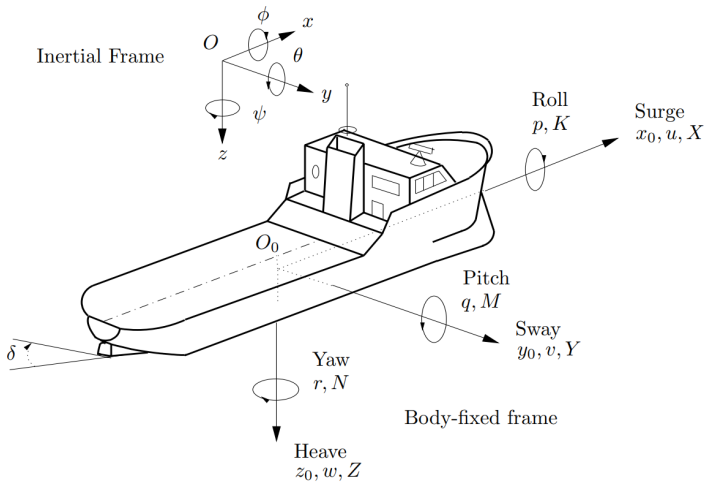

Figure 1.6: Standard notation and sign conventions for ship motions (SNAME, 1950).

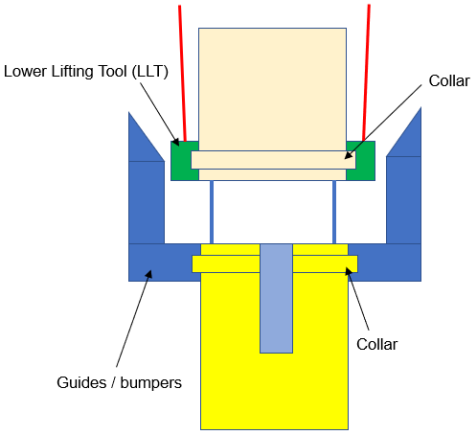

Figure 1.7: WTG set-down guides & bumpers (Heerema Marine Contractors, 2021).

Another point of attention is the positioning tolerance, which is defined by the bolt-hole tolerance. This tolerance ensures sufficient clearance for the bolts so that they can be installed without problems. The line-up guiding system will be used to remain within this tolerance. Considering the time window of this thesis, this positioning tolerance will not be taken into account.

1.1.1. Components

The system as just discussed consists of multiple components; the WTG tower, the RNA, and the substructure. The WTG tower will be connected to the substructure by a bolted flange connection. As the area of interest is focused on the interface, the geometry of these flanges is of importance, predominantly for the local effects. Several types of flanges are commonly used in the industry, but for this thesis one type will be assumed. The geometry of this type of flange can be found in Appendix A.

For the substructure, a monopile is the assumed type. As monopiles are the most common substructure type for offshore wind turbines, this assumption is considered reasonable. For the induced impact, another substructure like a jacket would give similar results, as the flange remains similar. However, the stress wave propagation and reflections will differ significantly in a jacket.

Following the trend of wind turbines becoming increasingly bigger, it is decided to assume a 17 MW turbine for this thesis. As such a big turbine is not yet on the market, HMC designed a reference turbine which basically is extrapolated from existing designs with lower rated power. The dimensions and other properties are presented in Appendix A.

1.2. Problem statement

The set-down stage of the turbine is a critical step during the floating installation of bottom-founded offshore wind turbines. An important criterion in this stage is the acceptability of the landing loads, from now on referred to as impact loads. These loads are to be quantified by analysing the interaction between the impacting surfaces, and the global interaction between WTG and substructure. The allowable impact, defined by this analysis and the structural integrity requirements, is the problem under consideration in this thesis. The impact load is affected by various system components and parameters, such as ship motions, rigging, motions of the lifted load (WTG), component stiffness, oblique angle and set-down speed. Taking all of these different aspects fully into account in a single model, results in an overly elaborate model and complicated calculation. An acceptance criterion that is convenient to employ in global installation analysis models, in order to determine for example the workability of the single lift installation, is desired. Workability in this context is defined as the fraction of time the operation can be executed compared to the available installation time. Aspects that influence the workability are, for instance, sea state and the vessel's sea-keeping capabilities.

The objective of the research into this problem is to determine a convenient-to-check acceptance criterion that defines acceptable touch-down impact of the WTG installation on a fixed substructure. A model will be developed to analyse the impact loads and the corresponding structural response during this stage. This model will form the backbone for the acceptance criterion, which has to ensure sufficient structural integrity. The methodology of the model needs to be sufficiently generic such that it can be applied for different component geometries (like a tapered WTG tower, or variable wall thickness over the height), and variable oblique angle and set-down speed.

As the allowable impact heavily determines the workability of the WTG installation operation, it is clear that this subject is of significant importance for HMC's ability to competitively install wind turbines. By enabling HMC to efficiently meet the growing demand for installation of offshore wind farms, this thesis has the potential to contribute to the renewable energy transition. HMC has green ambitions and want to do their part, and this thesis contributes to live up to those ambitions.

Prior to the formulation of the research question and sub-questions, additional demarcations are defined below:

- The focus within this thesis lies on the acceptance criterion only. The consequences of the acceptance criterion on the workability of the vessel are not within the main scope of this research. However, a rough qualitative estimate of these consequences is of added value to the research by means of investigating the stringency of the limits the criterion imposes on the workability. The acceptance criterion is defined in cooperation with the end users, such as marine engineers who calculate workability, to ensure the practical usefulness of the criterion.
- The focus in this thesis is on the loads and structural integrity near the interface. This is referred to as 'local', or 'contact'. The order of magnitude of the demarcation that is considered close to the interface is meters, which is considered small compared to tower and substructure height. However, also the response of the complete substructure and WTG are considered, as that could in fact potentially be limiting the allowable impact. This is referred to as 'global'. The distance order of magnitude of the global effects is hundreds of meters.
- When deemed necessary, the semi-submersible crane vessel 'Thialf' is assumed to be the installation vessel, and the 'Heerema 17 MW turbine' is considered to be the reference turbine of this research.
- Vertical set-down impact is assumed. The guides and bumper system as discussed earlier will ensure this. Therefore it is not possible for the WTG to accidentally impact the transition piece from the side.
- The structural integrity forms the starting point in this research. Based on structural integrity requirements, allowable impact is determined. This allowable impact defines an allowable sea state for the WTG set-down operation. Often such impact analyses are done in reverse direction of determination, so that a certain sea state and environmental conditions define the impact, and the impact determines the effects on the structural integrity.

1.3. Research question

Arising from the problem statement and the research objective, the main research question is formulated as:

"During WTG-substructure touch-down, what is a convenient-to-check acceptance criterion for the landing loads that ensures sufficient structural integrity of the impacting structures?"

The main research question is divided into the following, more specific sub-questions:

1. ***What are the structural integrity requirements of WTG and substructure during set-down?***
2. ***How can the impact and the impacting structures be modelled?***
3. ***How can impact-induced stresses on critical locations be determined?***
4. ***What are the best parameters in which to express the acceptance criterion, and that is convenient to determine critical ship dynamics?***

These sub-questions provide guidance in the process of finding answers to the main research question. The strategy on how to answer these questions will be discussed below.

1.4. Research strategy

The strategy to arrive at a model that effectively and accurately predicts acceptance criteria is discussed. This model needs to describe sufficiently accurate the relation between impact and impact-induced effects, particularly stress. There are two distinct types of knowledge required to answer the research question. The first is that about the modelling of an impact. The other is the determination of structural integrity requirements as these determine the allowable impact. The translation from structural integrity requirements to allowable impact is the purpose of the constructed model. First, the existing knowledge about these subjects is gathered and reviewed in chapter 2 and chapter 3, respectively about impact modelling and structural integrity requirements. The goal of this literature review is to determine the knowledge gap between existing and required knowledge to answer the research question. When this gap is identified, the next step is to perform the research required to bridge the gap. The strategy for this research is explained now.

An important part of the research will be the model that describes the collinear impact. This model will prove valuable as basis for the oblique impact model. In this collinear impact model, several rigorous assumptions are made. These are; no oblique angle ($\alpha = 0°$, see Figure 1.5), and the stress concentrations due to the flange's geometry are not considered. Especially the first assumption is expected to be far from reality. Consequently, this collinear impact model is not expected to represent reality, where a non-zero oblique impact will govern, yet it proves valuable as a starting point in the work towards the more realistic oblique impact model. On top of that, the influence on the occurring stresses of several effects such as; lateral inertia, variable cross-sectional area and boundary conditions can be investigated rather conveniently. The foreseen method of validating the oblique impact with is the Finite Element Method (FEM). A FEM model will be constructed to compare results with those obtained from the collinear impact model. This allows for cross-checking obtained results from both FEM and the collinear impact model in order to increase confidence. Numerous theories that can describe stress wave propagation in continuums, such as the one-dimensional rod theory, are rather convenient to describe axi-symmetric impact with. Several such models are discussed extensively in chapter 2. Some of these result in quite elegant analytical solutions for stress wave magnitude and propagation. The oblique angle, and the reason why it will be non-zero in reality, has already been discussed in chapter 1. In order to proceed towards the more realistic oblique impact model, two functionalities need to be added to the collinear impact model. These are; the inclusion of oblique-impact-imposed bending and shear at the interface, and the ability to approximate the contact indentation stress due to the oblique impact. An approach on how to incorporate these is presented per functionality.

The first functionality is the inclusion of bending and shear at the interface, imposed by the oblique impact. A bending moment will be imposed due to the fact that an oblique impact inherently results in an net force eccentricity with respect to the centroid of the tubular's cross-sectional area, with which the net force at the interface acts on substructure and WTG. This will significantly affect the global response

of the system. In order to include this bending and shear, a model that is able to describe bending and shear is required. Several such models are discussed and compared in section 2.1, based on which a decision is made of which model is used.

Apart from the global modelling of the oblique impact, the peak stresses at the contact region need to be determined. This contact problem requires another approach. Due to the oblique impact, the contact area and stress at the interface between both impacting structures vary with the indentation. Because the contact area will increase during the initial impact, contact stresses will decrease rapidly, where they initially can be very high. As it is not possible to describe this contact stresses in the global model as described earlier, a distinct contact model needs to be established. This ability to relate the impact to contact stresses is the other functionality the model needs to entail, in order to approximate contact indentation stresses. In order to validate the results from the contact model, FEM analyses are executed, providing results to compare with those obtained from the oblique impact model.

1.5. Thesis structure

The thesis will continue with reviewing the existing knowledge about impact modelling and structural integrity requirements in chapter 2 and chapter 3 respectively. Subsequently, chapter 4 provides the collinear impact model, which forms the basis for, and is succeeded by the oblique impact model as presented in chapter 5. Finally, the conclusion and recommendation are respectively presented in chapter 6 and chapter 7, which contain the answer to the research question and recommendations for subsequent research following from findings in this thesis .

2

State of the art impact modelling

The problem statement, as discussed in chapter 1, is an impact problem in which particularly the transient response is of interest. The existing scientific knowledge about these kind of impacts is studied, together with other topics that are relevant for this research. The main findings are presented and discussed in this chapter. The employed strategy in this literature review is to try to find answers to the research question and sub-questions as much as possible. Both value and limitations for the context of this research are discussed for the gathered knowledge, and finally, the information that is lacking in order to answer the research question is identified, referred to as the 'knowledge gap'. The research to be performed in this thesis will fill this gap, enabling answering the research question.

The chapter starts with discussing several ways of modelling the system, the impact load and other effects that occur in impact problems (section 2.1 & section 2.2). Thereafter, the material characteristics of steel enduring impact loads are discussed in section 2.3. Potential stress concentrations in geometrical details close to the flange are examined in section 2.4, and finally the literature gap is identified in section 2.5. This last section also contains a conclusion about which knowledge will be used for the research, and based on what that choice is made.

2.1. Impact modelling

Extensive research is done into modelling of impact loads on a pile in the context of impact pile driving. A similarity between impact pile driving and flange on flange impact during touch-down can be found in the impact load, where the substructure is the 'pile' and the WTG is the 'ram'. However, it should be noted that the WTG has a height in the order of 100 m, whereas that of a ram will be in the order of just a couple of meters. One important difference is that in most impact pile driving models additional components are added in between the ram and the pile, such as a cushion or anvil. Another difference is that in the context of impact pile driving, one-dimensional models are often deemed sufficient given the nature of the goal of the models. The goal in impact pile driving is to penetrate the pile into the soil. This is often done by impacting the pile with the ram, which causes a stress wave to be initiated which propagates trough the pile from top to bottom, where the stress wave needs to overcome the soil resistance in order to displace the pile into the soil (Deeks and Randolph, 1993). Hence, the longitudinal stress wave effects on a system scale are of main interest in impact pile driving. Effects in the pile itself, apart from the induced stress not exceeding the yield stress, are often not considered in impact pile driving literature (Smith, 1960).

Impact pile driving models are a specific case of impact models, but more generic theories exist that are useful for impact analyses. In fact, most impact pile driving models are based on theories such as the one-dimensional wave equation. The field of 'structural dynamics' covers various theories that describe structural vibrations. Another example of a theory that could be of use for this research is the transverse vibrating Euler-Bernoulli beam model, which describes lateral vibrations of a structural beam element. These kind of theories will prove themselves very useful in this research. A variety of useful theories are discussed in this section, in approximate order of increasing complexity.

2.1.1. Rigid body ram impact

In impact pile driving, the ram of the hammer is often considered a rigid body. A simple starting point in modelling the WTG and substructure could be to consider the WTG as a rigid ram. These kind of models are studied widely, and Deeks provided a convenient overview of several such models (Deeks and Randolph, 1993). All these models are one-dimensional, and the difference lies in the actual representation of the pile, cushion and anvil. Figure 2.1 provides an overview of the model representations discussed in the aforementioned paper. The simplest model is that of the ram, directly impacting the pile head (Figure 2.1 - a).

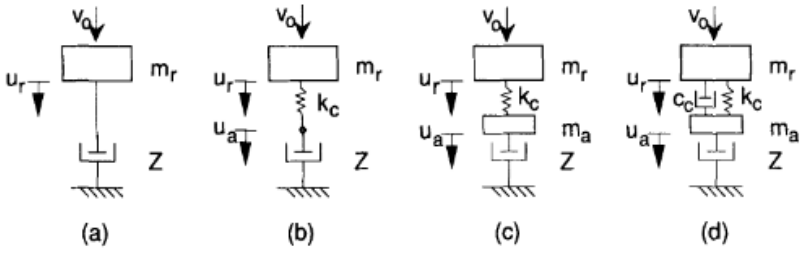

Figure 2.1: Analytical pile hammer models (Deeks and Randolph, 1993).

In this case, the impedance of the pile is given as

$$Z = \rho c_0 A, \qquad \text{with} \qquad c_0 = \sqrt{\frac{E}{\rho}}, \tag{2.1}$$

in which E is the pile material Young's modulus, ρ is the pile material density, A is the cross-sectional area of impact and c_0 is the stress wave speed (i.e. speed of sound) of the pile material. The impedance of the pile represents the energy transport by stress waves away from the impact location. The impedance can be modelled as a dashpot, and the magnitude of the force induced by the impact is given by:

$$F = Z\,V, \tag{2.2}$$

$$F\,(t) = Z\,V\,e^{\left(\frac{-Zt}{M}\right)}, \tag{2.3}$$

in which V is the impact speed, M is the mass of the ram in kg, and t is the time. Equation 2.3 describes the force as a function of time, whereas Equation 2.2 only gives the initial ($t = 0$) force amplitude.

The assumption of a rigid body ram is justified in the case that there is a cushion with a much lower stiffness compared to the ram and pile, but in absence of this cushion, it is not (Parola, 1970). Therefore, concerning the context of a WTG impacting a substructure, this rigid body assumption is an important limitation. Equation 2.2 forms in this sense an upper bound of the force, representing the case in which the ram stiffness is infinitely high, and this expression can readily be derived from the one-dimensional wave equation, as will be shown in subsection 2.1.2. Also this rigid body assumption for the ram, without cushion, would lead to the peak force occurring at the instance of the impact, which is not the case for an elastic ram. Due to stiffness and inertia of the ram, cushion, anvil and pile, the force is not introduced instantaneous but rather gradually.

2.1.2. Classical rod theory - longitudinal vibrations

The classical rod theory analytically describes the axial motions in a rod, based on the one-dimensional wave equation (Graff, 1975). Both impacting bodies, the WTG and substructure, can be modelled as elastic, one-dimensional rods. Using this rod theory, the induced stress wave could be determined. Advantage of the rod theory is that it considers the bodies as continuum materials, instead of spatially

discretized elements. The book 'Wave motion in elastic solids' from Graff (1975) is consulted in this subsection, and equations are, unless stated otherwise, based on it. The wave equation is written as

$$\frac{\partial^2 u}{\partial x^2} = \frac{1}{c_0^2}\frac{\partial^2 u}{\partial t^2}, \tag{2.4}$$

of which the widely known D'Alembert solution is

$$u\left(x,t\right) = f\left(x - c_0 t\right) + g\left(x + c_0 t\right), \tag{2.5}$$

in which u is the displacement in x-direction, c_0 is the stress wave speed, x is the longitudinal direction and f and g are arbitrary wave functions. The occurring stress resulting from the strains in the rod is related to the solution by Hooke's Law, assuming linear elastic regime, in which f' is the x-derivative of f. The stress reads:

$$\sigma\left(x,t\right) = E\frac{\partial u}{\partial x} = Ef'(x - c_0 t). \tag{2.6}$$

Note that Equation 2.6 describes exclusively the stress caused by the wave propagation in positive x-direction and yet without any reflections. In the case of a moving rod longitudinally impacting a fixed rod (or stationary semi-infinite), the magnitude of the induced stress wave can be analytically derived using the corresponding initial conditions, and is described by

$$\sigma_0 = -\frac{1}{1 + \frac{\rho_2 c_2}{\rho_1 c_1}}\rho_2 c_2 V_1. \tag{2.7}$$

This impact is shown schematically in Figure 2.2 where subscript 1 and 2 respectively represent the impacting rod with velocity V_1 and the fixed rod. Subscript 0 represents 'induced', hence, σ_0 is the induced stress magnitude. For the case in which a rigid body longitudinally impacts a fixed or stationary rod, this equation is reduced to Equation 2.2 as discussed in subsection 2.1.1, with the trivial difference of a factor A between force and stress.

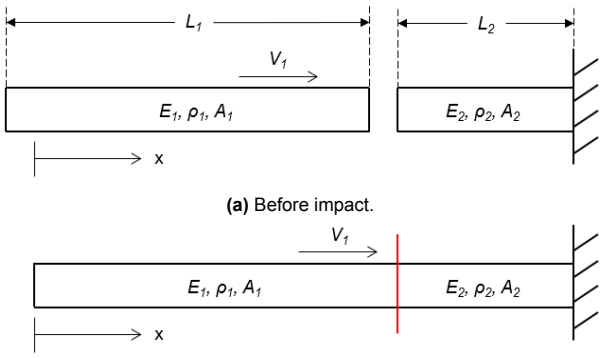

(a) Before impact.

(b) Instance of impact (t = 0), the red line indicates the interface.

Figure 2.2: Collinear impact against a fixed rod.

For the case in which the impedance of both impacting bodies is equal, Equation 2.7 reduces to

$$\sigma_0 = -\frac{1}{2}\rho_2 c_2 V_1. \tag{2.8}$$

The length of the induced stress wave, λ, is determined by the length of the impacting rod L_1 as follows:

$$\lambda = 2L_1. \tag{2.9}$$

The question remains how accurate it is to approach the substructure or the WTG-tower as a rod.

According to Kolsky (1964), for very long wave lengths, a hollow cylinder behaves as a rod, and for very short wave lengths, it behaves as a plate. In this context, 'long' and 'short' is with respect to the diameter of the cylindrical structure. The order of magnitude of the height of the WTG tower is around 100 m, thus $\lambda \approx 200$ m, and that of the diameter is around 8 m. Therefore, it is justified to consider the substructure and WTG-tower (i.e. a hollow cylinder) as a rod. This obviously only holds for axial motions.

Another point of interest is the reflection of waves at the boundaries. In reality, the bottom of the substructure is not completely fixed and some damping takes place in the soil. Also the substructure does not necessarily have a constant cross-section over the height, which can also cause reflection of waves. Nevertheless, assuming the bottom boundary as fixed is conservative. A fully fixed end will always fully reflect the incident compressive wave as a compressive wave in opposite direction. Because both incident and reflected wave are compressive, a superposition of incident and reflected wave will increase the stress. Assuming a completely fixed boundary, stresses during superposition are double the magnitude of the incident wave. This only holds assuming that there is no wave dispersion nor energy dissipation.

Until now, a constant cross-sectional area is assumed in deriving relations for the rod theory. The theory can, however, also describe rods with a variable cross-sectional area. The equation of motion assuming x-dependent cross-sectional area reads:

$$\rho A(x)\frac{\partial^2 u(x)}{\partial t^2} - \frac{\partial}{\partial x}\left(EA(x)\frac{\partial u(x)}{\partial x}\right) = 0. \tag{2.10}$$

It should be noted that for this equation of motion, the D'alembert solution is not valid anymore, as this equation of motion now yields a dispersive system. Including a tapered geometry for the WTG tower or substructure, or varying the wall thickness over the height, both are realistic to represent the WTG and substructure more accurately. A variable cross-sectional area results in a continuous junction for the stress wave. A discrete junction is presented in Figure 2.3.

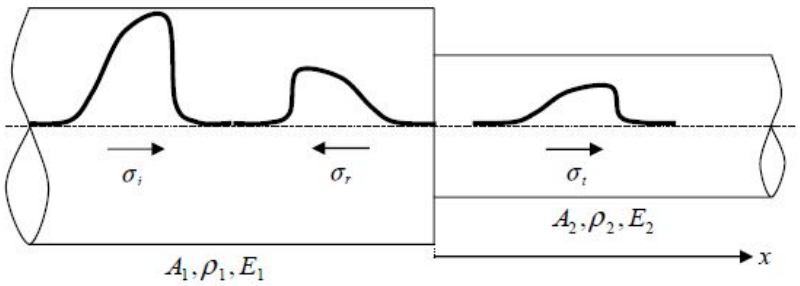

Figure 2.3: Incident, reflected and transmitted stress waves at the junction of two rods. Figure obtained from Metrikine and Vrouwenvelder (2018), based on the figure presented in Graff (1975).

Considering the figure, subscript 1 and 2 respectively represent the left and right rod. The incident stress wave is propagating from the left to the right rod. σ_i represents the incident, σ_r the reflected and σ_t the transmitted stress wave. In Graff (1975), the following relations between incident, reflected and transmitted stress waves are derived assuming equal material properties for both the left and right rod:

$$\sigma_t = \frac{2}{1 + Z_2/Z_1}\sigma_i, \tag{2.11}$$

$$\sigma_r = \frac{Z_2/Z_1 - 1}{1 + Z_2/Z_1}\sigma_i. \tag{2.12}$$

From these relations, effects of the variable area on the stress wave propagation can be determined.

2.1.3. Mass-spring elements in series

In the 1950s and 60s, E.A.L. Smith proposed a numerical solution for the one-dimensional stress wave propagation through a pile, represented by distributed mass and springs in series (Smith, 1950, 1960). Figure 2.4 shows the pile as represented by mass-spring elements. This models discretizes both the spatial and time variable where the time-step is dt and the spatial step, one mass-spring element, is dx. Smith's model is based on the one-dimensional wave equation, making it logical to lead to similar stresses as rod theory in subsection 2.1.2. Similar, not equal, because Smith's model is numerical in nature whereas the induced stress wave magnitude in rod theory is derived analytically. The advantage of Smith's model compared to the rod theory, is that its numerical approximation allows for non-linear spring- and dash-pot characteristics. This makes Smith's model very suitable for pile-driving applications.

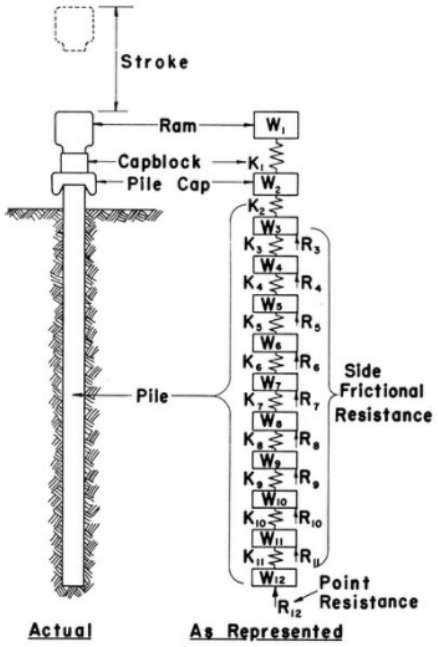

Figure 2.4: Ram and pile represented as mass-spring elements (Smith, 1960).

A significant limitation of this model is that it does not allow for lateral inertia effects. In reality, longitudinal strains will also cause lateral strains for materials with a non-zero Poisson's ratio (Graff, 1975). This coupling between longitudinal and lateral strain is known as the Poisson's effect.

Another difficulty is obtaining the time at which the maximum force occurs. Since the initial (before any reflections) maximum force will be at the interface in this model, the time at which it occurs decreases proportional to the size of dt and dx. This means that, when making the spatial element size smaller to get more accurate data, the time at which the peak force takes place also decreases. In the limit of infinitely many elements, the time goes to zero. This does not correspond with reality, where it takes at least non-zero time after impact for the maximum force to develop. In other words, the induced stress wave does not have a perfect rectangular block shape. It should be noted, however, that this limitation (the dependency of the force development at the instance of impact on the numerical discretization) also holds for the classical rod theory when solved using numerical methods.

2.1.4. Rayleigh-Love rod theory

Until now, any lateral strain effects are disregarded, but in reality, lateral strain is coupled to longitudinal strain by the Poisson's ratio. For steel the Poisson's ratio is $\nu \approx 0.3$. Consequently, these lateral strains caused by axial strains could have significant impact on the shape of the stress wave. The Rayleigh-Love rod theory presents the governing equation which includes these lateral strains (Graff, 1975). Based on Hooke's law, the relation between lateral and axial strains is given by

$$\varepsilon_x = \frac{1}{E}\left(\sigma_x - \nu\left(\sigma_y + \sigma_z\right)\right), \tag{2.13}$$

$$\sigma_x = \frac{E}{(1+\nu)(1-2\nu)}\left((1-\nu)\,\varepsilon_x + \nu\left(\varepsilon_y + \varepsilon_z\right)\right), \tag{2.14}$$

in which subscript x represents the axial, and y and z both lateral directions. The Rayleigh-Love rod equation of motion reads

$$\frac{\partial^2 u}{\partial x^2} = \frac{1}{c_0^2}\frac{\partial^2}{\partial t^2}\left(u - \frac{\nu^2 J}{A}\frac{\partial^2 u}{\partial x^2}\right), \tag{2.15}$$

where ν is the Poisson's ratio, and J is the polar moment of inertia, $J = Ar_{g,p}^2$, with $r_{g,p}$ being the polar radius of gyration of the cross section. It is important to note that, because this equation now includes a dispersive term, the D'Alembert solution does not hold anymore. Consequently, the aforementioned

expression for σ, Equation 2.8, is not valid for this governing equation. The expression for the stress including the lateral inertia from the Rayleigh-Love theory reads

$$\sigma = E\frac{\partial u}{\partial x} + \underbrace{\rho\nu^2\frac{J}{A}\frac{\partial^3 u}{\partial x \partial t^2}}_{Lateral\ inertia}. \tag{2.16}$$

In order to determine the influence of lateral inertia on the dispersion, let us assume a solution to be in the form of

$$u\left(x,t\right) = Ce^{i(\omega t - \gamma x)}, \tag{2.17}$$

in which ω is the frequency, C is an unknown constant and γ is the wavenumber, given by $\gamma = 2\pi\lambda^{-1}$. Substituting this solution in Equation 2.15 gives the dispersion equation

$$-\omega^2 + c_0^2\gamma^2 - a^2\omega^2\gamma^2 = 0, \qquad with \qquad a^2 = \frac{\nu^2 J}{A}, \tag{2.18}$$

$$\omega^2 = \frac{c_0^2\gamma^2}{1 + a^2\gamma^2}, \tag{2.19}$$

with the limit for increasing wavenumber

$$\lim_{\gamma\to\infty}\omega^2 = \frac{c_0^2}{a^2}. \tag{2.20}$$

This relation represents the frequency upper bound that this governing equation can still describe. Figure 2.5 shows the dispersion relation for Love's theory, classical rod theory (also referred to as wave equation) and exact theory[1]. One can see that for normalized γ, ($\bar{\gamma} = r_{g,p}\nu\gamma$) ≤ 2, Love's theory approximates the exact theory quite well. For much larger values of $\bar{\gamma}$, the theory diverges from exact theory. The wave equation approaches exact theory only for $\bar{\gamma} \leq 0.3$. Assuming some realistic values for the geometry of the tubular WTG tower ($c_0 \approx 5200$ m/s, $\nu = 0.3$, outer diameter $D_o = 8$ m, and wall thickness $th = 75$ mm), the following frequencies can be calculated for the wave equation and Love's theory. These frequencies indicate an approximate upper bound for which both theories still correspond reasonably well with the exact theory.

$$f_{Wave\ equation}(\bar{\gamma} = 0.3) \approx 1400\,Hz, \tag{2.21}$$

$$f_{Love\ theory}(\bar{\gamma} = 2) \approx 540\,Hz. \tag{2.22}$$

[1] According to Graff (1975), exact theory for various structures, such as rods and plates, results from applying the equations of elasticity. It is also stated that "whilst having the virtue of exactness, they are often quite complicated". Therefore it is often solely used to function as reference for an approximate theory, as illustrated in Figure 2.5.

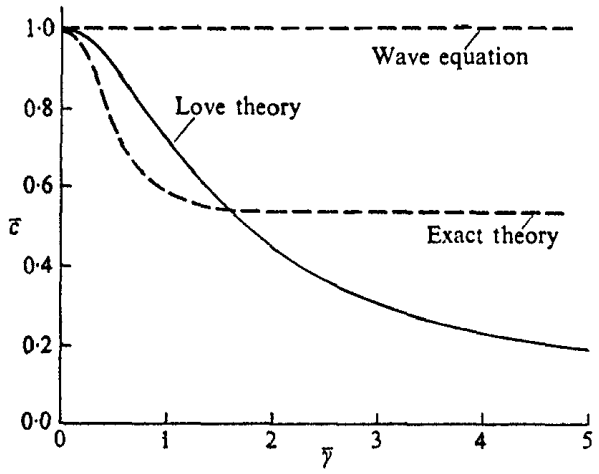

Figure 2.5: Dispersion curve for Love's rod theory, wherein radial-inertia effects are included (Graff, 1975).

As now the order of magnitude of these frequencies is determined, they can be compared to the excitation frequencies to determine whether these frequencies are accurately described by the wave equation and Rayleigh-Love's theory. One frequency that is excited is the 'fundamental' frequency (Achenbach, 1975). This is the frequency of the entire impact-induced stress wave. As mentioned before, this wave length will be in the order of 200 m. This wavelength corresponds to around 26 Hz, well below the accuracy limit of both theories.

2.1.5. Beam theory - transverse vibrations

The main difference between beam and rod theory is that beam theory considers motions in transverse direction y rather than longitudinal direction x. This enables the beam to describe transverse motions resulting from bending moments (Graff, 1975). The simplest beam theory is the Euler-Bernoulli beam theory (also referred to as classical beam theory). In contrast to the wave-equation-based classical rod theory, the beam theory yields a dispersive system. Just as for rod theory, equations and derivations for beam theory presented here are based on the book from Graff (1975), unless stated otherwise. A beam element is shown in Figure 2.6.

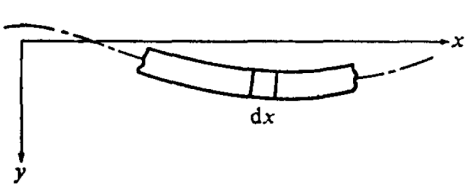

(a) Beam undergoing transverse motion.

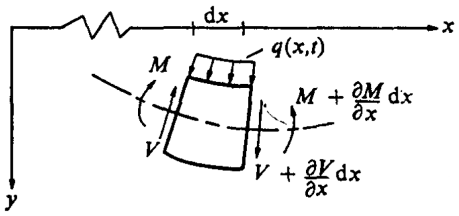

(b) Element of beam subjected to various loads.

Figure 2.6: Beam element (Graff, 1975).

Assuming constant cross section A and constant density ρ, the equation describing the transverse motions of the beam reads

$$\frac{\partial^4 y}{\partial x^4} + \frac{1}{a^2}\frac{\partial^2 y}{\partial t^2} = q(x,t), \qquad with \qquad a^2 = \frac{EI}{\rho A}, \tag{2.23}$$

in which y is the transverse direction, x the longitudinal direction, I the area moment of inertia of the beam and $q(x,t)$ is the external loading. In the context of this research, beam theory is only relevant for the oblique impact. Due to the absence of bending moments and shear forces in the collinear impact, no transverse motions will occur apart from lateral inertia effects as discussed in the previous section. A beam model that includes lateral inertia, is known as 'Rayleigh beam theory'. This equation of motion expands to

$$EI\frac{\partial^4 y}{\partial x^4} + \rho A\frac{\partial^2 y}{\partial t^2} - \rho I_y \frac{\partial^4 y}{\partial x^2 \partial t^2} = 0. \tag{2.24}$$

The relevance of a beam model in the oblique impact model is its ability to include bending of the tower and substructure. The oblique impact will, per definition, impose a moment at the interface of the impact. The axial force induced during the impact acts at some contact area, such that the resultant force acts on a non-zero distance from the neutral line of the tubular section (tower or substructure as a beam). This eccentricity between resultant force and neutral line of the 'beam' imposes a moment. This moment will affect the net stresses proportionally to how it is distributed along the cross-section. An Euler-Bernoulli beam assumes linear moment-induced stress distribution along the cross-section. Using this assumption, the bending stress is written as

$$\sigma_b = \frac{Mr}{I}, \tag{2.25}$$

in which M is the moment, r the distance from the neutral line to the location of interest and I the area moment of inertia of the beam's cross-section. In the case of the tubular section, the maximum and minimum stress occurs at both $r = R$ and $r = -R$, with R being the outer radius of the tubular section.

2.1.6. Coupled longitudinal and transverse motions

In order to describe both the longitudinal and transverse motions in one model, they need to be coupled. One way to do this is by simply coupling the two dimensions, u and v (v is the displacement in transverse direction y), at the interface by introducing interface conditions. In this way, the equations of motion for the rod and the beam remain independent, apart from being coupled at the interface. For the oblique impact, the force in x-direction that is introduced at the interface following from the longitudinal equation of motion can be coupled to the moment that will then be introduced at the interface, described by the transverse equation of motion. This relation is established via the eccentricity between force and neutral axis of the tubular section.

Another method of coupling longitudinal and transverse motions is by deriving coupled equations of motion. These are derived in the book 'Nonlinear and stochastic dynamics of compliant offshore structures' from Han and Benaroya (2002). The coupled equations of motion for longitudinal and transverse motion are, respectively

$$\rho A\frac{\partial^2 u}{\partial t^2} - \frac{\partial}{\partial x}\left(EA\left(\frac{\partial u}{\partial x} + \frac{1}{2}\left(\frac{\partial v}{\partial x}\right)^2\right)\right) = p, \tag{2.26}$$

$$\rho A\frac{\partial^2 v}{\partial t^2} - \frac{\partial}{\partial x}\left(EA\frac{\partial v}{\partial x}\left(\frac{\partial u}{\partial x} + \frac{1}{2}\left(\frac{\partial v}{\partial x}\right)^2\right)\right) - \rho I\frac{\partial^4 v}{\partial x^2 \partial t^2} + EI\frac{\partial^4 v}{\partial x^4} = f, \tag{2.27}$$

in which p and f are the external forcing terms respectively in axial and transverse direction. A schematic of the system described by the equations of motion is shown in Figure 2.7.

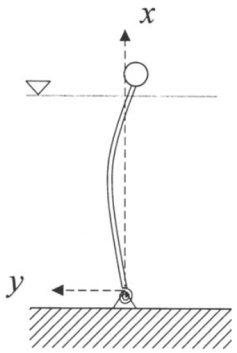

Figure 2.7: Beam with transverse and longitudinal degrees of freedom (Han and Benaroya, 2002).

In the book it is explained that the coupling between longitudinal and transverse motion becomes increasingly relevant with increasing slenderness ratio (the ratio of the length to the radius of gyration of the cross-section). According to Han and Benaroya (2002), a slenderness ratio higher than 100 is considered large. The slenderness ratio of the WTG tower would be in the order of 35 to 70[2], hence not particularly large. Another assumption is, quoting Han and Benaroya (2002): "It is assumed that strains are small but the rotation is moderate compared to the strain so that the equations of motion for the axial and transverse motions are non-linearly coupled".

The fundamental difference between these two methods of combining axial and transverse motions is that the first solely couples them at the interface, where it's equations of motion remain uncoupled. The second method consists of coupled equations of motions, so that the coupling is intrinsic. Considering the slenderness ratio order of magnitude, and the significantly increased complexity of the coupled equations of motion, it is concluded that the method of coupling longitudinal and transverse vibrations solely using the interface conditions will be employed in the oblique impact model.

2.1.7. Shell theory

A more sophisticated theory that can represent a hollow cylindrical structure, is the shell theory. Figure 2.8 indicates a typical section of a cylindrical membrane shell. According to Meijers et al. (2018), modelling of a hollow cylinder as a shell is justified when the structure's length and radius, and the wavelength of the impact-induced stress waves are large compared to the wall thickness. The 'membrane theory of shells' is the general shell theory with some specific assumptions. It assumes torsional and bending moments on an element to be negligible small, so that they are disregarded. Consequently, only forces, normal and shear acting in the mid surface of the shell element are considered, as can be observed in Figure 2.8b.

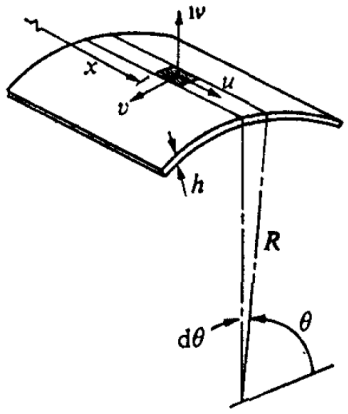

(a) Section from cylindrical membrane shell.

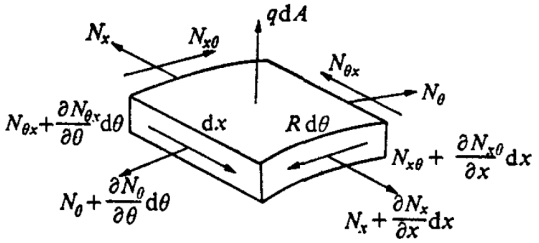

(b) Differential element of shell.

Figure 2.8: Cylindrical membrane shell (Graff, 1975).

Assuming a membrane, the equations of motions for this shell in the longitudinal, tangential and radial directions read, respectively (Graff, 1975)

$$\frac{\partial^2 u}{\partial x^2}+\frac{\nu}{R}\left(\frac{\partial w}{\partial x}+\frac{\partial^2 v}{\partial x \partial \theta}\right)+\frac{(1-\nu)}{2R}\left(\frac{\partial^2 v}{\partial \theta \partial x}+\frac{1}{R}\frac{\partial^2 u}{\partial \theta^2}\right)=\frac{\rho\left(1-\nu^2\right)}{E}\frac{\partial^2 u}{\partial t^2}, \tag{2.28a}$$

$$\frac{1}{R}\left(\frac{1}{R}\frac{\partial w}{\partial \theta}+\frac{1}{R}\frac{\partial^2 v}{\partial \theta^2}+\nu\frac{\partial^2 u}{\partial \theta \partial x}\right)+\frac{(1-\nu)}{2}\left(\frac{\partial^2 v}{\partial x^2}+\frac{1}{R}\frac{\partial^2 u}{\partial x \partial \theta}\right)=\frac{\rho\left(1-\nu^2\right)}{E}\frac{\partial^2 v}{\partial t^2}, \tag{2.28b}$$

$$-\frac{1}{R}\left(\frac{w}{R}+\frac{1}{R}\frac{\partial v}{\partial \theta}+\nu\frac{\partial u}{\partial x}\right)+\frac{1-\nu^2}{Eh}q=\frac{\rho\left(1-\nu^2\right)}{E}\frac{\partial^2 w}{\partial t^2}, \tag{2.28c}$$

[2]Calculated using outer diameter $D=8\,\text{m}$, a wall thickness $th=0.075\,\text{m}$. Slenderness ratio is defined as $\lambda=kL/r_g$ in which k is the effective length factor, L the length of the structure and r_g the radius of gyration defined as $r_g=\sqrt{I/A}$ in which I is the area moment of inertia and A the cross-sectional area. For $k=1$, this results in a slenderness ratio $\lambda=35$ and for $k=2$, it results in $\lambda=70$.

where θ and x are the coordinates as shown in Figure 2.8a. The longitudinal, tangential and radial directions are depicted respectively u, v and w. Furthermore, h is the shell wall thickness, R is the outer radius and q is the external radial loading on the wall surface. These equations are coupled. It is important to note that here v represents a motion in another direction than in previous sections.

For the collinear impact, all motions can be assumed independent from θ ($\frac{\partial}{\partial\theta} = 0$), referred to as the axi-symmetric condition. Assuming $q = 0$, the equations of motions simplify to

$$\frac{\partial^2 u}{\partial x^2} + \frac{\nu}{R}\frac{\partial w}{\partial x} = \frac{\rho\left(1-\nu^2\right)}{E}\frac{\partial^2 u}{\partial t^2}, \tag{2.29a}$$

$$\frac{(1-\nu)}{2}\frac{\partial^2 v}{\partial x^2} = \frac{\rho\left(1-\nu^2\right)}{E}\frac{\partial^2 v}{\partial t^2}, \tag{2.29b}$$

$$-\frac{w}{R^2} - \frac{\nu}{R}\frac{\partial u}{\partial x} = \frac{\rho\left(1-\nu^2\right)}{E}\frac{\partial^2 w}{\partial t^2}, \tag{2.29c}$$

from which it can be clearly observed that the motion in tangential direction v, is now uncoupled from the others. For these equations, Graff (1975) proposes solutions in the form

$$u = Ae^{i(\gamma x - \omega t)}, \qquad w = Be^{i(\gamma x - \omega t)}, \tag{2.30}$$

where A and B are unknown constants, γ is the wavenumber and ω is the wave-frequency. A practical example of a cylindrical shell impacting a fixed wall is discussed in Graff (1975), based on the work of Berkowitz (1963). Figure 2.9 shows the shell impacting the wall with initial velocity V_0.

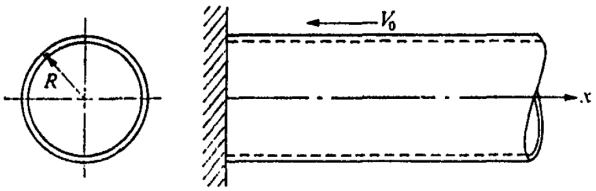

Figure 2.9: Longitudinal impact of a cylindrical shell against a rigid wall (Graff, 1975).

The example assumes the axi-symmetric condition, so that the tangential motion is decoupled from the other two. After defining the four initial conditions, two boundary conditions, and taking the Laplace transform of Equation 2.29a and Equation 2.29c, a solution for the axial shell stress, $N_x\left(x,t\right)$, is found to be

$$N_x\left(x,t\right) = \frac{-EhV_0}{\left(1-\nu^2\right)c_p^2}\frac{1}{2\pi i}\int_{c-i\infty}^{c+i\infty}\frac{e^{s(t-\zeta x)}}{s\zeta}ds, \tag{2.31}$$

in which s is the complex frequency, c_p the thin-plate wave speed

$$c_p = \sqrt{\frac{E}{\left(1-\nu^2\right)\rho}}, \tag{2.32}$$

and

$$\zeta^2 = \frac{s^2 + \frac{c_p^2}{R^2}}{c_p^2\left(s^2 + \frac{c_0^2}{R^2}\right)}. \tag{2.33}$$

The difficulty in this solution is the evaluation of the integral. Berkowitz (1963) provides an approximate solution for the axial stress. These approximations, however, are only accurate under certain rigorous conditions, and are inconvenient to reproduce due to their complexity. Figure 2.10 presents the stress

as solution to the rod impacting the rigid wall. The stress as presented is normalized by dividing by DV, in which

$$D = \frac{E}{1-\nu^2}, \qquad V = \frac{V_0}{c_p}. \tag{2.34}$$

Additionally, the normalized variables T and Y are introduced as

$$Y = \frac{x}{R}, \qquad T = \frac{c_p t}{R}. \tag{2.35}$$

This Y/T ratio, as depicted on the x-axis in Figure 2.10, represents the ratio of distance from the wave front at $x = c_p t$. It can be observed that the stress expression DV is the same as the induced stress for a rigid body impact (Equation 2.2 divided by A) except that now the thin-plate wave speed c_p is used, resulting in a slightly higher stress. Another important observation is that the stress peaks at higher values, resulting in an underestimation of the maximum stress when DV is taken. Based on Figure 2.10, the maximum stress would be approximately 20 % higher than DV. Unfortunately, the solutions presented are for the case of an elastic shell impacting an rigid wall. However, based on the findings in subsection 2.1.2, it is estimated that for two elastic shells with equal impedance impacting each other, the stress would be roughly half that of one elastic shell impacting a rigid wall.

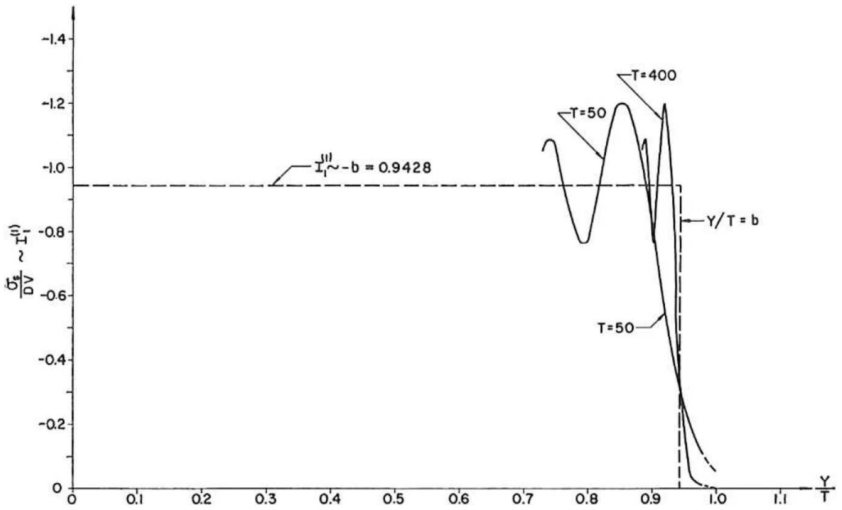

Figure 2.10: Normalized stress as function of distance from the wave front (Berkowitz, 1963).

A phenomenon that occurs in a shell, is breathing resonance close to the ring frequency (Meijers et al., 2018). The expression for the ring frequency reads

$$\omega_r = \frac{c_p}{R}, \tag{2.36}$$

in which R is the outer radius of the shell. Assuming an outer radius R of around 4 m for the WTG tower and substructure near the interface, this results in $\omega_r \approx 1360$ rad/s (216 Hz).

Compared to the rod theory, shell theory is substantially more complicated. The solution just presented assumes the axi-symmetric conditions. When one wants to include bending effects on the deformations, and bending moments and shear force in the equations of motion, this will result in considerably more complicated equations according to Graff (1975). Another point of attention is that, according to (Kolsky, 1964), a shell will behave like a rod for very long wave lengths (longitudinal waves) compared to the cylinder's diameter. As the wavelength induced by the WTG impact will be in the order of 200 m, it qualifies for aforementioned statement. Elaborating on this, shell theory would not lead to significantly different axial stresses compared to rod theory for the collinear impact.

2.1.8. Stress wave propagation in structures

Due to the impact being located at the interface, the impact-induced motions will be initiated at this location. These motions will propagate through the structure as a wave. This wave propagation is of main importance because a superposition of stress waves could potentially result in higher stresses than the induced stress. At a fixed end of a rod, a compressive incident wave will reflect as compressive wave, thus imposing a superposition of two compressive waves, resulting in a wave magnitude twice as high as the incident wave. A free end will reflect the compressive wave as tensile wave. Consequently, the superposition will result in a wave magnitude of zero. By defining the boundary- and interface conditions properly, the stress wave propagation is inherently accounted for in the rod, beam and coupled theories as discussed before. The speed of sound of a certain material defines the speed of the wave propagation.

The substructure is, to some extend, fixed at the bottom in the soil. However, it is not completely fixed due to soil stiffness and damping. In addition, the soil conditions are hard to predict exactly. Therefore, it is difficult, if not impossible, to accurately predict what the exact boundary condition at the bottom is. Another difficulty of predicting the boundary condition is that the variable cross-section geometry of the substructure itself causes reflections. Also, there will be some fixation at the mud-line, where the soil starts to surround the substructure. This surrounding soil will provide some damping and stiffness as well.

Some of the effects as discussed for the substructure are applicable to the WTG. The tower of the WTG will, due to its conical geometry, cause reflections. The RNA at the top of the tower will act as an inertia, and just above the interface, the lower lifting tool is attached by which the weight of the WTG is lifted.

Put together, several reflections will take place at several distances from the interface and at different instances of time. Many of the effects remain uncertain due to, for example, the uncertain nature of soil conditions. To be able to qualitatively discuss these uncertainties, the effects of these conditions will be studied by tweaking values. For example, the effect of soil stiffness can be discussed by comparing results for different values of the stiffness.

2.2. Contact mechanics

As the impact between WTG and substructure is located at the interface, this problem can locally be considered as a contact mechanics problem, especially for the oblique impact model. In the case of oblique impact, the contact area will vary significantly during the impact, whereas the contact area for the collinear impact remains constant. Within the field of contact mechanics, the most commonly practised theory is known as Hertzian contact (Barber, 2018). A lot of research has been executed using the Hertzian contact theory for specific cases, such as a sphere impacting a flat surface or another sphere. The search for the application of Hertzian contact on similar geometrical structures as considered in this thesis has not been successful. Therefore, a contact model will be constructed in subsection 5.2.1, based on the theory of elasticity, geometric relations and strain approximations.

One problem that is encountered while constructing the model, is known as the singularity problem (Barber, 2018). This is one of the flaws of the theory of elasticity for continuum bodies. The singularity that will occur in this contact model, is that the contact area will increase in time, but it initially is infinitesimally small at $t = 0$. A non-zero force applied on an infinitesimally results in an infinite stress arising at the instance of impact which, although theoretically correct, is not what physically will happen. A solution to this problem is proposed in subsection 5.2.2, which entails the assumption of a non-zero initial contact area at the instance of impact.

2.3. Material behaviour during impact

In this thesis, linear-elastic material strength is assumed for the elastic regime. This linear stress-strain relation is described by the well known Hooke's law. Some effects that can cause deviation from this linear-elastic assumption are discussed. Figure 2.11 shows a typical stress-strain relationship for steel.

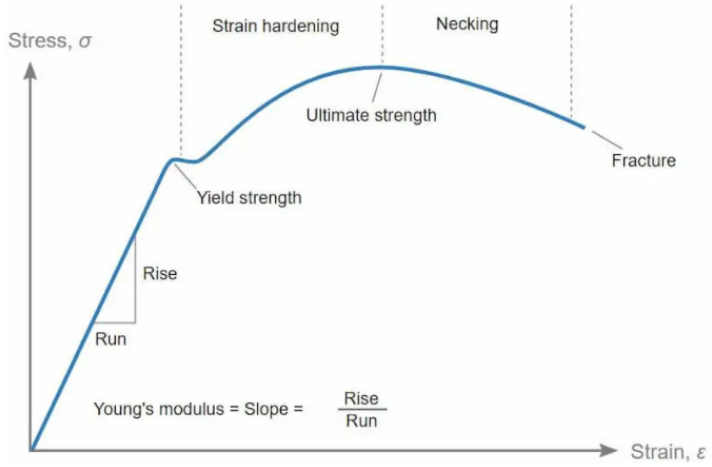

Figure 2.11: Typical stress-strain curve for steel. Figure from Wikipedia Commons Nicoguaro.

The first effect that is discussed is known as 'strain hardening'. This effect occurs in the plastic regime, and causes the material's strength to increase further up to the ultimate strength (Smith and Hashemi, 2006). Another effect that can occur in the plastic regime is known as 'strain-rate hardening'. This effect causes the material's strength to increase as a function of the strain rate at which it is deformed (Smith and Hashemi, 2006). Since both of these effects only occur in the plastic regime, they can be ignored when the stress does not exceed the yield strength of the material. In chapter 3, it will be concluded that one of the structural integrity requirements is that in principle no plasticity is allowed. Therefore, these two effects will not be investigated further in this thesis.

2.4. Stress concentrations

One of the challenges in this research is to determine where in the structure the critical stress occurs. This could be somewhere away from the interface due to reflections, or right at the contact surface, where especially the oblique impact will likely induce high peak stresses. Due to the specific geometry of the flange, this could also be, for instance, in the neck of the flange due to stress concentrations. Another location that deserves attention, is the welded connection between flange and tower or sub-structure. Figure 2.12 illustrates these locations. Some of the existing knowledge in the literature about this topic is discussed now.

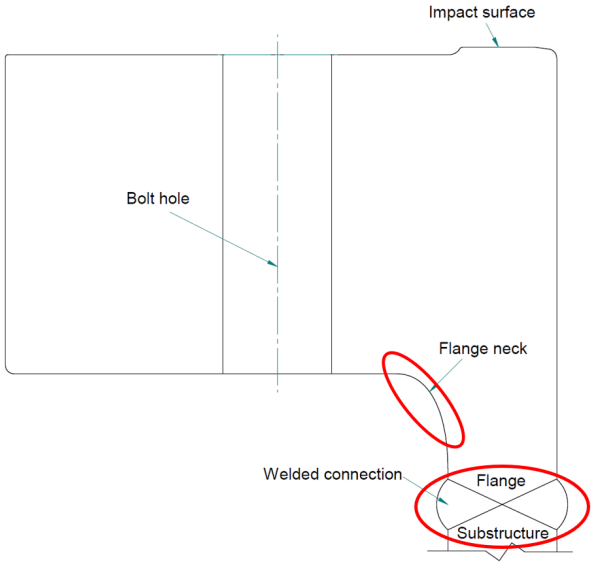

Figure 2.12: Potential flange stress concentration areas depicted in red.

Extensive research has been devoted to stress concentrations in welds. The DNV recommended practice 'Fatigue design and offshore steel structure' contains stress concentration factors (SCF's) for several weld details (DNV AS, 2019b). These SCF's are determined for fatigue damage purposes, thus applicable for dynamic loading, although based on significantly lower frequencies than an impact entails. Because the impact load under consideration in this thesis is dynamic as well, these SCF's are assumed more appropriate compared to SCF's for static loading, which are abundantly available. Considering that a lot of research has been done into this, together with the fact that applicable SCF's are presented in DNV AS (2019b), it is decided to not further investigate the weld SCF in this thesis.

For geometrical details, a lot of analytical derivations and results are presented in Pilkey (1997). A detail that gets very close to the flange neck detail is the shoulder fillet detail shown in Figure 2.13. The flange neck, however, is still slightly different, and also its applicability for dynamic loading is not mentioned. One potential significant difference between the detail presented in the figure and the flange neck under consideration is, that for the flange, the load is most likely not distributed equally in the 'thick' part (denoted with thickness H) of the detail from the figure. This makes it unlikely that the stress in the thick part of the flange, H in Figure 2.13, is distributed equally over the thickness.

Considering the limited time in which this thesis is completed, it is chosen to not focus on investigating the exact stress concentrations in the flange neck, as priority is given to modelling the impact and the contact. As will be shown in chapter 5, the peak stresses at the surface due to oblique impact will most likely be higher than stresses in the flange neck, even if a SCF of around 5 is assumed. Therefore, the stress concentration factor for the flange neck will be most important for the collinear impact model, but in an oblique impact, it will most probably not be governing.

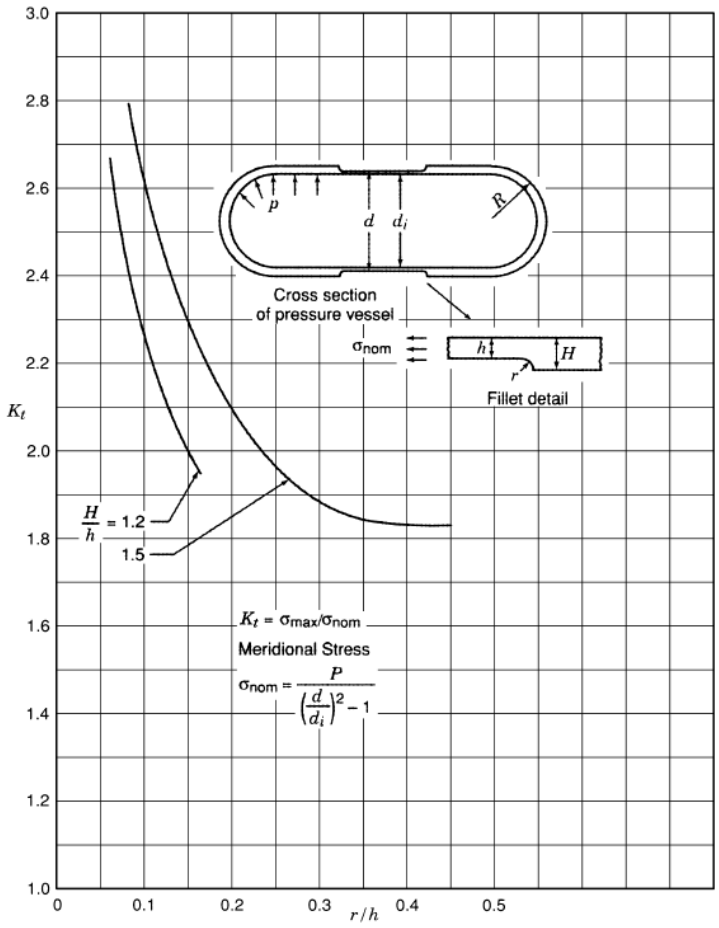

Figure 2.13: Stress concentration factor K_t for a stepped pressure vessel wall with a shoulder fillet (Pilkey, 1997).

2.5. Impact modelling conclusion

For the modelling of the impact, several theories and models are discussed. The rigid body ram impact model is relatively simple, but has the considerably downside of neglecting the continuum properties of the WTG tower, such as its elasticity. The mass-spring elements in series model offers the ability to include elastic properties of the tower, making it more suitable. The governing equation on which the model is based, is the wave equation, which is also governing in the classical rod theory, making the mass-spring elements model basically a numerical solver of an impact on a rod. Classical rod theory analytically describes the longitudinal motions in elastic rods. Due to its ability to take into account the WTG- and substructure's elastic properties, variable cross-sectional area and several boundary conditions, it is deemed very suitable to model the collinear impact case with in this thesis. Additionally, according to Kolsky (1964), rod theory pretty accurately describes longitudinal vibrations for a shell structure if the induced stress wave is relatively long. The Rayleigh-Love rod theory offers the lateral inertia effects to be included, but due to the limited frequencies it can describe, it is not necessarily closer to reality compared to the classical rod theory. Both theories will be modelled to investigate the differences. The inherent axi-symmetric condition of the collinear impact makes beam theory and shell theory unnecessary, because no bending will occur.

The oblique impact model does require the ability to describe transverse motions, in order to simulate the oblique impact by means of describing bending moments and shear forces. The simplest way to include this is by using both rod and beam theory, and couple them solely at the interface by means of interface conditions. The other way to couple longitudinal and transverse motions is by using the coupled equations of motion, but this is not preferred due to the increased complexity. Geometrically, modelling the substructure and WTG tower as shell would be most accurate. Shell theory though, will lead to a much more complicated model, while it does not necessarily result in significantly more accurate results. Considering the desire for a 'simplified' model, and the time window in which this thesis is completed, it is decided to leave shell theory out of account. For the oblique impact, the rod and beam coupled by interface conditions is chosen to construct the oblique impact model with.

Considering the local effects at the interface, a contact model will be constructed in order to approximate contact stresses at the interface induced by the oblique impact. As explained, SCF's for the weld and flange neck will not be investigated further for distinct reasons, as the focus lies on the impact modelling and contact model.

Following from the findings in this chapter and chapter 1, the impact velocity V_i and oblique impact angle α are considered the most useful and convenient-to-check kinematic variables that determine the impact load. Therefore, the allowable impact will be expressed in these variables. This answers the fourth research sub-question, which was formulated as ***"What are the best parameters in which to express the acceptance criterion, and that is convenient to determine critical ship dynamics?"***.

3

Structural integrity

The definition of structural integrity requirements for the installation of the WTG on the substructure is of fundamental importance for providing specific acceptance criteria. These requirements form the basis on which the allowable impact will be defined. The determination of these requirements will be presented in this chapter, where multiple sources are investigated. First, methods of design that are commonly practised in structural engineering are discussed in section 3.1, and a choice of preference for one method will be explained. Next, the limit states, which form an important part of the preferred design method, are discussed in section 3.2. An extensive investigation into requirements specified in codes and standards is performed and presented in section 3.3. As will be explained there, Det Norske Veritas (DNV) is commonly used within HMC and more generally in the offshore wind industry, but consideration is given to other sources as well. The codes and standards will form the basis on which the structural integrity requirements will be based, but also other potential requirements are discussed. A potential requirement which could be imposed by a client or supplier is presented in section 3.4. For example, one supplier specifies maximum accelerations for the RNA, as some equipment is sensitive for accelerations. Finally, section 3.5 presents the conclusion concerning the requirements. The specific structural integrity requirements governing in this thesis will be formulated there.

3.1. Structural design methods

Two well-known design methods that are often used in structural engineering are the working stress design method (WSD), and the load and resistance factor design method (LRFD). These methods provide guidance in the design of structures, and introduce ways to ensure sufficient safety in designs. The fundamental difference between WSD and LRFD is that the latter enables for multiple safety factors whereas WSD only allows for one (Galambos and Ravindra, 1981). Also, the LRFD method makes use of so-called 'limit states', as elaborated upon in section 3.2. According to Galambos and Ravindra (1981), the LRFD method has the potential to be more consistent. DNV has offshore standards for both the WSD and LRFD method, DNV-OS-C201 and DNV-OS-C101 respectively. From HMC's perspective, the LRFD method is more common nowadays within the wind industry, especially in Europe. Vugts (2013) also mentions that the design of offshore structures, following Eurocode or International Organisation for Standardization (ISO) codes, is almost exclusively done based on LRFD nowadays. Due to common practice and the increased level of customization, the LRFD method is preferred in this thesis. Within LRFD, it is common practice to identify what kind of 'action' is considered, and for this thesis, the impact is the action. According to NORSOK N-001, the impact during installation would be identified as 'variable action', denoted Q.

3.2. Limit states

According to DNV AS (2021), limit states are "conditions beyond which a structure or structural component will no longer satisfy the design requirements". These limit states form a structured method to identify the structural integrity requirements. The limit states and their implementation in the context of this thesis are discussed. The four limit states are the ultimate limit state (ULS), fatigue limit state (FLS), serviceability limit state (SLS) and accidental limit state (ALS). The latter will not be discussed as

it is considered not to be within the scope. This is supported by DNV AS (2017) stating that ALS does not have to be considered in the transport and installation (T&I) phase, which this thesis comprises. The FLS will be discussed shortly, in order to arrive at the conclusion that FLS is not within the scope either. ULS and SLS will be discussed in more detail.

3.2.1. FLS

The FLS corresponds to the failure of the structure due to the effect of dynamic loading. One could think of an impact as a single action contributing to the fatigue damage, but if it features only one action, it is per definition not considered for fatigue. Another effect that could have indirect influence on the fatigue life of the structure, is residual stresses caused by the impact. When the impact causes residual stresses, these will remain during service life, influencing the actual stresses in the material during dynamic loading. If some dynamic force results in a certain stress level at the location where the residual stresses are, then the actual stress in the material will be the sum of the residual and dynamic-induced stresses. This will obviously affect the actual fatigue damage, which is strongly affected by stress magnitude.

The question remains why FLS will not be considered. This is explained by the fact that residual stresses are exclusively induced when plastic strain occurs. One of the requirements resulting from this examination is that in principle no exceedance of the yield stress is allowed, at least not at locations that are critical for fatigue during the lifetime of the structure. DNV AS (2021) states that for less than 1 % plastic strain occurring in the ULS analysis, no detailed analysis of the impact on the fatigue strength is required. Hence, this requirement allows the residual stress effect on fatigue damage to be disregarded.

3.2.2. ULS

The ULS corresponds to the maximum load-carrying resistance, such as loss of structural resistance due to excessive yielding. In the context of the WTG impacting the substructure, loss of structural resistance could occur when the stress in the flange neck, or any other critical region exceeds the yield stress of the material. Exceeding the yield stress first results in plasticity only, but when the exceedance increases further, loss in strength capacity will happen. This loss in capacity could lead to failure of the structure. Besides the yield capacity, also local and global buckling are covered by ULS. This buckling failure mode, however, will not be focused on in this thesis, considering the limited time window.

3.2.3. SLS

The SLS corresponds to the state beyond which the structural system loses its serviceability from an operational point of view. For example, grating of an access platform which is heavily deflected when walked on. It does not fail, yet it can lose its serviceability by feeling dangerous for the people walking on it, as access is supposed to be, but also feel safe. A more relevant example is that of excited accelerations on certain equipment. High accelerations can damage, thereby decreasing serviceability of, this equipment, while the structural integrity does not have to be affected by it.

3.3. Codes and standards

HMC often chooses to comply with the classification society Det Norske Veritas (DNV), and is therefore considered the governing classification society in this thesis. Where possible, the structural integrity requirements comply with, but are not restricted to DNV. The relevant requirements stated by DNV are listed per code. For some aspects however, other codes provide useful requirements as well, meaning that the codes and standards requirements are not restricted to DNV prescription.

3.3.1. DNV

Assuming DNV as code compliance, the code-checking path for installation operations is as follows: ‘DNV-ST-N001 Marine operations and marine warranty’ (DNV AS, 2018) is the overarching governing code. It also provides load and material factors. It provides a material factor of γ_m 1.15 and a load factor γ_f of 1.3 applicable for ULS analyses using both LRFD and WSD methods. This code often refers to more specific codes, in this case to ‘DNV-OS-C101 Design of offshore steel structures, general LRFD method’ (DNV AS, 2019a). This code specifically describes how to apply the LRFD method on offshore steel structures. Another code it refers to, which is highly applicable for this thesis, is ‘DNV-ST-0126

Support structures for wind turbines' (DNV AS, 2021). First, this code is examined. The limit states, as defined earlier, are taken from this standard, but these definitions are DNV-broad. This standard outlines the LRFD method applied to support structure design for wind turbines. It provides the following design equations. Design load effects should be smaller than design resistance

$$S_d \leq R_d, \tag{3.1}$$

and load factors, γ_f, relate design load effects to characteristic load effects

$$S_d = \gamma_f S_k, \tag{3.2}$$

and material factors, γ_m, relate design resistance to characteristic resistance

$$R_d = \frac{R_k}{\gamma_m}. \tag{3.3}$$

Some additional, more specific, requirements are provided in 'DNV-ST-0054 Transport and installation of wind power plants' (DNV AS, 2017). It states that "limiting values for accelerations and vibrations of sub-components and other parts of the nacelle should be obtained from the component manufacturer and be considered accordingly". Also, specifically for piling, it mentions that fabrication tolerances, clearances, deflections and pile sway have to be considered. Additionally, the total pile stress (static plus dynamic) shall not exceed the pile's yield strength. For the set-down operation, "allowable maximum set-down velocity shall be determined during development phase based on impact analysis". This is basically what this thesis is all about. For the set-down, it also provides the following recommendation: "it is recommended that the set-down speed is limited to a maximum value of 0.5 m/s and impact loads to no more than 3 % of the submerged weight including added mass". This recommendation, however, will not be adopted, since this thesis will investigate more thoroughly the allowable impact.

The LRFD method is described more in-depth in the standard 'DNV-OS-C101 Design of offshore steel structures, general LRFD method' (DNV AS, 2019a). It gives the load factor γ_f as 1.0 for ALS, SLS and FLS. The material factor, γ_m, for the ULS analysis for a full penetration weld, is given as 1.25 (in DNV-ST-0126) for wind turbine applications. This is of importance when the yield capacity (ULS) of the flange weld is evaluated. The mass of the structure itself shall be considered as 'permanent load', where the expected value may be based on data of the structure. On the contrary, loads associated with installation operations can sometimes be considered 'variable functional loads' (this is not necessarily the case, as lifting operation are based on permanent loads such as self-weight), which may vary in magnitude, position and direction during the period under consideration. The characteristic value of this variable functional load is the value which produces the most unfavourable load effects. Regarding the stress in the material, it states that "Simplified assumptions regarding stress distributions may be used provided the assumptions are made in accordance with generally accepted practice" and that "individual design stress components and the von Mises equivalent design stress for plated structures shall not exceed the design resistance". Finally, it appoints that structural analysis may be carried out as linear elastic, simplified rigid-plastic or plastic-elastic. This is also stated in DNV-ST-0126.

More information about the determination of structural capacity by means of FEM analysis is provided in the recommended practice 'DNV-RP-C208 Determination of structural capacity by non-linear finite element analysis methods' (DNV AS, 2019c). Information given here is especially important when performing FEM analysis. This document gives the failure modes that are dealt with in it, such as tensile failure, buckling and accumulated plastic strain. Important statement is that "linear analysis can be used for ULS checks even for structures which behave significantly non-linear when approaching their ULS". It also mentions that an explicit solver is well suited for shorter time transients, such as in impact analysis. The von Mises yield function is considered suitable for most capacity analyses of steel structures. Additionally, it mentions that in most cases it will be safe to exclude strain rate effects. Lastly, a safety factor only need to be applied for ALS and ULS according to the practice.

3.3.2. Eurocode EN

Another set of codes that are commonly used in offshore structural engineering are the so called 'Eurocodes'. Although this series provides codes for other industries as well, the 'EN 1993' series is used for the design of steel structures, such as in the offshore industry. The fundamental code for all Eurocodes is the 'EN 1990 Basis of structural design' (British Standards Institution, 2005b). The for this

thesis relevant information from this code is that the impact should be classified as a 'transient' design situation and it states, just as DNV, that material factors used in LRFD for SLS is 1.0. It should be noted that all Eurocodes use the limit state design method with LRFD.

More specific requirements about steel structures such as the substructure and WTG is found in 'Eurocode 3 EN 1993-1-1 Design of steels structures - general rules' (British Standards Institution, 2005a). First of all, this code provides material properties for steels, such as the S355 steel that is the steel used in this thesis for the substructure and WTG tower. These properties can be found in Appendix A. The nominal value for the yield strength of S355 steel is 335 MPa for a material thickness larger than 40 mm and smaller than 80 mm. Also, the code states that nominal values, as provided in the codes, shall be adopted as the characteristic value, as part of the LRFD method. The yield strength is equal for equal steel grades, but the ultimate strength differs per fabrication method. Besides the strength, the design values of the Poisson's ratio and Young's modulus are provided. Just as DNV, it states that linear elastic analysis may always be used, whatever the stress level. A yield criterion for a critical point of a cross-section, better known as the two-dimensional Von Mises equation, is given as:

$$\left(\frac{\sigma_{x,Ed}}{f_y/\gamma_{M0}}\right)^2 + \left(\frac{\sigma_{z,Ed}}{f_y/\gamma_{M0}}\right)^2 - \left(\frac{\sigma_{x,Ed}}{f_y/\gamma_{M0}}\right)\left(\frac{\sigma_{z,Ed}}{f_y/\gamma_{M0}}\right) + 3\left(\frac{\tau_{Ed}}{f_y/\gamma_{M0}}\right)^2 \leq 1, \tag{3.4}$$

where $\sigma_{x,Ed}$ is the design value of the local longitudinal stress at the point of consideration, $\sigma_{z,Ed}$ the design value of the local transverse stress at the point of consideration and τ_{Ed} the design value of the local shear stress at the point of consideration. f_y is the characteristic yield strength and γ_{M0} is the material factor. The material factor γ_{M0} is applicable for the cross-sections relevant in this thesis. The value of γ_{M0} is given as 1.0, except for the situation of "resistance of cross-sections in tension to fracture", where it should be 1.25. Please note that both DNV and NORSOK do not allow these factors to be applied, although they do refer to the Eurocode. The reason for this being that Eurocodes are specifically applicable for onshore structures, and not deemed sufficient for offshore structures. If the assumption is made that the axial force is uniformly distributed over the cross-section, specific requirements for compressive stress in cross-sections is provided as:

$$N_{c,Rd} = \frac{Af_y}{\gamma_{M0}}, \tag{3.5}$$

in which $N_{c,Rd}$ is the design resistance of the cross-section for uniform compression, and A the cross-sectional area. This condition 'uniform compression' makes this relation exclusively relevant for the collinear impact where the stress is perfectly distributed. For bending and combined bending and axial force similar requirements are given. Requirements for buckling are also presented, but since buckling is excluded from this thesis, those will not be discussed.

A value for 'limiting of principal strain' is recommended as 5 % in 'EN 1993-1-5 Design of steel structures - general rules - plated structural elements' (British Standards Institution, 2006). Furthermore, this code reconfirms that the material strength properties should be taken as characteristic values.

The following code is about the strength and stability specifically for shell structures. 'EN 1993-1-6 Design of steel structures - strength and stability of shell structures' (British Standards Institution, 2007) states that hollow structures with a radius over thickness (r/t) ratio between 20 and 5000 are to be considered as shell structures. Both tower and substructure will have, regardless of their exact geometry, ratios within this range, justifying the consideration of them as shell structures. This code introduces the two ultimate limits states that have to be considered in shell structures, the plastic limit state (LS1) and buckling (LS3). LS1 should be deemed to be reached when the primary stress reaches the yield strength throughout the full thickness of the wall at a sufficient number of points, such that only the strain hardening reserve or change in geometry would lead to an increase in the resistance of the structure. Primary stresses should be limited to the design value of the yield strength. Interestingly, it is mentioned that shear stresses in the shell due to transverse shear forces are insignificant and thus may be neglected. Considering the yield condition, the von Mises stress may be used to determine the design stress, which means that the von Mises strength design is the design yield. This is equal to the characteristic yield divided by the material factor. Then the obvious strength requirement is that the design stress must be smaller than the design strength. Finally, elastic analysis may be used in the plastic limit state LS1.

3.3.3. NORSOK

The last classification society that will be discussed is the Norwegian NORSOK. The standard 'NORSOK N-004 Design of steel structures' (NORSOK, 2004) follows the limit state method as well, and it mentions that it provides information specifically for offshore practices compared to general building codes, possibly referring to the Eurocodes. When it comes to load and material factors, it deviates from the codes and standards discussed earlier. For the material factor for ULS, it prescribes a value of 1.15 unless stated otherwise and for welds it gives a factor of 1.3. Regarding the material yield strength, the standard instructs that it should be taken as the 'minimum guaranteed' value according to the material certificate, and otherwise the 'as built' characteristic value should be taken. For this characteristic value it refers to the Eurocode standards. On page 24 of the standard, specific requirements are presented for combined axial compression and bending for tubular members. In this condition, however, coefficients are included that are specified for jacket structures and superstructures only, making it questionable how applicable it is for a monopile. Considering pile installation, the standard states "the pile should be checked with respect to yield and buckling (ULS) in the maximum possible inclined position for a design condition of maximum relevant equipment weight (e.g. hammer weight), plus pile self-weight. Current loads and possible dynamic effects should be accounted for". The current loads will not be accounted for in this thesis, since the load effects near the interface, thus above the water line, are of main interest. For pile driving, it states that "dynamic stresses caused by pile driving are to be assessed based upon recognised criteria or by using wave equation analysis. The sum of the dynamic driving stresses and the static stresses during the driving process is required not to exceed the specified minimum yield strength". No specific material factor is mentioned for this pile driving operation, hence this is unfactored. Lastly, the standard specifies design fracture toughness on page 46.

The more general standard about the integrity of offshore structures is the 'NORSOK N-001 Integrity of offshore structures' (NORSOK, 2020). This standard states that for SLS, both material and load factor are 1.0. Also, it states that "structures designed according NORSOK shall be designed according to LRFD", strengthen the choice made to design with the LRFD method. The highest load factor given for 'variable actions' and 'permanent actions' for ULS is given as 1.3.

3.4. Supplier & client requirements

An SLS requirement that is often imposed by clients or turbine manufacturers, is a maximum acceleration on certain equipment. As this thesis aims to investigate the impact generic, such that not one single turbine manufacturer is considered, a specific maximum acceleration is not identified as a requirement. However, a certain turbine manufacturer (the name will not be made public, as this information is considered sensitive) specifies maximum accelerations for the nacelle. It must be noted that these accelerations are specified for transportation. The specified maximum vertical acceleration is given as 1.5 g, where g is the gravitational constant. Despite that no concise maximum acceleration can be formulated as requirement, it provides an order of magnitude of such acceleration. The acceleration obtained from the models will be discussed considering this order of magnitude of maximum allowable accelerations. Also the fact that this maximum acceleration can be a requirement indicates that the acceleration is considered a relevant, and potentially limiting parameter.

3.5. Requirements conclusion

Concluding, the following ULS and SLS requirements will be governing for the structural integrity of the WTG and substructure. The premise of the ULS requirement is that plastic deformation is not desired, hence it should be avoided if possible. There are, however, codes that allow for some limited plastic strain. This could provide guidance in the case that plastic strain cannot be avoided. British Standards Institution (2006) mentions a maximum of 5 % plastic strain allowed, and a maximum of 1 % plastic strain is mentioned in DNV-ST-0126.

Regarding the material and load factors, it is chosen to not consider those, as they could differ per project. Also, such factors do not influence the models, but they only influence the final results. Consequently, the yield stress of the material will be considered the maximum allowable stress in the results the model outputs, and if results for a specific project are desired, material and load factor can easily be accounted for (For instance DNV, which prescribes $\gamma_m = 1.15$ and $\gamma_f = 1.3$).

Considering the SLS requirements, there will not be a stringent requirement for a maximum acceleration, because this is a turbine manufacturer requirement which can vary. Nevertheless, the models

should be able to calculate accelerations, as they could be of importance. The maximum accelerations that will occur in the system, particularly at the nacelle, will be discussed and compared to the 1.5 g prescribed by a certain manufacturer to provide insight in whether this acceleration could potentially be limiting the allowable impact.

4

Collinear Impact Model

An important intermediate step in the progress towards a model that includes the oblique angle, is the collinear model. This model assumes the oblique angle to be zero, which simplifies the model rigorous. Although this assumption is substantial, it provides for solutions that will be accurate for the collinear impact case, which are conveniently cross-checked. Also, effects of boundaries, variable cross-sectional area and wave dispersion are investigated and discussed. For instance, the influence of the RNA mass on the stress reflections is demonstrated. This model, the equations of motion and the boundary conditions are presented in section 4.1. The method that is used to solve the equations of motion is explained and discussed in section 4.2. To provide for cross-checking the results that are obtained, a FEM analysis is performed, which is explained in section 4.3. The results of the constructed model are discussed in section 4.4, where also a case study is executed with the intention of obtaining a realistic order of magnitude for results. Next, an extensive discussion about the model, the underlying assumptions and limitations of the model is presented in section 4.5. Finally, the conclusion will be presented in section 4.6 containing a discussion about the results and the relevance of this model for the problem under consideration in this thesis.

4.1. Model

For the collinear impact, in which the oblique angle α is zero, the WTG and substructure are modelled as two rods. These rods can only move in one direction, which is the axial (or longitudinal) direction of the rod, denoted x. It is assumed that both rods are perfectly aligned, so that both center-lines coincide. Figure 4.1 displays a schematic of this model.

As explained in chapter 1, the weight of the WTG is lifted just above the interface using the lower lifting tool. How this is incorporated in the model is explained in subsection 4.1.1. The boundary conditions at the bottom of the substructure and top of the WTG are discussed in subsection 4.1.2. The impact itself is modelled by defining the initial velocity of the WTG to be V_i, and zero for the substructure. The displacement initial condition is set to zero for both structures, providing for the impact starting at $t = 0$ s. Furthermore, all parameters shown in Figure 4.1 are variables in the model, allowing for tailor-made solutions. Special consideration is given to the stress wave dispersion effects in subsection 4.1.3. Also, the cross-sectional area could be x-dependent, enabling for modelling a tapered geometry or variable wall thickness of both substructure and WTG tower. This variable area is discussed in subsection 4.1.4. In order to arrive at consistent results, a baseline impact velocity V_i is assumed to be 1 m/s, unless stated otherwise. In relation to common prac-

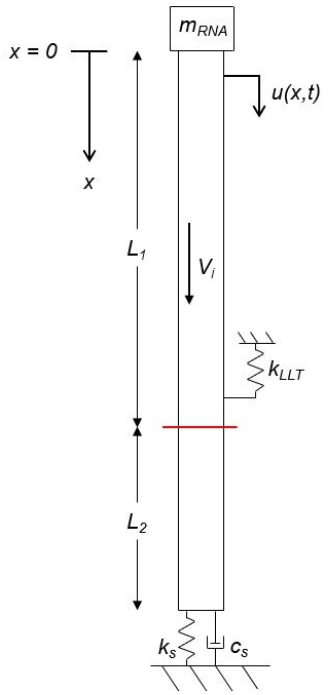

Figure 4.1: Collinear impact model schematic, red line indicates the interface.

tice of the set-down stage in an installation process, this impact velocity is considered already rather high, but as will be determined in this chapter, it allows for useful insights.

At first, let us assume no lateral inertia effects. The equation of motion for the longitudinal motions of this non-dispersive system reads

$$\rho A \frac{\partial^2 u}{\partial t^2} - \frac{\partial}{\partial x}\left(EA\frac{\partial u}{\partial x}\right) = 0. \tag{4.1}$$

Assuming constant area, this equation can be written as the well-known wave equation

$$\frac{\partial^2 u}{\partial t^2} - c_0^2 \frac{\partial^2 u}{\partial x^2} = 0. \tag{4.2}$$

Henceforth, in the interest of clarity, the derivative with respect to time, $\frac{\partial u}{\partial t}$, will be indicated with a dot ($\dot{u}$) and the derivative with respect to the spatial coordinate, $\frac{\partial u}{\partial x}$, will be denoted with accents (u'). The dimensions assumed for the model are based on the reference turbine, of which more details can be found in Appendix A. Some of the most important values of key parameters are listed in Table 4.1.

Table 4.1: Key dimensions reference WTG.

parameter	symbol	value	unit
tower length	L_1	100	m
substructure length	L_2	50	m
RNA weight	m_{RNA}	800·10^3	kg
outer diameter	D_o	8	m
wall thickness	th	0.075	m
lift cable cross-sectional area	A_{ca}	0.01	m^2
lift cable length	L_{ca}	120	m

4.1.1. Lower lifting tool

As the exact location of the LLT is variable per project, the distance of this LLT from the interface is not fixed in the model. The tension in the cable is in the order of 500 MPa, and it is assumed that the resultant stress in the cable during impact remains in tension. Obviously, in reality the tension will disappear at some instance in time, that is to say when the WTG is completely resting on the substructure. This simplification results in the ability of modelling the tensioned cable as a spring with stiffness $k_{LLT} = EA_{ca}/L_{ca}$, in which A_{ca} and L_{ca} are the cable's cross-sectional area and length respectively. In a current design of the LLT, there are four connection points at the LLT, thus four cables, all of them located such that horizontal components of forces will cancel out. This enables modelling the cables as one spring with one force, exclusively in vertical direction. The small angle approximation is assumed for the angle between cable and the WTG's centerline, so that the spring and force can be considered vertical.

Due to gravity not being accounted for in the model so far, and the tension in the cable is existent by most part because of gravity, it is decided to consider the LLT around its static force equilibrium when the full weight of the WTG hangs in the crane. This results in modelling of the cables as springs solely. This simplification leaves room for improvement in order to more accurately account for the lift- and rigging arrangement of the WTG. In reality the tension will gradually decrease as the impact lasts, but it is also dependent on the crane tip's motions and heave compensation systems.

4.1.2. Boundary conditions

At the top of the WTG, two conceivable boundary conditions are formulated. As a simplification and a condition to compare with, the top of the WTG tower could be considered as a free end of a rod. However, a more realistic condition would be to considering the RNA at the top of the tower to be a point mass. In reality this RNA is not exactly a point mass, but due to it's complex geometry and relatively high mass-concentration in comparison with the WTG tower, this approach is considered appropriate. However, since the blades have relatively low mass concentration, and their stiffness is much lower compared to that of steel, the blades' response to an impact would be much slower compared to that

of the WTG itself and the RNA. Therefore, the blades are not taken into account in the model. Also their mass is excluded from the RNA mass. These boundary conditions at $x = 0$ are, a free end and the point mass respectively:

$$u'(0,t) = 0, \tag{4.3}$$

$$EAu' - m_{RNA}\ddot{u} \mid_{0,t} = 0. \tag{4.4}$$

Likewise, for the bottom of the substructure two boundary conditions are formulated. The simplest (also most conservative regarding maximum stress) boundary condition would be a fixed end. As in reality the bottom is not completely fixed due to soil damping and stiffness, the more realistic boundary condition accounts for those. This boundary condition is represented by a so-called 'Kelvin-Voight' (KV) unit, which is a spring and dashpot combination in parallel. The spring can account for soil stiffness and the dashpot for soil damping. The damping provides for energy dissipation out of the system. Both boundary conditions at $x = L$ are, respectively for a fixed end and the KV unit:

$$u(L,t) = 0, \tag{4.5}$$

$$-EAu' - k_s u - c_s \dot{u} \mid_{L,t} = 0. \tag{4.6}$$

4.1.3. Lateral inertia

The effect of lateral inertia can be included by modifying the equation of motion. As discussed in chapter 2, lateral inertia, which is a form of dispersion, is described by the Rayleigh-Love (RL) rod theory. The Rayleigh-Love rod equation of motion, assuming no external forcing, reads:

$$\frac{\partial^2 u}{\partial t^2} - c_0^2 \frac{\partial^2 u}{\partial x^2} - \frac{\nu^2 J}{A} \frac{\partial^4 u}{\partial x^2 \partial t^2} = 0, \tag{4.7}$$

where a constant cross-sectional area is assumed. As mentioned in chapter 2, the correctness of the RL rod theory is heavily dependent on the excitation frequencies, because it has an implicit cut-off frequency limit. In the same chapter, it is also calculated that for the geometry of the WTG, the upper bound of the frequency for which the RL theory provides relatively accurate results is in the order of 540 Hz. This accuracy is based on the frequency from which the RL theory significantly diverges from exact theory. The fundamental frequency of the excitation is around 26 Hz, hence this frequency can be properly described with RL theory. It was also derived that the cut-off frequency upper bound for the RL theory is, considering the dimensions of the reference WTG, approximately 690 Hz[1]. Consequently, results from the RL theory will not contain frequencies higher than 690 Hz, and accuracy of frequencies between 540 Hz and 690 Hz will be questionable.

The classical rod theory, described by the wave equation Equation 4.2, does not yield wave dispersion. This equation has no upper bound of frequencies it can describe, but according to analysis done in subsection 2.1.4, the results start to diverge substantially from exact theory for frequencies higher than 1400 Hz.

4.1.4. Variable cross-sectional area

Until now, the cross-sectional area of the WTG tower and substructure, modelled as rods, is assumed constant, where in reality this often is not the case with monopiles and towers. At the top of the tower, the diameter is often smaller than the diameter at the interface, and also the wall thickness often varies over height. Looking at Equation 4.1, the area can also be substituted with a variable, x-dependent area, $A(x)$. In this case, the equation of motion reads

$$\frac{\partial^2 u}{\partial t^2} - c_0^2 \frac{\partial^2 u}{\partial x^2} - c_0^2 \frac{1}{A} \frac{\partial A}{\partial x} \frac{\partial u}{\partial x} = 0. \tag{4.8}$$

The effects of a variable area will be studied by comparing the results with the constant area model. It should be noted that taking into account a variable area like this still assumes uniform stress distribution over the cross-sectional area, which in reality, is not true for sharp variations in cross-sectional area.

[1] Following the procedure presented in subsection 2.1.4, with the frequency limit expression in Equation 2.20.

4.2. Solution method

The employed method of solving these equations of motion is the finite difference method (FDM). The spatial domain is discretized with resolution Δx, and finite differences are used to approximate spatial derivatives. The goal of this approximation of spatial derivatives is to transform the set of partial differential equations (PDEs) into a set of ordinary differential equations (ODEs) with respect to time, the latter being much more convenient to solve. An extensive explanation about this method and how it is applied for the specific equations of motions and interface- and boundary conditions is presented in Appendix B. One motive for using FDM is that boundary- and interface conditions can be incorporated relatively easily. Another benefit of this method is that both spatial and temporal resolution can be adjusted, in order to find a good trade-off between computing power and accuracy. Using central differences, the truncation error is in the order of $\mathcal{O}(\Delta x^2)$.

This numerical model is solved using Mathworks® MATLAB R2017a (hereafter referred to as MATLAB), and the ODE45 numerical integrator function is used to solve the differential equations. In the ODE45 solver, the second order, ordinary differential equation is written in state-space form, so that it is written as two first sets of order ordinary differential equations.

The basic value for Δx is taken as 1 m, as this turns out to describe the results well, and minimizes the computing time. It is observed that globally, various smaller values of Δx result in negligible small difference. It should be noted that for the contact model in subsection 5.2.1, this no longer is the case.

4.3. Model validation

In order to validate the models, FEM analyses are performed to compare results with. The dedicated FEM software that is utilized is Dassault Systemes® Simulia Abaqus 2021. Multiple FEM models are created, starting with an axi-symmetric rod model. The lateral inertia effects can be disregarded simply by setting the Poisson's ratio of the material, ν, to zero. Additionally, a tubular geometry is modelled, as this approximates the actual WTG and substructure geometry more accurately than a rod. This tubular consists of solids rather than shell elements. Due to the axi-symmetric nature of these models, required computing power is not inconveniently large, enabling solid elements to be used for all these models. The FEM models are explicit, dynamic models. The details about the settings, meshing, options and so on are presented in Appendix C, which also contains a mesh convergence study.

4.4. Results

The MATLAB model outputs values for $u(x,t)$ and $\dot{u}(x,t)$ for every spatially discrete node. The ODE solver itself determines the stable time increment in the solver, but it can be manually specified for what time increment the data should be written in the output. From these outputs, important parameters are calculated, such as the stress, being related to $u(x,t)$ by, for the wave equation (or classical rod) and RL rod theory respectively,

$$\sigma(x,t) = Eu'(x,t), \tag{4.9}$$

$$\sigma(x,t) = Eu'(x,t) + \frac{\rho\nu^2 J}{A}\ddot{u}'(x,t), \tag{4.10}$$

in which σ is the axial tensile stress. For convenience, all stresses obtained are factorized with -1, so that positive stresses represent compression instead of tension. For studying the effects, such as boundary condition reflections, a time-span of 0.05 s will be used. This is enough time to show all such effects. As will be shown in subsection 4.4.4, the maximum stresses will not necessarily occur within 0.05 s, hence for determining maximum occurring stresses, a longer time history needs to be considered.

4.4.1. Model comparison

For the simplest case, in which the bottom boundary condition is fixed, the top of the tower is considered a free end, and the LLT is excluded, Figure 4.2 presents the stresses at x =101 m (i.e. 1 m below the interface), resulting from the RL model, the classical rod model (wave equation) and three different

FEM models[2]. Several effects can be observed, such as the RL model not being able to described frequencies higher than the calculated 690 Hz, and its frequency amplitude decays after the initial peak due to the dispersive effects of lateral inertia. It is also observed that the frequency shown by the FEM-shell model correspond to the ring frequency of around 216 Hz as calculated in subsection 2.1.7 for the tubular structure. The frequencies shown by the classical rod are dependent on Δx [3]. Another effect that draws the attention is that the FEM-shell model shows sharp, short stress peaks just before the peak is expected. This peak is directly corrected, and shows the expected peak subsequently. Common practice in FEM learns us that this sharp peak is numerical in nature, and hence not physical.

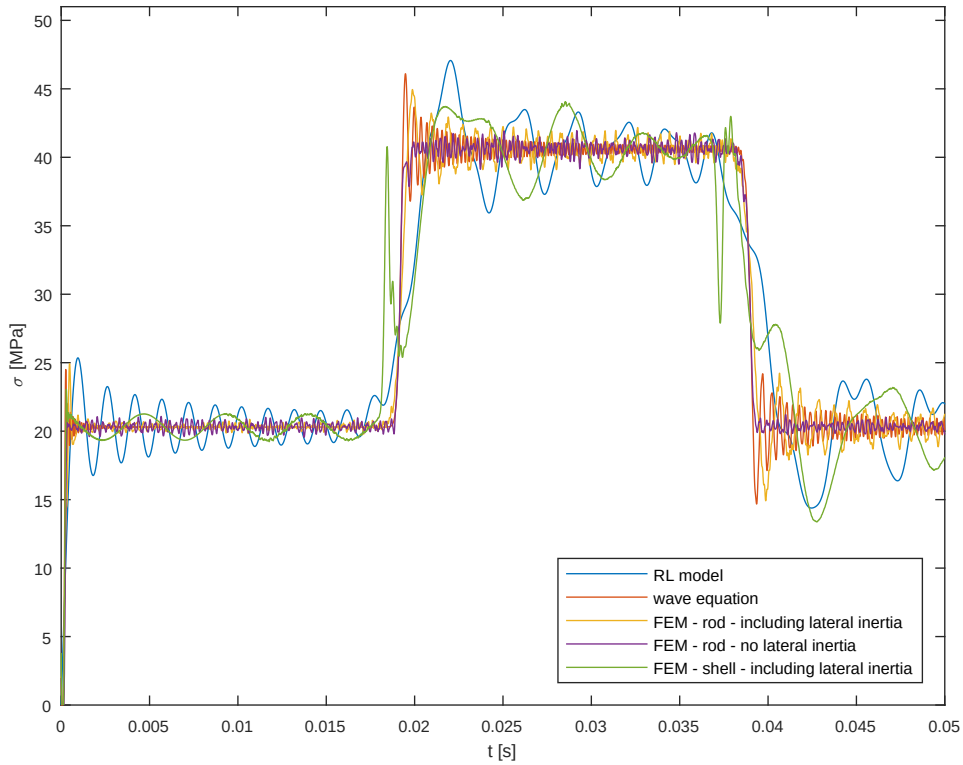

Figure 4.2: Stress Comparison of models with FEM at $x = 101$ m, one meter below the interface. Boundary conditions are fixed at the bottom and free at the top, $V_i = 1$ m/s.

Perhaps the most relevant finding is that apart from aforementioned frequency differences, all models roughly correspond. Based on these findings, together with being the most geometrically accurate, the FEM-shell model will be used to validate other effects with. These other effects will now be discussed.

4.4.2. Influence of system parameters

System parameters, such as the boundary conditions, heavily influence the occurring stress in the model. Increasing soil stiffness k_s, for instance, causes the wave reflection response to be faster, decreasing the delaying effects of the spring representing the stiffness. An infinitely stiff spring would represent a fixed end boundary condition. On the other hand, an increase of damping ratio, thus decrease of c_s, increases the dissipation of energy away from the stress wave, resulting in a lower amplitude of the reflected wave. Figure 4.3 shows these effects clearly for an arbitrary location, x =125 m located in the substructure.

[2]These models are discussed in subsection C.1.2, where the distinctions are explained. Basically there are three FEM models, one representing the actual geometry of the substructure and WTG tower the best, and the other two should comply with the analytical models the most, although in subsection C.1.2 it is explained that this does not completely hold comparing the FEM rod including lateral inertia to the Rayleigh-Love model.

[3]This relation is $\omega = 2c_0/\Delta x$ in rad/s, so that $f = c_0/\pi\Delta x$ in Hz.

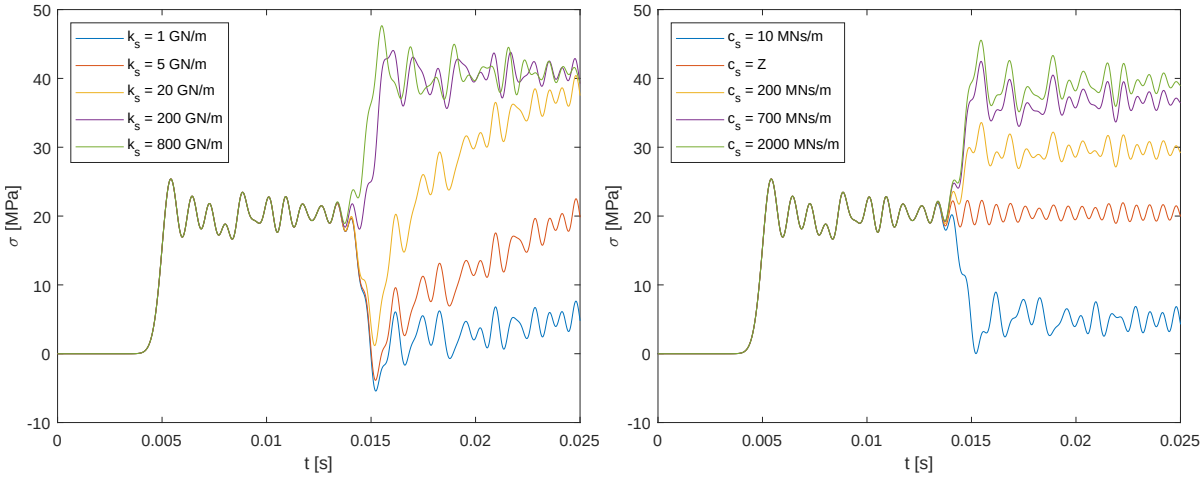

(a) No damping, different values of stiffness k_s.

(b) No stiffness, different values of damping c_s.

Figure 4.3: Soil conditions influence on stress at location $x = 125$ m in the substructure. The range of values is based on realistic values as will be derived in subsection 4.4.4.

Another influence is the mass of the RNA. A heavier mass results in more inertia at the top of the WTG, thus strengthening the inertia effect. At first, when the inertia is not accelerated yet, it causes the compressive incoming wave to reflect as compressive as well, but when it is accelerated so much that it's velocity exceeds the particle velocity at the top of the tower, it reflects compressive waves as tension waves. Increasing the RNA mass results in higher peak stresses due to superposition of incident and reflective wave. Figure 4.4 shows the effect of the RNA on the stress at $x = 25$ m in the tower.

Further, an effect that is included in the model is that of variable cross-sectional area due to a tapered geometry of monopile or WTG tower, or due to variations in wall thickness. One effect that occurs while assuming a variable cross-sectional area, is that the change in impedance and area results in stress wave reflections. At a certain discrete junction between two different structure impedance values, the incident wave will partly transmit and partly reflect. This effect is more thoroughly described in chapter 2. Assuming equal material properties and a compressive incident stress wave, a decrease in impedance results in a reflection of tension and a compressive transmitted stress wave bigger in magnitude than the incident wave[4]. This effect can also be observed in Figure 4.5, where the stress, after being initiated, slowly decreases over time. This is due to the increasing tensile stress reflections which, in superposition with the incident compressive wave, result in a lower stress. Another observation is that the stress at location $x = 25$ m increases when the decrease in impedance is bigger. Also this effect is stronger at $x = 25$ m than at $x = 75$ m. This is explained by the relations Equation 2.11 and Equation 2.12, from which is derived that for decreasing impedance, the transmitted stress wave increases in magnitude. In other words, at location $x = 25$ m, where the impedance is lower than that at $x = 75$ m, the stress magnitude is increased more than at $x = 75$ m. Both these effects can be clearly observed in the results presented in Figure 4.5.

[4] This can be readily derived from the relations presented in subsection 2.1.2, Equation 2.11 and Equation 2.12.

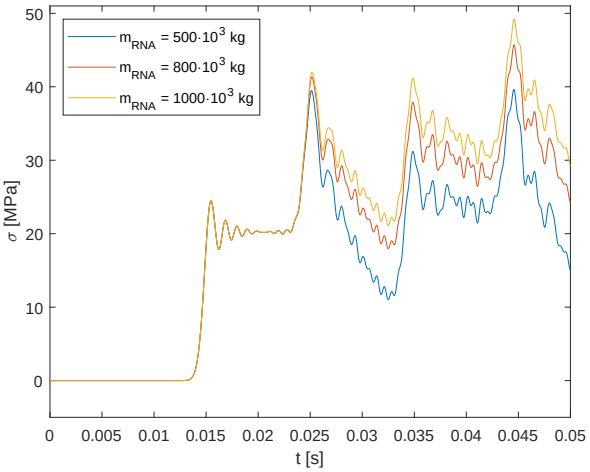

Figure 4.4: Stress at location $x = 25$ m in the tower for different values of RNA mass m_{RNA}.

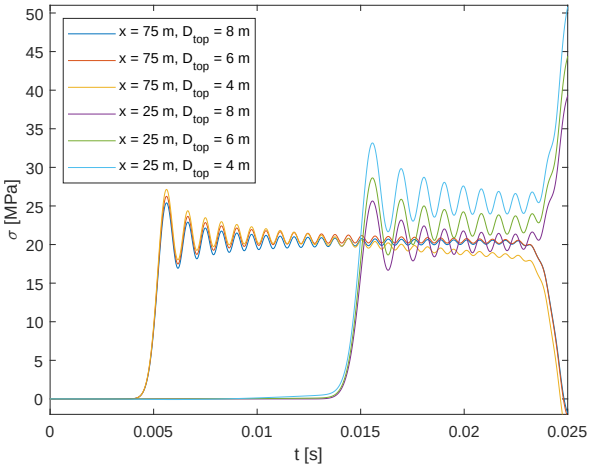

Figure 4.5: Stress at location $x = 25$ m and $x = 75$ m in the tower for different values of tower top diameter D_{top}. The diameter at the interface is in all cases $D_i = 8$ m.

Obviously, the impact speed, incorporated through the initial condition, heavily influences the results. For the induced stress in this collinear impact, the stress magnitude will increase linearly with impact speed, as can also be readily observed from Equation 2.8.

4.4.3. FEM validation

In contemplation of validating the results obtained from the models, FEM is used to compare results with. As explained in Figure 4.2, a shell tubular structure is used in FEM with a Poisson's ratio of 0.3. Figure 4.6 shows a comparison of results obtained from the FEM model, the classical rod and the Rayleigh-Love rod, at two different locations. The input parameters, such as soil stiffness, soil damping and the RNA mass are equal to those derived in the case study in subsection 4.4.4. Figure 4.6a clearly shows the effect of the RNA mass on the occurring stress 50 m above the interface in the tower. Figure 4.6b shows the influence of the boundary conditions at the bottom tip of the substructure.

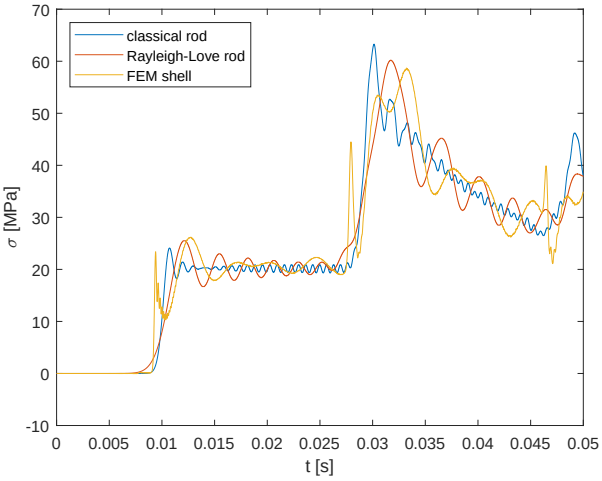

(a) Location $x = 50$ m in the tower.

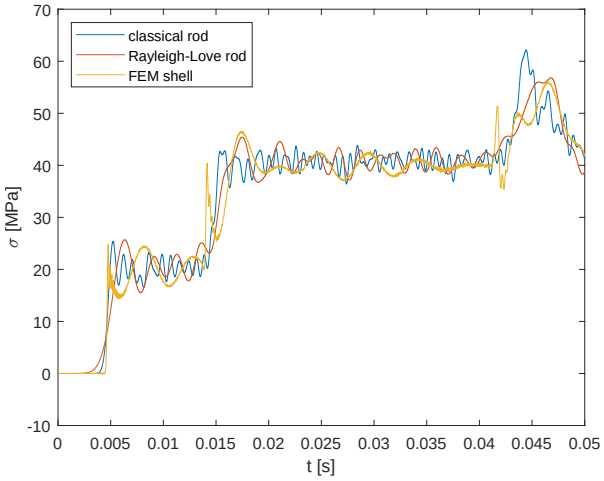

(b) Location $x = 125$ m in the substructure.

Figure 4.6: Comparison of results at arbitrary locations obtained from classical rod, Rayleigh-Love rod and FEM shell for values of m_{RNA}, k_s and c_s as assumed in the case study presented in subsection 4.4.4.

Based on these results it can be concluded that the results obtained from the FEM model correspond sufficiently well. A clear distinction between the models can be observed concerning the frequencies, as is already explained in subsection 4.4.1. The validation also shows that the effects of RNA mass, soil stiffness and soil damping are described well by all models.

4.4.4. Case study

In order to obtain a realistic order of magnitude of stresses assuming collinear impact, let us discuss the results for a case in which realistic parameter values are assumed. The Rayleigh-Love model is applied, as this includes lateral inertia effects. Values for the soil stiffness and damping at the monopile bottom tip are estimated based on the paper from Meijers et al. (2017), where data is presented based on which values for these parameters can be derived. This paper investigates drivability of large-diameter monopiles, with similar geometry as the substructure under consideration in this thesis. Shear modulus of the soil, G_s, is given as 24.25 GPa, and a Poisson's ratio of the soil, ν_s, is given as 0.48. A value of 1900 kg/m^3 is proposed for the soil density ρ_s. Based on Meijers et al. (2017), the following relations are presented:

$$k_s = \frac{4G_s R}{1-\nu_s}, \tag{4.11}$$

$$c_s = 3.4R^2 \frac{\sqrt{G_s \rho_s}}{1-\nu_s}, \tag{4.12}$$

and substituting $R = 4$ m, $G_s = 24.25$ GPa, $\nu_s = 0.48$, this results in $k_s = 746$ GN/m and $c_s = 710$ MNs/m. The geometry and mass are based on the reference turbine as presented in Appendix A. The cross-sectional area of the WTG and substructure is assumed constant, based on an outer diameter D_o of 8 m. Figure 4.7 shows the stress as function of both time and space. Figure 4.8 present the same stress, but over a much longer period of time, which illustrates that the maximum stress will not necessarily occur within the first 0.05 seconds. Nevertheless, in reality it is likely that the maximum stress does occur within the first 0.05 s, as several forms of additional damping are neglected in the model. In reality, there will always be additional sources of damping than only the soil, being for instance material damping, damping via the water, and so on. Also, from Figure 4.8 it is observed that the maximum stress has a value very close to the maximum within 0.05 s. As the exact influence of these neglected forms of damping is unknown, a longer time period than 0.05 s will be checked for results concerning maximum stresses. The baseline impact velocity of $V_i = 1$ m/s is assumed.

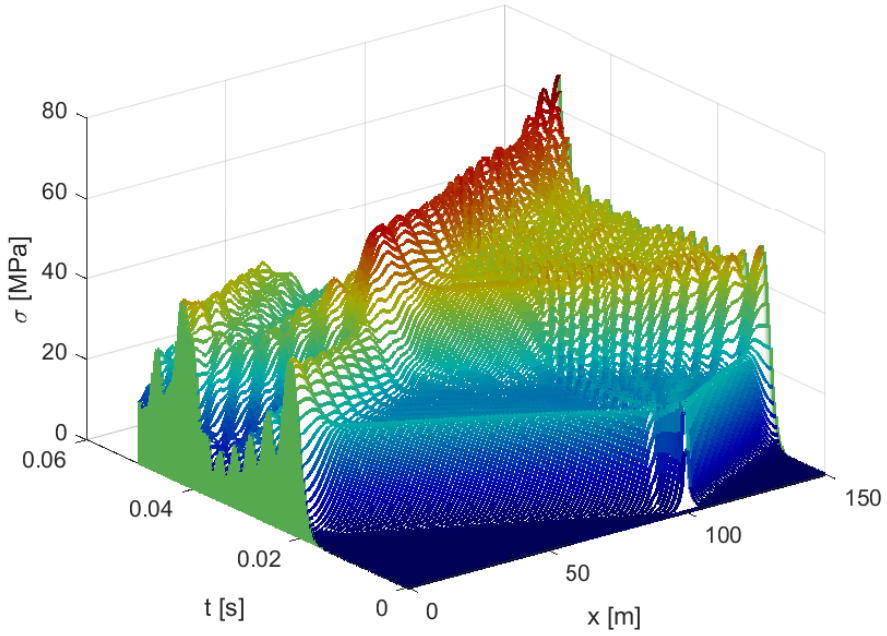

Figure 4.7: 3D plot of compressive stress σ as function of time and space, time-span of 0.05 s.

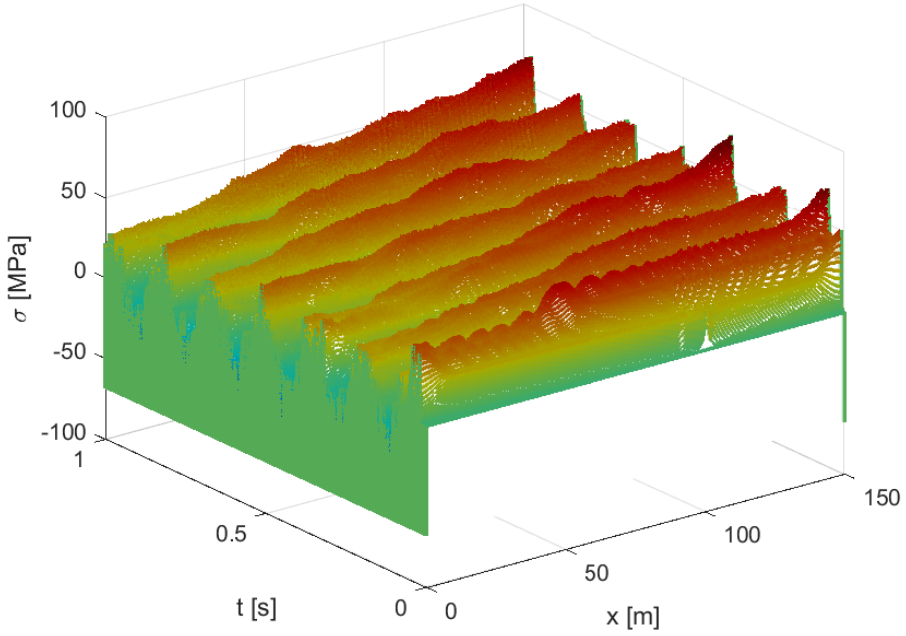

Figure 4.8: 3D plot of compressive stress σ as function of time and space, time-span of 1 s.

The maximum stress in this case study, $\sigma_{max,case}$, is found to be 78 MPa, and occurs at $t = 0.35$ s at location $x = 150$ m at the bottom of the substructure. This stress is much higher than the induced stress at the interface at the instance of impact, which is in the order of 25 MPa. This demonstrates that for the collinear impact case, boundary conditions have significant influence on the maximum stress. Consequently, these conditions may not be overlooked in determining maximum stresses for an oblique impact. Another effect, that is not mentioned yet, is that substructure and WTG tower will lose contact when the stress at the interface will become tension. In the case study, this event will take place at approximately 0.08 s. This means that results obtained after this event took place will not be accurate anymore, as the model does not account for this event. In order to obtain a more accurate estimate if and when this disconnection will take place, effects such as material damping and distributed soil damping should be taken into account, as they lower reflection effects by dissipating energy away from the vibrations. Also the gravity is not included in this model, which in reality would further decrease the chance on disconnection.

4.4.5. Axial RNA accelerations

Although the stress is of main interest for determining the structural integrity, accelerations should also be considered, as was concluded in chapter 3. Assuming the case study parameter inputs, the impact-induced accelerations occurring at the RNA are shown in Figure 4.9 both for the Rayleigh-Love and classical rod. It is also shown that the maximum acceleration seems to scale approximately linear proportional with the impact speed V_i. Comparing these accelerations to the order of magnitude of maximum allowable accelerations determined in section 3.4, it is easily concluded that the occurring accelerations are significantly higher for the impact speeds of 0.5 and 1 m/s. The order of magnitude of maximum accelerations potentially imposed by clients or manufacturers was around 1.5 g (approximately 15 m/s^2). Assuming the linear proportionality between accelerations and impact speed, a maximum impact speed V_i of 0.15 m/s can be approximated, limited by the maximum acceleration. This allowable impact speed of 0.15 m/s is, in a matter of fact, not at all an unrealistic set-down velocity value in common practice.

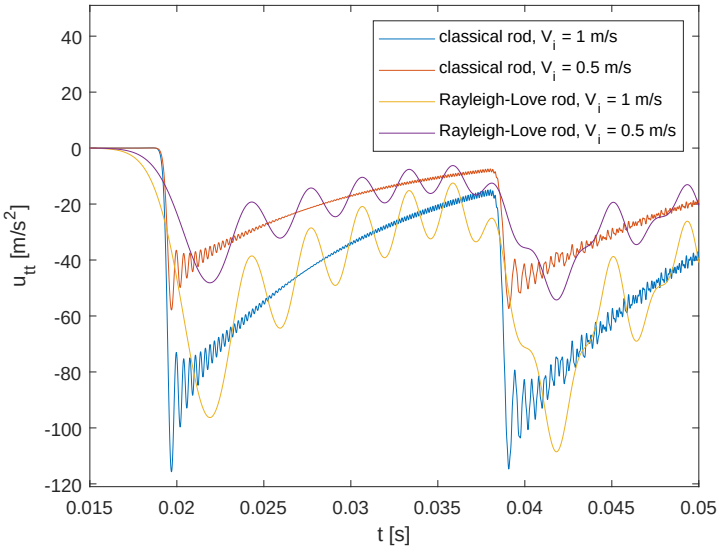

Figure 4.9: Accelerations $\ddot{u}$, depicted u_{tt}, at the RNA for a time span of 0.05 s.

4.5. Discussion

The confidence in the results obtained from the collinear impact model is rather high due to the fact that this model is relatively simple, and it corresponds the most to well-known theories such as the classical rod theory. Also, the FEM model validates the results considerably well, including effects of the boundary conditions such as RNA mass and soil conditions. In the same time, the applicability of this model is fairly low, as a zero oblique angle impact is unlikely to occur in a real WTG installation. Yet it provides clear insight in the various effects of system parameters. In this section, special consideration is given to the most important assumptions, findings, pro's and cons, and limitations of the model.

The first and foremost assumption of the collinear impact model is that the oblique impact angle α will be zero. This assumption is substantial, and limits the applicability of the results obtained. This is due to the fact that during an actual installation operation, it is near impossible that the oblique angle is precisely zero, although strictly speaking not theoretically impossible. Several effects influencing the motions of the WTG ensure it to have a non-zero oblique angle, and these are the wind, ship's motions, lift arrangement and the WTG's geometry. On the other hand, other functionalities of the collinear impact model, being the foundation for the oblique impact model and examining the influence of system parameters (RNA mass, soil conditions, and so on), are not necessarily limited by the practical impossibility of a zero oblique impact angle. The effects of the system parameters on the global response of WTG and substructure can be conveniently and accurately determined in this model. For instance, the reflection of the longitudinal stress wave by the RNA will not be fundamentally different for the oblique impact compared to the collinear impact. There will be a difference, however, because in the oblique impact also flexural waves will propagate. Also, in reality the longitudinal stress wave will also be different in shape, magnitude and distribution over the cross-sectional area, but the reflection principle will still be similar.

Assuming the collinear condition (zero oblique impact angle), describing the response of the WTG and substructure by solely describing axial vibrations is fairly accurate, as the fundamental excited wave length ($\lambda = 2L_1$) is much longer than the diameter of the hollow cylinder. For very short wave lengths, the hollow cylinder would behave more like a plate. This is substantiated in Kolsky (1964). As the fundamental excited wave length is the most important, this justifies the modelling of the hollow cylinder as a rod. Yet, shorter excited wave lengths could cause discrepancy between the modelled rod and the actual hollow cylinder, but these wave lengths then need to be much shorter than the diameter in order to do so. These waves are very short, and will both contain significantly less energy than the longer waves and will damp out faster, due to the proportionality between material damping and frequency (Nashif et al., 1985). Another difference between rod and hollow cylinder that draws the attention in the results, is that the so called ring frequency ($\omega_r = c_p/R$) of the hollow cylinder will be excited, which

is not the case for the rod. In literature, this effect is also referred to as 'breathing resonance', which occurs due to excited frequencies close to the ring frequency. Although this ring frequency is easily observed in the results, it does not significantly affect the stress magnitude.

The effects of lateral inertia are examined by comparing results obtained from the classical rod and Rayleigh-Love rod, of which the latter includes lateral inertia. On the one hand, including lateral inertia would be more accurate, as lateral inertia does occur in reality due to the non-zero Poisson's ratio of steel. On the other hand, the RL rod theory inherently imposes a frequency upper bound on the results. This frequency cap is not physical, as is explained in subsection 2.1.4. As the exact excitation frequencies are unknown, and could also contain higher frequencies than this cap, it limits the confidence in the results obtained from the RL rod. From Figure 4.6 and Figure 4.2 it is concluded that the results obtained from the classical rod and RL rod are rather similar, and result in similar maximum stress predictions. For this reason, it was decided to proceed with the classical rod for the oblique impact model, as it is simpler to model with.

Considering the FEM cross-check, it was initially expected that the RL rod should comply the most with the FEM rod including lateral inertia. Figure 4.2 shows, however, that the RL rod shows results most similar to those obtained from the FEM shell model. This is explained by the fact that the FEM rod model assumes a significantly smaller diameter, as it is required to have an equal cross-sectional area as the circular hollow section. This smaller diameter implicitly results in a different rotational moment of inertia J, and thus results in different lateral inertia effects as those described by the RL rod model. In fact, the RL rod does assume the actual rotational moment of inertia, which corresponds to the FEM shell model. This explains the fact that the RL rod and FEM shell model seem to comply the most, as they include the actual rotational moment of inertia. In general, the performed cross-check shows similar results obtained from all models. This increases confidence in the results obtained from the constructed models.

The fact that the positioning tolerance, as explained in chapter 1, is neglected, is likely to underestimate the calculated maximum stress at the interface. At the instance of impact (assuming a non-zero positioning tolerance), the contact area will be smaller than the cross-sectional area. Yet, the material at the interface that does not make contact will, due to stiffness, also be accelerated / decelerated and thus gain a relative particle velocity. Therefore, the impact force ($F = ZV_i$) will be similar to that assuming no positioning tolerance (not necessarily equal, due to the non-zero time required to mobilize the material that does not make contact), but it is distributed over a smaller contact area, resulting in higher stresses at the interface. For this reason, neglecting the positioning tolerance underestimated the stresses at the interface due to the collinear impact. Some distance away from the interface, the stress is expected to be distributed over the cross-sectional area. As a consequence, it is expected that this underestimation solely holds for stresses close to the interface. The underestimation limits the accuracy of the model in approximating stresses at the interface, and therefore inclusion of the positioning tolerance could be an improvement of the model. On the other hand, the applicability of the collinear impact model in determining accurate stress was already limited due to the unlikeliness of a zero oblique angle, while it does not limit the other functionalities of the model (such as determining impact force and investigating system parameter influence).

In the current model, the total rigging arrangement is modelled by the LLT solely as a stiffness. In reality, this system is much more complicated, as it contains also a passive heave compensation system and several hoist wires, tuggers and an upper stabilising frame (USF). In order to more accurately include these component, gravity should also be included, as it is the main cause of the initial (before impact, but when the WTG is already lifted in the crane) forces in the rigging. For instance, initially there will be compressive stresses in the WTG above the LLT, and tension stresses below the LLT. Predicting the influence of a more accurate rigging arrangement during impact is not straight forward, resulting in uncertainty about whether the inclusion of a more accurate rigging arrangement would result in more severe or more favourable stresses and accelerations in the system. This is a limitation of the current simplified modelling of the rigging arrangement, and could therefore be improved.

One of the boundary conditions is the point mass representing the RNA at the top of the WTG tower. In reality the RNA is not a point mass, but a body containing distributed mass and stiffness. Due to

several heavy components in the RNA, such as the generator, the concentration of mass of the RNA is significantly higher than that of the tower and especially the blades. Also representing the RNA mass as a point mass is conservative, as is explained in subsection 4.1.2. The point mass representation of the RNA, being both conservative and fairly accurate, makes for a justified and solid boundary condition. The boundary conditions at the bottom of the substructure currently consist of a linear spring and dashpot in parallel. These represent the soil damping and stiffness in longitudinal direction. The accuracy of the soil conditions could be increased by considering non-linear stiffness and damping, and distributed soil conditions alongside the substructure shaft under the mudline. Neglecting those forms of stiffness and damping currently results in conservatism, as more damping would dissipate more energy away from the system, hence decreasing reflections. Additionally, there are other sources of damping that are not considered currently. These are damping due to the water and material damping due to internal material affects, such as viscosity. Incorporating these forms of damping would result in more accuracy, and potentially causes lower maximum stresses and accelerations occurring in the system, allowing higher impact velocities.

The inclusion of these additional damping sources also potentially influences another phenomenon that occurs according to the model. At a certain moment (in the case study this is around 0.08 seconds after impact) disconnection will take place between WTG tower and substructure. Significantly more damping in the system could prevent this phenomenon from occurring. In practice, disconnection is highly unfavourable, as is leads to unpredictable situations. Confidently predicting whether disconnection will indeed occur requires these forms of damping to be considered.

The ability of the model to incorporate a variable cross-sectional area, representing a variable wall thickness or tapered geometry, is valuable. In the first place because monopiles (substructure) and wind turbine towers often do indeed have a tapered geometry and variable wall thickness. Furthermore, the influence of a variable cross-sectional area can significantly increase maximum occurring stress, thus decreasing allowable impact speeds. This is concluded based on the results and explanation presented in subsection 4.4.2 and Figure 4.5. These results only emphasize the importance of including a variable area in the case it is present.

4.6. Conclusion

The constructed collinear impact model is able to describe the impact-induced stress wave propagation throughout the system, consisting of the substructure and WTG. Several effects, such as the influence of the RNA mass, soil damping and stiffness, and a variable cross-sectional area, are included, observed in the results and discussed qualitatively. The cross-check between FEM and the results obtained from the model correspond well, increasing confidence in the model. A case-study has been performed in order to arrive at results that could be considered realistic, assuming the impact to be collinear.

The most significant limitation of this model is that it assumes a collinear impact, in which the oblique impact angle is zero, while in reality, the WTG will almost certainly impact the substructure with a non-zero oblique angle. The oblique impact causes effects, such as bending and increasing contact area, that may not be neglected. Another limitation is that the model does not account for potential loss of contact between substructure and WTG tower in the event of resultant tension at the interface. This limitation, however, is not significant, as the real maximum stress is likely to occur before this event. Although the disconnection phenomenon does not limit the capabilities of this model to predict maximum occurring compressive stresses, disconnection would be problematic operationally. Effects that are not included in the model, such as gravity, distributed soil damping and material damping, would all decrease chances of disconnection actually happening.

Nonetheless, this collinear impact model proves valuable as it can conveniently describe the influence of system variables, such as the RNA mass, variable cross-sectional area and soil conditions. An increase in RNA mass, for instance, results in a higher reflection, hence a higher maximum stress. These effects, although not necessarily quantitatively equal, will hold for the oblique impact as well. Additionally, the results obtained in the case study indicate the relevance of the boundaries, as well as provide a good understanding of stress wave propagation and an order of magnitude for stresses in the system. For example, the occurring maximum stress in the system can be more than three times

higher than the impact-induced stress wave magnitude at the interface due to superposition of incident and reflective stress waves. This only indicates that, indeed, boundary conditions shall not be overlooked. At last, the collinear impact model serves as a confident base from which the oblique impact model can be extended. Considering the in section 4.5 discussed assumptions, it is concluded that the collinear impact model yields conservative stress approximations, but the negligence of the exact flange geometry and non-zero positioning tolerance do not yield conservatism.

5

Oblique Impact Model

As the collinear impact model's applicability is considerably limited, as it can only describe the improbable occasion of a collinear impact, a more sophisticated model is required to analyse the impact effects of a WTG set-down on the substructure. An oblique impact is expected to influence both the global response of the system as well as the local impact-induced effects at the contact area. Globally, an oblique impact imposes a moment, and to a lesser extent shear force, at the interface due to eccentricity of the impact contact force. Locally, the oblique impact results in non-homogeneous indentation of both bodies due the impact. The contact area will initially be very small but will increase rapidly as the force grows and the indentation progresses. A model that can exclusively describe longitudinal motions does not suffice anymore when these effects need to be incorporated. Consequently, an oblique impact model is made to describe the global response of the system by coupling rod theory with beam theory to include the ability to describe transverse motions. In this way, bending moments and shear force can be included. For the local effects near the interface, a contact model is made to approximate the peak stresses at the interface due to the indentation. These models are presented in section 5.2. The method used to solve the governing equation is explained in section 5.3, followed by the validation of both the contact model and the global oblique impact model in section 5.4. The results of the model together with the validation results are presented, analysed and discussed in section 5.5, from which a conclusion is drawn in section 5.7. In the conclusion, also the limitations and relevance of the results are discussed. An extensive discussion is presented in section 5.6 about the limitations, findings and underlying assumptions. Before heading on to the model, let us first discuss some expectations of the oblique impact compared to the collinear impact in section 5.1.

5.1. Expectations

Especially for the local effects near the interface, it is expected that the oblique impact is significantly different compared to the collinear impact. In a collinear impact, the contact area will be equal to the total cross-sectional area of the structures at the interface directly upon impact, and remain constant afterwards. For the oblique impact, the contact area will be extremely small upon impact, but will increase rapidly due to elastic, and potentially plastic deformations. Given that the contact area will be very small at the beginning of the impact, it is expected that contact peak stresses will be much higher than the stresses following from the collinear impact.

Likewise, the global response is expected to be quite different. This is due to the fact that the oblique impact causes the contact force to act with some eccentricity from the neutral axis of the tubular WTG and substructure. This imposes a moment and shear force at the interface, resulting in transverse vibrations of both structures. Especially the moment (as the shear force is expected to be relatively small) will potentially influence the total stresses in the components as bending stresses add up to the axial stress.

Another expected difference is the maximum occurring acceleration due to the impact. As in the collinear impact the contact area is directly maximum, it is expected that accelerations resulting from such impact are high compared to a situation in which the contact area increases over time. This is due to the fact that in the case of a bigger contact area, there is more material that resists the impacting

structure, so that it is decelerated faster, ergo higher maximum absolute acceleration. Due to the collinear force input assumption, this can unfortunately not be examined using the current model.

Lastly, plasticity is more likely to occur, also for smaller impact speeds. Due to the contact area being small initially, local plasticity could easily occur for the same impact speed at which the collinear impact induced stresses do not even approach the yield stress. Overall, it is expected that the oblique impact will cause significantly higher stresses than the collinear impact, resulting it to be the limiting case.

5.2. Model

The oblique model needs to incorporate the effects caused by the oblique impact. One important effect is that an oblique impact causes a bending moment, and also a small shear force, to be introduced at the interface. In order to account for this, the rod model, as explained in chapter 4, is combined with a beam model. The beam model assumes the same geometry as the rod model, and boundary conditions will be formulated following the same logic as for the rod model. The input for the beam model is the introduced moment and shear force at the interface on both WTG and substructure. The most significant assumption in this approach will be that the force at the interface will be obtained from the rod model, and this force determines, together with the eccentricity the moment and shear force introduced. This results in a one-way coupling between the rod and beam models, as the force from the rod model determines the moment and shear force imposed at the interface. For the sake of simplicity, the classical rod theory (wave equation) is employed for the global model, instead of the Rayleigh-Love theory. Assuming constant cross-sectional area, the governing equations of motion describing the longitudinal (rod) and transverse (beam) vibrations in this coupled model are, respectively,

$$\frac{\partial^2 u}{\partial x^2} - \frac{1}{c_0^2}\frac{\partial^2 u}{\partial t^2} = 0, \tag{5.1}$$

$$\frac{\partial^4 v}{\partial x^4} + \frac{1}{a^2}\frac{\partial^2 v}{\partial t^2} = 0, \qquad a^2 = \frac{EI}{\rho A}. \tag{5.2}$$

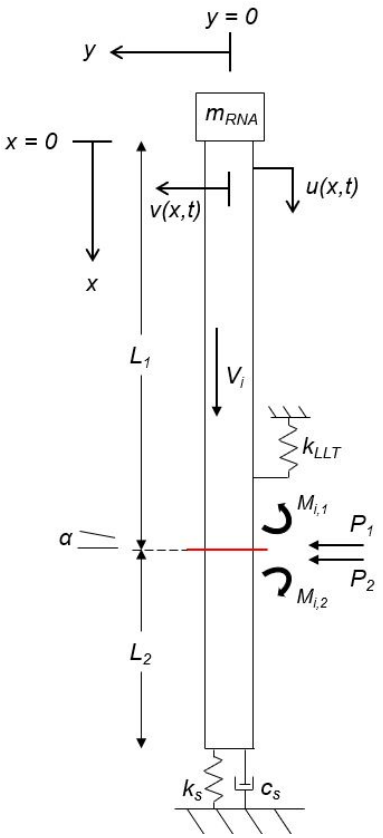

Figure 5.1: Oblique impact model schematic, red line indicates the interface.

Two effects of the oblique impact are distinguished, one being the global response of the components (WTG and substructure) to the moment and shear introduced at the interface, and the other being the local effects, being the contact stresses and indentation at the interface. These two are not completely independent, as the eccentricity of the location on which the force acts will be determined in the contact model. The local effects will be covered in this contact model, which will be a sub-model within the oblique impact model, where the latter also includes the global response. A schematic of the global model is shown in Figure 5.1. Considering the time window in which this thesis had to be completed, the implementation of a variable cross-sectional area is left out. However, this could be implemented in similar regard as explained in the collinear impact model in chapter 4. The soil conditions as determined in the collinear impact case study, subsection 4.4.4, are adopted.

5.2.1. Contact model

As just discussed, the contact model should be able to describe contact indentation stress and eccentricity of the contact force. In order to develop such model, assumptions have to be made. The first assumption, which is fundamental for this approach, is that the contact force is obtained from the collinear impact force at the interface. In other words, the force is considered an input in this contact model. A more comprehensive explanation of which force input exactly is presumed can be found in

subsection 5.2.3, as it turned out not to be as straightforward as one initially might suppose. The reason being that the maximum indentation stress following from the contact model is not only dependent on the force magnitude, but also on how fast this force develops after the instance of impact, and this is quite substantially influenced by the value chosen for the numerical parameter Δx in the MATLAB model. A problem that occurs in this model, commonly present in contact problems, is that a singularity arises at the instance of impact, at the location where first contact will be made (Barber, 2018). This problem will be more thoroughly explained, and a solution will be proposed in subsection 5.2.2.

Another assumption, which will be explained more thoroughly while deriving Equation 5.10, is that of vertical indentation. In addition, solely vertical strains are assumed. Also the effect of slip is not considered. Less fundamental assumptions, such as that of a thin-walled cylinder for determining the contact area, will be explained where applied. Figure 5.2 shows a schematic of the indentation model and important parameters, which will be utilized.

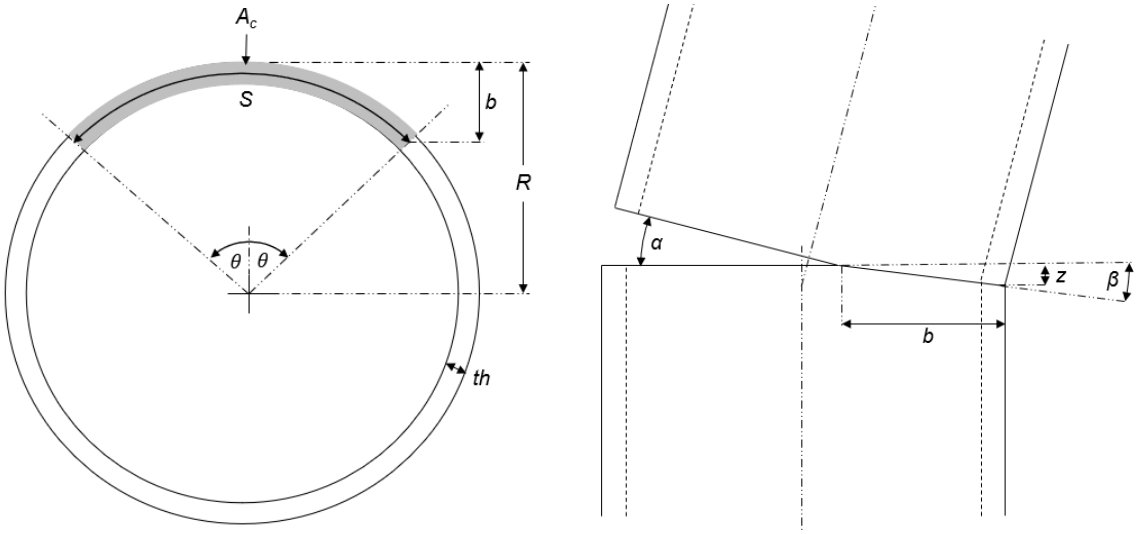

(a) Top view.

(b) Side view.

Figure 5.2: Oblique impact contact area and indentation relation.

Let us now derive the relation between force and indentation z. Assuming linear elastic material properties, the force can be written as

$$F = A_c E \bar{\varepsilon}, \tag{5.3}$$

in which $\bar{\varepsilon}$ is the average vertical strain over the contact area A_c. Let us first define the geometric relations which are required in order to write the force exclusively as function of z. The parameters are depicted in Figure 5.2, in which S is the arc length of a circle, th the wall thickness and β the indentation angle, which is, assuming that both WTG and substructure deform similarly, equal to half the oblique impact angle α,

$$\beta = \frac{1}{2}\alpha, \tag{5.4}$$

$$b = \frac{z}{\tan(\beta)}, \tag{5.5}$$

$$\theta = \arccos\left(1 - \frac{b}{R - \frac{1}{2}th}\right), \tag{5.6}$$

$$S = 2\theta\left(R - \frac{1}{2}th\right), \tag{5.7}$$

$$\bar{z} = \frac{1}{A_c} \int_0^z A_c dz, \tag{5.8}$$

in which $\bar{z}$ is the average indentation. Figure 5.3 depicts the maximum and average indentation, respectively z and $\bar{z}$.

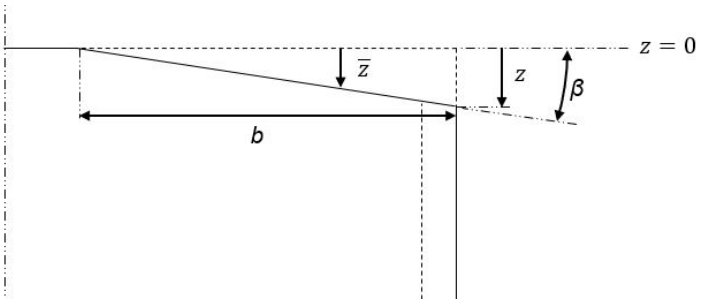

Figure 5.3: Indentation relation.

The area of contact is approximated by assuming a thin-walled cylinder, so that

$$A_c = S \cdot th. \tag{5.9}$$

Given that the geometric relation between the contact area and indentation is established, let us continue deriving an expression for the average strain resulting from the impact-induced deformation. The first assumption that is made is that the deformation, thus strain, will develop only vertically. This inherently assumes that strains will be defined by vertical deformations exclusively, and stiffness resisting the deformations is contributed only by material below the location of deformation. Considering these assumptions, an approximation of the average vertical strain can be derived. In this one-dimensional, linear elastic model, vertical strain in positive $x-$direction is per definition $\varepsilon = \frac{\partial u}{\partial x}$. Discrete, this can be approximated per time-step with $\varepsilon = \frac{\Delta u}{\Delta x}$. As linear material properties are assumed, the average strain is related to the average displacement by $\bar{\varepsilon} = \frac{\Delta \bar{u}}{\Delta x}$, where the average displacement $\Delta \bar{u}$ can be substituted with the average indentation $\bar{z}$. The distance within which the material at an instance t already 'notices' the stress, Δx can be approximated as $c_0 t$. After all, this is the distance the induced stress wave has travelled at instance t. A somewhat similar derivation is performed in Graff (1975) where the relation between particle velocity $\dot{u}$, and wave speed c_0 is to be found proportional to the relation between Young's modulus E and stress σ. This relation can also readily be derived from Equation 2.8. The derived approximations enables for finding an expression for the average strain to be

$$\bar{\varepsilon} = \frac{\bar{z}}{c_0 t}. \tag{5.10}$$

It should be noted however, that this expression only holds for a limited amount of time, until reflections arrive. This relation is extensively discussed in subsection 5.6.1. Also, this relation, in which the wave speed is taken as one constant, does not hold for the Rayleigh-Love theory, in which different frequencies propagate with different wave speeds. In subsection 5.2.3 it will be reasoned and concluded that the force input signal for this contact model will be taken from the classical rod, rendering the latter limitation irrelevant. In order to examine the discrepancy of this approximation (Equation 5.10) compared to the actual definition of strain, being $\varepsilon = \partial u / \partial x$, both expressions are compared. Figure 5.4 shows the stresses at the interface for the collinear impact assuming $V_i = 1$ m/s.

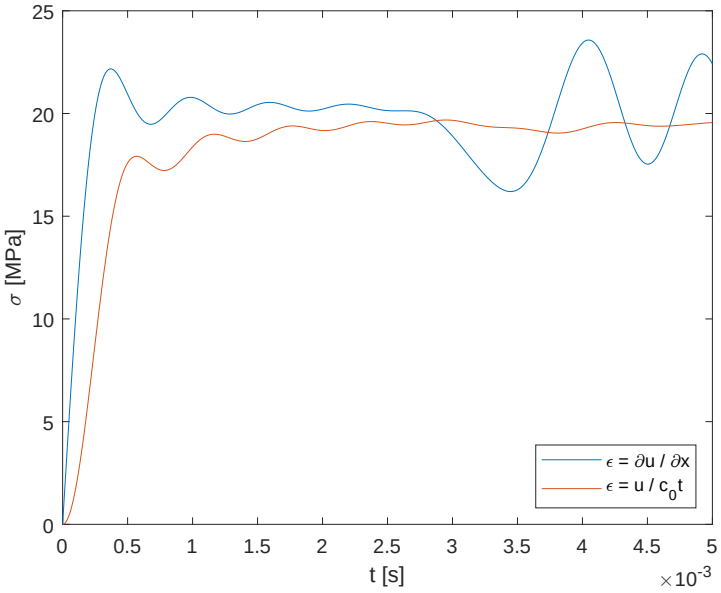

Figure 5.4: Comparison of stress obtained with different strain expressions. The stress is sampled at the interface assuming collinear impact.

From this figure, it can be concluded that the approximation as presented in Equation 5.10 corresponds to the more accurate strain definition conveniently well. Nevertheless, it remains an approximation.

The symbolic evaluation of the integral in Equation 5.8 is done using Maplesoft™ Maple 2021. Performing substitutions, including the evaluated integral, the force can now be expressed as function of z, and reads

$$\begin{aligned} F_i = &-\frac{1}{4c_0 t}\left(E\,th\,(2R-th)\left(2\pi\tan(\beta)R-\pi\tan(\beta)\,th\right.\right.\\ &-8\sqrt{z}\sqrt{\frac{2\tan(\beta)R-\tan(\beta)\,th-z}{\tan(\beta)^2\,(2R-th)^2}}\tan(\beta)R\\ &+4\sqrt{z}\sqrt{\frac{2\tan(\beta)R-\tan(\beta)\,th-z}{\tan(\beta)^2\,(2R-th)^2}}\tan(\beta)th\\ &-4\tan(\beta)R\arcsin\left(\frac{2\tan(\beta)R-\tan(\beta)\,th-z}{\tan(\beta)\,(2R-th)}\right)\\ &+2\tan(\beta)th\arcsin\left(\frac{2\tan(\beta)R-\tan(\beta)\,th-z}{\tan(\beta)\,(2R-th)}\right)-2z\pi\\ &\left.\left.+4z\arcsin\left(\frac{2\tan(\beta)R-\tan(\beta)\,th-z}{\tan(\beta)\,(2R-th)}\right)\right)\right). \end{aligned} \tag{5.11}$$

Obtaining an explicit expression for z has not been successful, making it necessary to solve the equation for each time-step implicitly. In order to solve this implicitly, iteration is required. This is performed using the *fzero* function in MATLAB, which requires a first guess for z in order to start the iteration. This first guess is determined with a more inaccurate area-indentation relation, which is much easier to solve. For this relation, z can be solved explicitly. The area-indentation relation that is used assumes the cross-section of the monopile to be a hollow square with equal wall thickness th, and the radius R being equal to the diagonals of the square. The square is rotated such that the location where the contact starts will be at the outer point of a corner of the square. Considering that z now is a function of the force at the interface, F_i, the maximum contact stress as function of time can be calculated as

$$\sigma_{i,max}(t) = \varepsilon_{i,max}(t)E = \frac{z(t)}{c_0 t}E, \tag{5.12}$$

in which $\varepsilon_{i,max}(t)$ is the maximum strain at the interface as function of time. The first objective of the contact model, describing the contact stress, is now achieved, as an expression is derived that approximates the maximum stress due to the indentation during the impact. Let us now derive the relation between force and moment.

The moment caused by this eccentric force is determined by the total force and the distance from the centerline on which that force acts. This can be represented by the total force applied on one location, being the centroid of the displaced volume. The centroid of the area is written as[1]

$$R_e = \frac{2\sin(\theta)}{3\theta}\frac{R^3 - (R-th)^3}{R^2 - (R-th)^2}, \tag{5.13}$$

but this distance does not yet account for the difference in force magnitude determined by the difference in indentation depending on the distance from the neutral line. For example, at distance R from the neutral line, the indentation is maximum, z, and at that location the force will be higher in magnitude compared to the force at distance $R - \frac{1}{2}b$, because the strains differ accordingly. To include this effect, the difference in force magnitude is incorporated by accounting for the triangular shape (looking from the side view as in Figure 5.2b) of the deformation and therefore force distribution. The eccentricity can now be written as

$$R_{e,e} = \frac{1}{3}R + \frac{2}{3}R_e. \tag{5.14}$$

Figure 5.5 shows both the area centroid and the volume centroid, of which the latter represents the location at which the net force acts. It should be mentioned that in the derivation of R_e and $R_{e,e}$ the actual geometry is considered rather than the thin-walled cylinder assumption as utilized earlier.

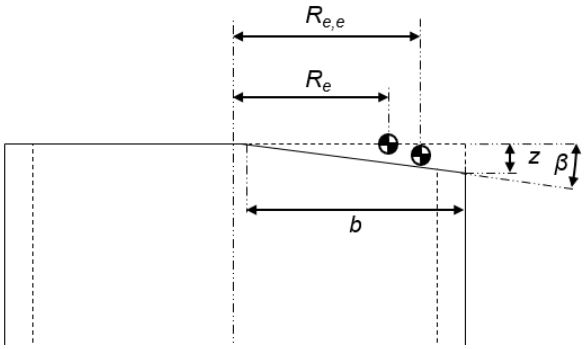

Figure 5.5: Indentation eccentricity.

There is one seemingly limitation of this contact model, although not influencing the maximum indentation stress. Due to the geometrical relations derived, this approach only holds for $z < 2\tan(\beta)R - \tan(\beta)th$, which is both physically and mathematically easily explained. Looking at the square roots in Equation 5.11, results will get complex if this condition is not satisfied. Physically this condition is trivial, since it represents the case in which b would be bigger than the diameter (diameter in the thin-walled cylinder approach, so $D - th$). Looking at the results, as will be demonstrated in subsection 5.2.3, the maximum stress will occur just after impact, within milliseconds. This is explained by the fact that the stresses will significantly decrease as the contact area increases.

Although aforementioned limitation turns out to be irrelevant, there is another assumption which does influence the validity of this contact area approach, being the assumption that the vertical set-down motions, which result in vertical indentation, remain purely vertical. Whilst the imposed moment develops, a restoring moment develops, resulting in a rotational movement of the WTG structure, such that the contact area is expected to increase even faster than described in this contact model. This effect will result in a faster decrease in indentation stress. In addition, this effect will grow stronger in

[1] https://en.wikipedia.org/wiki/List_of_centroids

time, as the moment-induced rotation needs time to develop. This makes it likely that at the instance of maximum indentation stress, this effect is minimal. Consequently, the approximated maximum indentation stress will be marginally influenced by this effect, although it loses accuracy proportional to increasing time in predicting stresses.

5.2.2. Singularity problem

In contact problems, a problem that often arises is that of singularity. For the geometric relations as assumed in subsection 5.2.1, this entails that at the instance of impact, the contact area is infinitesimally small (in the limit: $\lim_{t\to 0} A_c = 0$). This results in the contact stress theoretically approaching infinity (Barber, 2018). This is also demonstrated in subsection 5.2.3 in Figure 5.6a. This is one of the flaws of the elasticity theory, as this effect is not what physically happens. In order to remove this singularity from the contact model, a minimum contact area A_c is assumed.

This is justified when proposing that a certain amount of plastic deformation is allowed. Let us assume a maximum vertical plastic deformation of 1 mm. This means that stresses until an indentation of $z = 1$ mm is reached, are considered irrelevant. Following the geometric relations derived in subsection 5.2.1, and assuming an oblique impact angle α of 1°, this results in a minimum contact area A_c of 0.1243 m^2. This minimum contact area will govern the contact until the indentation z reaches the minimum of 1 mm, and thereafter, the contact model will determine the contact area.

5.2.3. Force input

As mentioned before, the maximum indentation stress is dependent on how fast the force develops after the instance of impact. The force input signal is obtained from the collinear impact model. This is likely to result in a faster development of the force after the instance of impact, as immediately all cross-sectional area is activated. In an oblique impact, the force will increase more gradually, as not all of the cross-section is directly activated to resist the impact. Therefore, the force obtained from the collinear impact model will most likely overestimate the slope with which the force develops.

This slope with which the force develops is influenced by changing the numerical disretization parameter Δx, hence this requires some attention. The force at the interface is, for the classical rod theory, determined using $F = AE\frac{\partial u}{\partial x}$. Results of the indentation stress are obtained for various values of Δx in order to investigate if results converge for decreasing Δx. Also, the force input following from a Rayleigh-Love rod model will be examined. Figure 5.6 shows the maximum indentation stress with the force input determined from both classical and Rayleigh-Love rod theory, for various values of Δx. It should be noted that in these plots, the proposed solution of a minimum contact area A_c is not yet included, to emphasize the singularity problem for the classical rod theory.

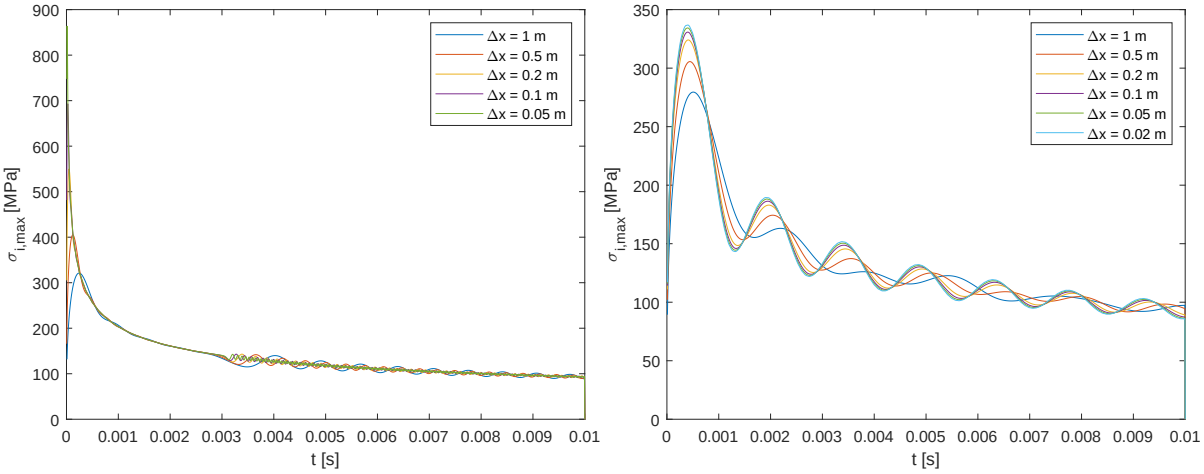

(a) Classical rod.

(b) Rayleigh-Love rod.

Figure 5.6: Maximum contact indentation stress determined from the force input for different values of Δx. The proposed solution for the singularity problem is not yet included.

As can be clearly observed, the results obtained from the classical rod force input do not seem to converge, as the stress peak tends to go to infinity for decreasing Δx. This is due to the singularity

problem. On the contrary, the resulting stress based on the Rayleigh-Love rod do converge. This is explained by the fact that the Rayleigh-Love rod inherently contains a frequency cut-off, so that frequencies higher than the cut-off cannot be described. This ensures that the peak is capped, as that would require higher frequency content. This cut-off frequency is, however, not necessarily physical, as higher frequencies can in reality be excited and propagate, according to Tsetas et al. (2021). As the precise excitation frequencies are not known without test data or exact modelling, choosing for the Rayleigh-Love rod-based results would not be justified as frequencies above the cut-off frequency are simply excluded. Therefore, it is decided to proceed with the classical rod theory force input signal, as it can describe higher frequencies, though not necessarily accurate. Results obtained from the classical rod force input, now including a minimum contact area as derived in subsection 5.2.2, are shown in Figure 5.7.

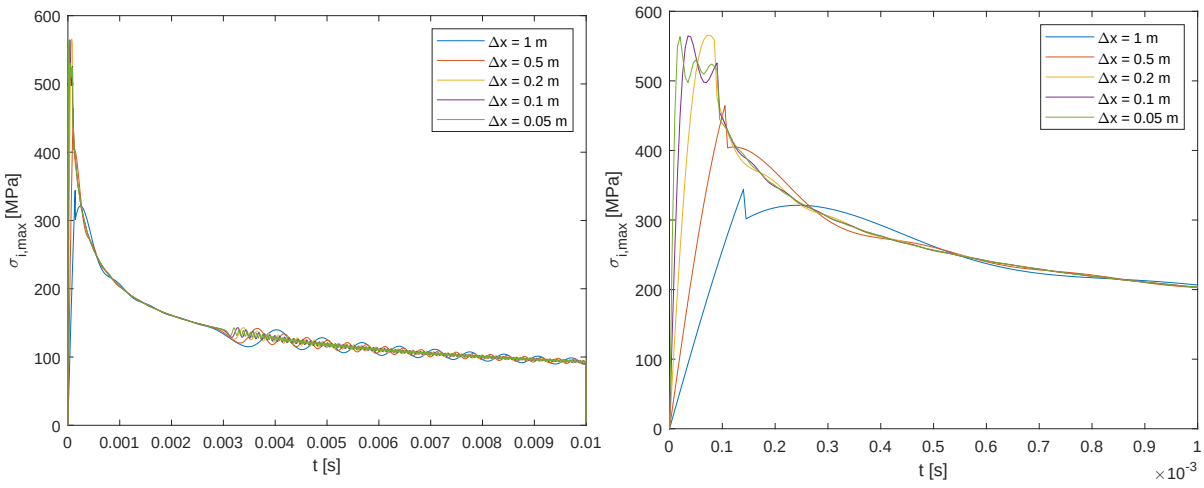

(a) Time window of 0.01 s.

(b) Time window of 0.001 s.

Figure 5.7: Maximum contact indentation stress determined from force input from classical rod theory including minimum A_c.

Now a minimum contact area is assumed, the results do converge for decreasing Δx. The sharp discontinuity that is shown, is due to the difference in stress expression between the time that the minimum contact area is governing, and the time the contact model takes over. If the minimum contact area is governing, than both the contact area and force are known, allowing for a more accurate determination of the stress. The maximum stress, as is of interest, is however not simply dividing the force by the contact area. The geometric relations have to be taken into account, as the stress at location R at the edge will be higher than the stress closer to the center of the tubular. When the contact model takes over, the contact area is not known beforehand anymore, requiring the implicit relation Equation 5.11 to determine the indentation z and A_c. This approach requires the strain approximation as presented in Equation 5.10. The peak also demonstrates that the approximation Equation 5.10 slightly underestimates the actual stress, as for a near-equal force and contact area, it returns a notably lower stress. Conversely, similar results obtained considering different input parameter values show the opposite effect. For instance, the peak distinguished in Figure 5.13 (which shows a similar stress signal but based on other input values) shows an overestimation of the contact model stress compared to when the minimum contact area is governing. This, however, can also be due to the fact that the force already reached its peak, where after the signal oscillates. Considering the frequency amplitude and the timing of the transition between minimum contact area and the contact model, this could also explain the reversed overestimation in Figure 5.13.

Another effect that can be observed in Figure 5.7 is that already after approximately 0.15 ms an indentation z of 1 mm is reached. Considering the impact velocity V_i of 1 m/s, it is not possible that the indentation z reached 1 mm so quickly. This is explained by the fact that the force input is taken from the collinear impact model, in which the force develops much faster. In other words, if the force in the oblique contact model would develop as fast as in the collinear impact model, it would require a higher impact velocity. An indentation z of 1 mm can only be reached after 1 ms at minimum (at minimum because the impact velocity of the WTG will decrease due to the impact) considering $V_i = 1$ m/s. Although

this effect distorts the time at which the peak occurs, it does not influence the approximated maximum stress value. This is an inherent limitation of assuming the force input from the collinear impact.

One aspect that is neglected until now, is material damping. In Nashif et al. (1985) it is explained that the damping is proportional to the frequency. In other words, higher frequencies will be damped out more than lower frequencies. Because the material damping can have significant influence on the results obtained from the force input signal, the effects of it are examined. In Trubat and Molins (2019) it is derived how material damping can be included in the equation of motion of a classical rod. It is based on the Kelvin-Voigt rheological model for the axial stress-strain relation, which reads

$$\sigma = E\varepsilon + \eta\frac{\partial\varepsilon}{\partial t}, \tag{5.15}$$

in which η is the material viscosity. Based on this relation, the following equation of motion is derived:

$$\rho A\frac{\partial^2 u}{\partial t^2} - AE\frac{\partial^2 u}{\partial x^2} - \eta A\frac{\partial^3 u}{\partial x^2 \partial t} = 0. \tag{5.16}$$

The viscosity can be expressed as the viscous damping ratio of steel, ξ, multiplied with the critical viscosity η_c, so that $\eta = \xi\eta_c$. The paper from Trubat and Molins (2019) presents an expression for the axial critical viscosity of a rod, which reads $\eta_c = \frac{4L}{\pi}\sqrt{\rho E}$. This expression describes the critical damping solely for the first longitudinal mode of vibration. Moreover, in the book "Vibration damping" Nashif et al. (1985), it is demonstrated that the loss factor, defined as $\eta_{loss} = 2\xi$, is proportional to frequency. Considering that the damping increases for increasing frequency, assuming this damping to be constant for all frequencies results in a conservative stress approximation. It is noteworthy to mention that it remains uncertain how applicable this damping is on such a highly transient response as of interest in this contact problem. More knowledge about material damping in impact problems would be required in order to express more confidence.

The book from Cremer et al. (2005) presents values for the longitudinal viscous damping ratio of steel, ξ, which lies approximately within 10^{-5} and 1.5×10^{-4}. Another source, Bachmann et al. (1995), mentions values for this ratio to be within approximately 10^{-3} and 2×10^{-3}, and in Nashif et al. (1985), an order of 10^{-4} and 10^{-5} is mentioned for the loss factor η_{loss}. Determining the material damping more accurately for this contact model would require more knowledge about this subject, yet, based on the previous sources, a rough approximation can be established. Let us assume ξ to be 3×10^{-4}, which lies between aforementioned values, and a substructure length L of 50 m. The contact indentation stress obtained for this damped system is presented in Figure 5.8.

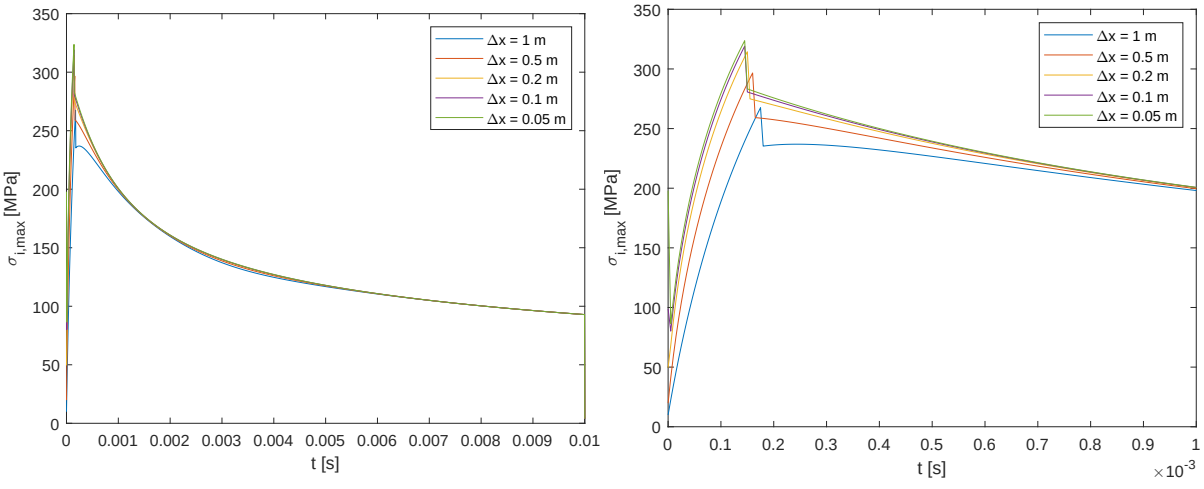

(a) Time window of 0.01 s.

(b) Time window of 0.001 s.

Figure 5.8: Maximum contact indentation stress determined from force input from classical rod theory including material damping with viscous damping ratio $\xi = 3\times10^{-4}$.

From Figure 5.8b it is observed that these results converge with decreasing Δx, as the results obtained for Δx =0.2 m, Δx =0.1 m and Δx =0.05 m already tend to shift rather close to each other. The

results obtained are significantly lower than without damping, emphasizing the importance of the actual material damping, which requires further investigation in order to arrive at more accurate damping coefficients. This is highly recommended for any subsequent research. For now, let us proceed with results obtained for $\Delta x = 0.2$ m, assuming satisfactory convergence.

5.2.4. Global model

In order to couple the impact force from the rod model to the beam model, a moment will be imposed at the interface, via the eccentricity $R_{e,e}$. Due to angle β, the contact force can be decomposed into a vertical and horizontal component. The imposed moment at the interface, for respectively the WTG tower and substructure, can be calculated as

$$-EIv''(L_1^-,t) = -EAR_{e,e}\cos(\beta)u'(L_1^-,t), \tag{5.17}$$

$$-EIv''(L_1^+,t) = -EAR_{e,e}\cos(\beta)u'(L_1^+,t), \tag{5.18}$$

in which superscript '-' means the tower interface side, and '+' the substructure interface side. Due to the horizontal component of the force, a shear force is imposed as well. This is written, respectively for the tower and substructure, as

$$EIv'''(L_1^-,t) = -EA\sin(\beta)u'(L_1^-,t), \tag{5.19}$$

$$-EIv'''(L_1^+,t) = -EA\sin(\beta)u'(L_1^+,t). \tag{5.20}$$

The boundary condition for the top of the tower considers, similarly to the axial motions, the RNA to be a concentrated inertia. The boundary conditions for the top of the tower are

$$EIv''(0,t) = 0, \tag{5.21}$$

$$EIv'''(0,t) - m_{RNA}\ddot{v}(0,t) = 0. \tag{5.22}$$

For the transverse vibrations, the beam is considered fixed at the soil, resulting in the following boundary conditions for the bottom of the substructure,

$$EIv(L,t) = 0, \tag{5.23}$$

$$EIv'(L,t) = 0, \tag{5.24}$$

in which $L = L_1 + L_2$.

The oblique impact angle is, apart from the impact-induced contact stress it induces, limited by the global stability of the WTG when impact occurs. This stability requirement prescribes that the center of gravity (COG) of the WTG may not be located, horizontally speaking, outside of the outer radius of the substructures' cross-section at the interface. When this requirement is not met, the global balance of forces on the WTG results in rotation causing the WTG to rotate downwards, away from the substructure. The orientation of the WTG is based on the worst case, where the limiting oblique angle is the smallest. This maximum oblique angle is defined by the dimensions of the WTG as in Appendix A and reads

$$\alpha_{max} = \arctan\left(\frac{1.4}{81}\right) = 0.99^\circ. \tag{5.25}$$

This maximum oblique angle is the absolute oblique angle of the WTG in order to be set-down in a stable manner. The substructure, however, also has a certain out of verticality tolerance, which has to

be taken into account as well in order to arrive at a relative maximum oblique angle, the angle between WTG and substructure at the interface. DNV AS (2021) does not specify a specific tolerance, but mentions a value of 0.25° as example. Common practice learns that the out of verticality tolerance for offshore monopiles rarely exceeds 0.25°. Hence, an upper bound of 1.25° is established, defining the angle interval from 0 to 1.25 degrees which will be considered.

5.3. Solution method

Similar to the collinear impact model, finite differences are used to approximate spatial derivatives. The equations of motions are solved using the ODE45 integrator in MATLAB. The difference in this model is that an extra set of equations, those describing the transverse vibrations, has to be solved. Considering that the imposed moment varies in time and influences the model, the imposed moment at the interface is re-calculated for each time step, within the ODE45 function. Consequently, the contact model as described in subsection 5.2.1 is solved within the ODE45 function, as it provides the eccentricity $R_{e,e}$ per time step that determines the moment.

5.4. Model validation

An attempt is made to validate the results of the contact model using FEM. An explicit, dynamical analysis is done, using solid elements near the interface (+/- 8 m from the interface), and the structure further away is constructed using shell elements. A mesh convergence study is presented in Appendix C where it is shown what order of magnitude of mesh size is required to at least capture the stress wave well. The mesh convergence as presented does not mean that all effects are converged and represent reality well, as will be later discussed. Also, because the 3D model is computationally time-intensive to run, it is chosen to start with a coarser mesh. The three meshes that are operated for the validation are shown in Figure 5.9.

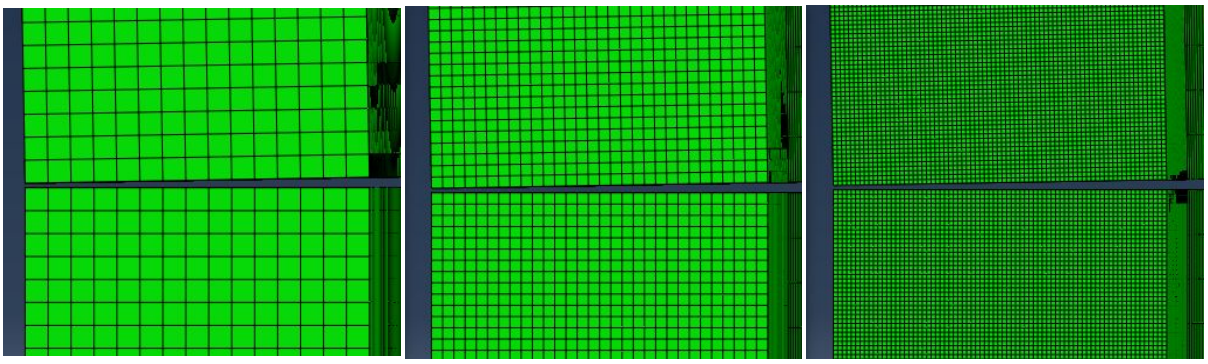

(a) Element size 5 mm. **(b)** Element size 2.5 mm. **(c)** Element size 1 mm.

Figure 5.9: FEM different mesh sizes. Point of view is on the cross-section of the tubular wall.

For computational efficiency, the structure further away from the interface is meshed less fine. This mesh distribution is such that results obtained close to the interface are not significantly affected by a coarser mesh elsewhere. This is also shown for tie-constraints and shell-to-solid constraints.

The elements from which the stress is obtained are denoted in Figure 5.10. Geometrically, element $e_{1,1}$ represents the location in which maximum stress occurs in the contact model closest to the contact surface. In the contact model, this location (where maximum indentation z is located) is at exactly the outer radius, where the element's integration point is located in the center of the element. Results for two more elements are obtained as well, namely elements $e_{1,2}$ and $e_{2,1}$. Logically these elements do not represent the equal location in the structure for different mesh size, as $e_{2,1}$ for 1 mm mesh represents the stress at a vertical distance of 1.5 mm from the interface, whereas for a mesh of 5 mm that

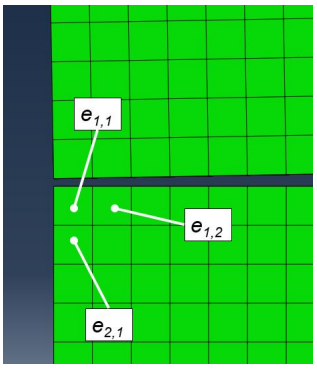

Figure 5.10: FEM elements numbering.

distance is 7.5 mm. The relevance of these two elements is to exclude the possibility that the element that makes contact first, $e_{1,1}$, causes fundamentally different results due to first contact or infinitesimally small contact area.

For the obtained results, vertical stress, denoted $\sigma_{S22,FEM}$ is obtained for the aforementioned elements, as this results in best agreement with the contact model. Figure 5.11 shows the stress obtained for $e_{1,1}$ for the different mesh sizes. Figure 5.12 shows similar results for the other two elements.

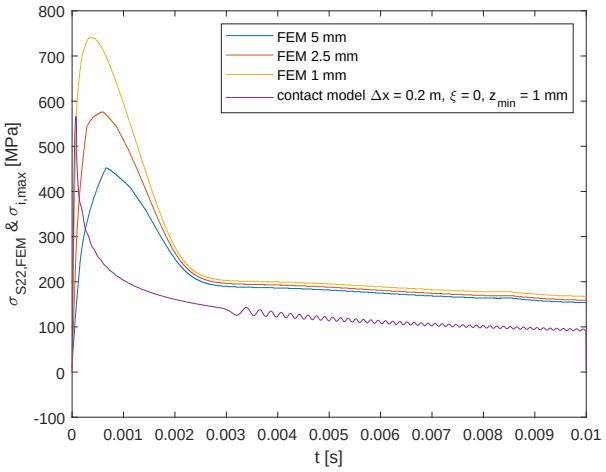

Figure 5.11: FEM stress in vertical direction in element $e_{1,1}$, denoted $\sigma_{S22,FEM}$ for different mesh size and the contact model maximum indentation stress $\sigma_{i,max}$ for $\Delta x = 0.2$ m, a minimum indentation $z = 1$ mm and no damping.

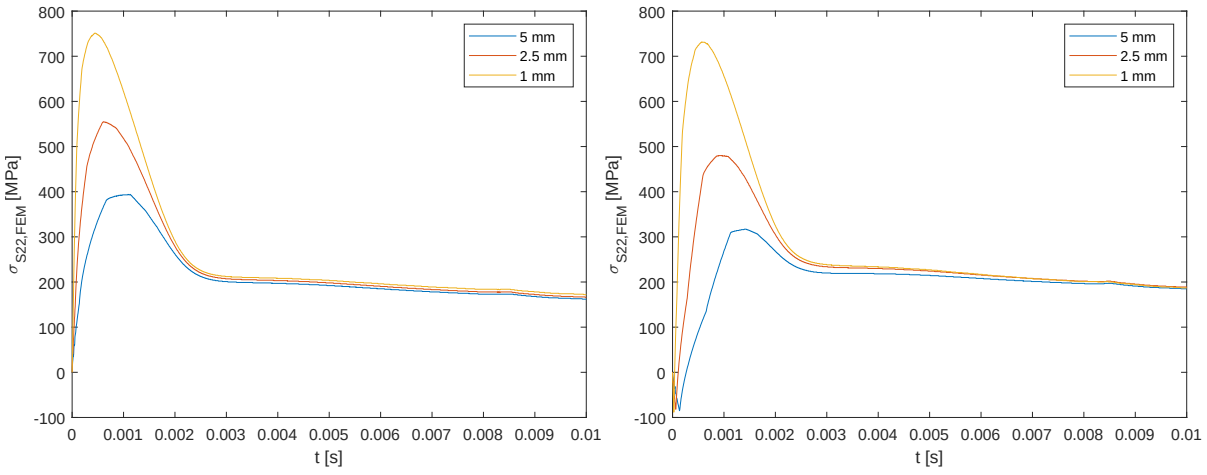

(a) Element $e_{2,1}$.

(b) Element $e_{1,2}$.

Figure 5.12: FEM stress in vertical direction in elements underneath and besides $e_{1,1}$, denoted $\sigma_{S22,FEM}$ for different mesh size.

Unfortunately, the results do not shows convergence for decreasing mesh size. This could be explained by the principle of singularity, which occurs at the instance of impact at the location where first contact takes place. This means that the closer an element gets to this location, which is a singular point, the higher the stress. In the limit, a force will be applied on a point without area, resulting theoretically in infinite stress. This explains the fact that stresses in a smaller element closer to the singularity, as is also shown in Figure 5.11, approach infinity. The singularity problem is already explained in section 2.2 and subsection 5.2.2.

Despite the fact that this FEM model does not provide accurate maximum stress values, it does shows a similar stress shape as that of the contact model, although the peak in the contact model occurs significantly faster. This was already discussed in subsection 5.2.3, where it was explained that this is an inherent limitation of the collinear impact force input assumption. Also, apart from the first

stress peak, different meshes result in converged stress after the first peak, and this stress is in the same order of magnitude as those obtained in the contact model. As improvement, material damping could be included in FEM. One way to avoid the singularity problem in FEM, could be to assume non-linear material characteristics, so that plastic strain can occur. This will limit the maximum stress to the yield stress.

5.5. Results

5.5.1. Contact indentation stress

The contact model is applied with several values of the oblique impact angle α, in the range between 0 and 1.25°. In order to find allowable impact velocity as function of α, the maximum contact indentation stress $\sigma_{i,max}$ is limited to the yield stress of 335 MPa. This examination is performed for the case without material damping, $\xi = 0$, and the case of a damping ratio $\xi = 3 \times 10^{-4}$, as derived in subsection 5.2.3. Figure 5.14 presents the maximum allowable impact velocity V_i for these cases. An arbitrary example of how the contact indentation stress develops when it is limited by 335 MPa is shown for the case without damping in Figure 5.13.

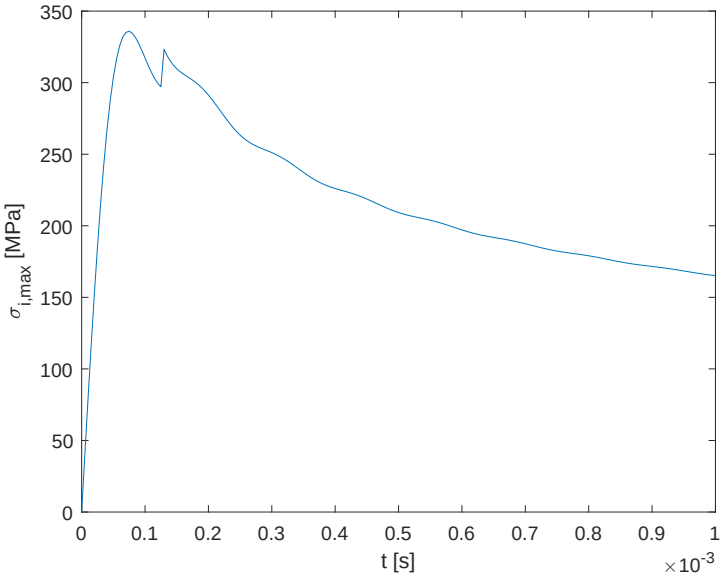

Figure 5.13: Maximum stress limited by the yield stress, $\sigma_{i,max} = 335$ MPa. This is the case for $\alpha = 0.2°$and $\xi = 0$, for which the maximum impact velocity V_i is calculated to be 1.68 m/s. The transition between the initial minimum contact area and the contact model is easily distinguished considering the distinctive discontinuity.

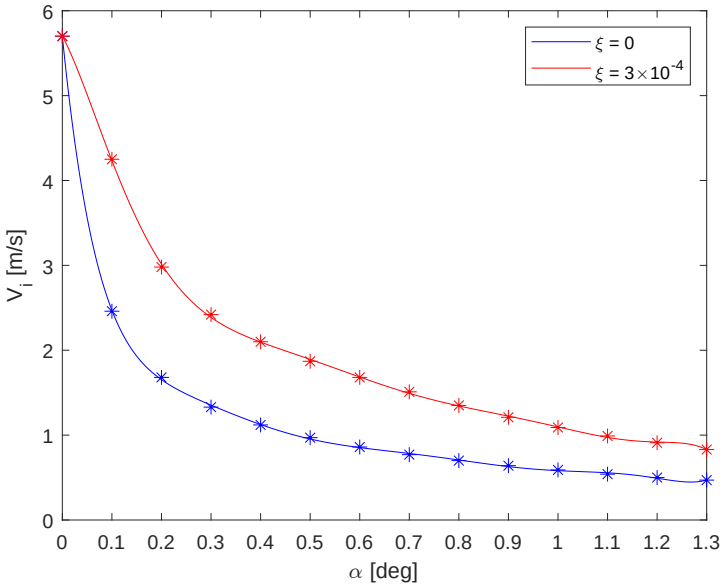

Figure 5.14: Maximum impact velocity V_i as function of oblique impact angle α defined by the maximum contact stress to be equal to the yield stress, $\sigma_{i,max} = 335$ MPa. The study is performed for a α range of 0-1.25°, but results for 1.3°are included as well. The area under the curves is the 'safe' area, whereas the area above the curves correspond to failure of structural integrity. The * symbol marks the obtained data from the model from which the fitted curve it constructed.

5.5.2. Global stress

The global stress is determined for the same conditions as assumed in the case study performed in subsection 4.4.4. This is to say that the same soil conditions, RNA mass and substructure and WTG geometry is assumed. Naturally, these parameters remain variables in the model, so that tailored results could be obtained if these conditions are known. Let us assume the impact speed, V_i, to be 1 m/s and the oblique angle, α, to be 1°. The maximum global stress, that is to say where the compressive bending stress is maximum at the cross-section, is described by

$$\sigma_{g,max}(x,t) = E\frac{\partial u(x,t)}{\partial x} - \frac{M(x,t)R}{I}. \tag{5.26}$$

Let us, once again, multiply the total stress by -1, so that compressive stresses are positive. Figure 5.15 shows the global stress as function of x and t for this case.

From this figure, it can be readily observed that maximum stresses are significantly higher than those for the collinear impact case. The maximum occurring stress in this plot is 169 MPa, where the maximum occurring stress in the collinear impact model is in the order of 78 MPa. Also, the highest stresses are to be found closer to the interface, which is explained by the fact that at that location, the moment will be maximum, as it is imposed at the interface. However, it must be noted that this model loses accuracy after approximately 0.022 s, after which the determination of the force eccentricity, $R_{e,e}$, does not hold anymore. To keep the model working, it is chosen that after that moment, $R_{e,e}$ is kept constant at the last value[2]. This will in reality not be true, as the eccentricity will continue to decrease due to neglected effects such as distribution of stresses over the cross-section and the restoring moment causing the WTG to rotate such that $R_{e,e}$ decreases even further. Therefore, although longer term results lose accuracy, this results in conservative stress approximation after 0.022 s [3], as $R_{e,e}$ is overestimated afterwards.

In order to arrive at acceptance criteria based on the global response, values for V_i and α are obtained based on a maximum global peak stress approaching yield, 335 MPa. Figure 5.16 shows the data obtained, and a curve fit to approximate intermediate values.

[2] At this moment, the eccentricity $R_{e,e}$ is solely determined by the triangular shape of the force distribution looking from the side as in Figure 5.5. $R_{e,e}$ will now be approximately 1/3 R, as can also be easily derived from Equation 5.14

[3] In this case 0.022 s, but this time varies for different values of α and V_i.

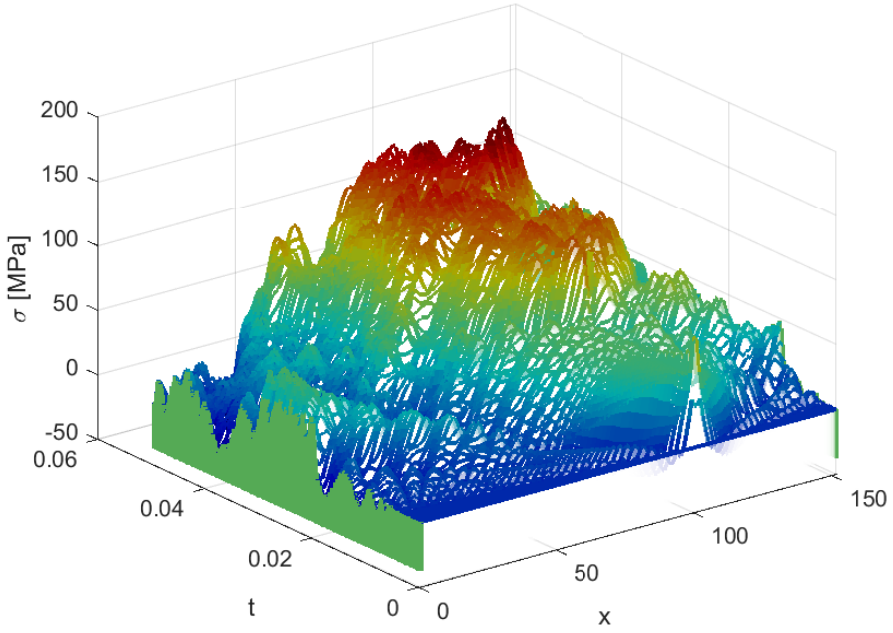

Figure 5.15: 3D plot of compressive stress σ as function of time and space for the oblique impact, time-span of 0.05 s.

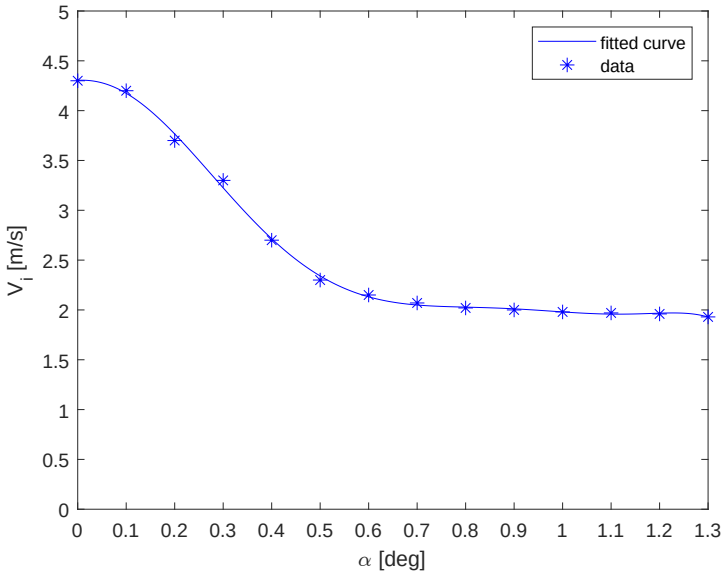

Figure 5.16: Maximum impact velocity V_i as function of oblique impact angle α limited by the maximum global stress to be equal to the yield stress, $\sigma_{g,max} = 335$ MPa. The area under the curves is the 'safe' area, whereas the area above the curves correspond to failure of structural integrity.

5.5.3. Transverse RNA accelerations

The axial accelerations at the RNA are already discussed in subsection 4.4.4. Let us examine the transverse vibrations at the RNA as well. Figure 5.17 shows the transverse accelerations, $\ddot{v}$, at the location of the RNA for the case study parameters.

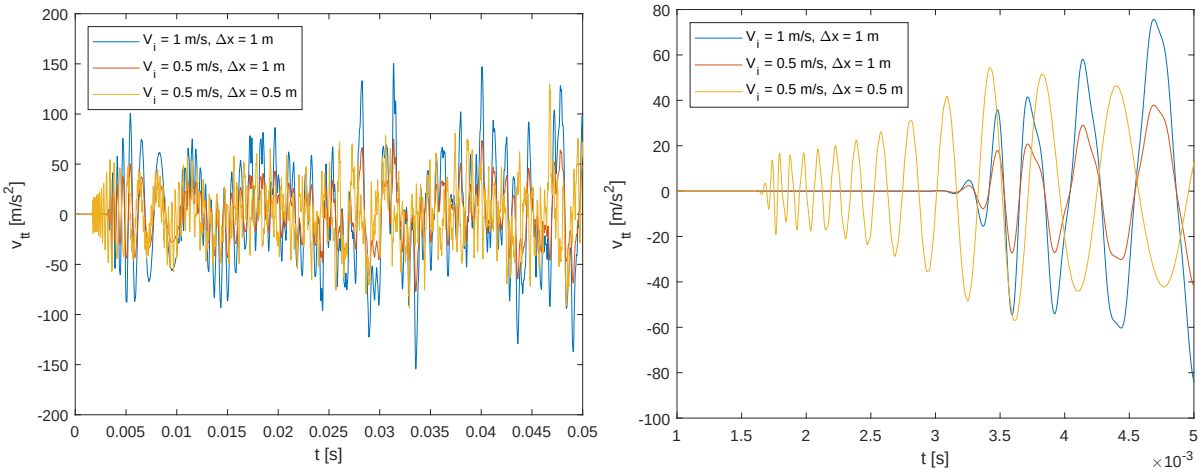

(a) Time window of 0.05 s.

(b) Time window of 0.005 s.

Figure 5.17: Transverse accelerations $\ddot{v}$ at the RNA, depicted v_{tt}.

Examining the results, it is clearly noticed that the velocity with which the flexural wave propagates is dependent on Δx. The acceleration determined for $\Delta x = 0.5$ m starts to be non-zero earlier. In fact, the flexural wave velocity is not physical anymore for high frequencies. This is explained by an important limitation of the classical (Euler-Bernoulli) beam theory. The dispersion relation in this theory allows the flexural wave group velocity to grow infinitely large as the wavenumber γ tends to infinity (Graff, 1975). As a consequence, the classical beam theory does not accurately predict the group velocity of the flexural wave for the high frequency band. The numerical parameter Δx influences the frequency of the results inversely proportional, explaining the observation of a faster propagating wave for a decreased value of Δx.

5.6. Discussion

This section contains a discussion about the most important assumptions underlying both the global and contact model. The limitations are identified and potential improvements are discussed. In general, a significant part of the discussion presented (section 4.5) for the collinear impact model also holds for the oblique impact model, as it forms a part of it. The discussion is presented specifically for the contact model and global model in subsection 5.6.1 and subsection 5.6.2 respectively. The contact model is a part of the oblique global model, so limitations or findings presented for the contact model also indirectly hold for the global model.

5.6.1. Contact model

The most fundamental assumption in the contact model is that the force is assumed as input and is obtained from the collinear impact model. The first question that arises is, how similar are the impact contact force of a collinear and oblique impact? Considering the impact force expression for an impact between two bodies of equal impedance, $F = 0.5\,ZV_i$, it can be derived that the impact force will be dependant on the impedance that is 'activated' at a certain instance after the impact. In the case of collinear impact, the activated impedance is instantly equal to the cross-sectional impedance of the structure. Assuming no variable cross-sectional area, this impedance will also remain constant. This also explains the approximate constant impact stress after the instance of impact observed in the results (for example in Figure 4.2). In the case of oblique impact, however, the impedance that is activated will increase gradually. For instance, at the instance of impact, an infinitely small contact area is present and the stress wave has not yet travelled into the material above it. The impedance at this moment is infinitely small. A very short instance later, more material above, but also besides the contact area is accelerated / decelerated, and thus gains a relative (relative to its initial velocity) particle velocity. This is due to the stiffness of the material. This way, material that does not make contact, and is located not directly above the contact area, also contributes to the impact force, as it needs to be included in the impedance. Consequently, the impact contact force will be similar to that for a collinear impact, but it will develop more gradually towards its 'maximum' value, corresponding to the instance from which the

full cross-sectional impedance contributes to the force. Because just after the instance of impact the contact area will be very small, a faster developing force will result in higher stresses. This makes for a conservative stress prediction in the time window in which the collinear force develops faster (and thus has a higher magnitude) than the actual oblique impact force. This time window, however, is expected to be extremely small, as steel is very stiff so that the activation of material not making contact will be extremely fast (stress wave speed of steel).

Another point of attention is the one-way coupling between the assumed impact force obtained from the collinear impact and the imposed moment at the interface. Currently, this force determines both the contact indentation stress (together with the geometric relations and the oblique impact angle α) and the force eccentricity $R_{e,e}$ from which the imposed moment is derived. This one-way coupling is in fact a simplification, as the imposed moment also influences the contact indentation stress. In fact, the impact force, contact indentation stress, contact area, force eccentricity and the imposed moment are all mutually dependant. In order to obtain more accurate results concerning the contact indentation stress and imposed moment, it would be required to perform an iterative calculation for each time step to assure that the forces at the contact area are in equilibrium. Without actually performing this implementation, it is unfortunately not possible to confidently predict whether the one-way coupling results in conservative or too optimistic stress approximations. This is one of the most important limitations of this contact model, and a recommendation concerning this limitation is formulated in chapter 7. This limitation also affects the oblique global model, as the imposed moment and shear force are influenced by the simplified one-way coupling.

Currently, it is assumed that the vertical indentation remains vertical. In reality, slip can occur and the WTG is likely to start rotating due to a restoring moment of the WTG (caused by gravity acting on its COG). Restricting these two degrees of freedom is conservative, as in general restricting DOF's always increases forces. The rotation will cause the contact area to increase faster, lowering contact stresses and decreasing the force eccentricity $R_{e,e}$. Taking these two DOF's into account would be more accurate, and potentially results in higher allowable impact. As restricting these DOF's is conservative, this assumption is safe.

Considering the geometric relations presented in subsection 5.2.1, one of the simplifying assumptions made is the thin-walled cylinder area approximation as presented in Equation 5.9. This approximation is not the exact contact area. Using the geometric relations for a circular segment, it should be possible to express the contact area exact, yet this proved mathematically over-complicated (in evaluating the integral as in Equation 5.8) in an attempt to do so. Especially for small contact areas this discrepancy could be significant. Due to the fact that a minimum contact area is assumed, this is less relevant. For instance, the allowed 1 mm plastic deformation and assuming an oblique angle α of 1°, correspond to an exact contact area[4] of 0.1045 m^2, and an approximated contact area of 0.1243 m^2 (as derived in subsection 5.2.2). This indicates that, although these values are not catastrophically different, the approximation overestimates the contact area, underestimating the stresses. This should be considered, as an underestimation of contact stresses does not yield conservatism. It must also be noted that for bigger oblique angles than 1°, the difference between exact and approximated contact area is expected to increase, and for smaller oblique impact angles the difference will decrease.

An assumption that is of fundamental importance for obtaining maximum allowable impact, is the minimum contact area based on allowable plastic deformation. This is currently limited by a maximum plastic deformation of 1 mm. It must be noted that this value, while considered very small compared to other geometrical values such as wall thickness and diameter, is chosen arbitrarily. This value, therefore, remains open for debate. Modifying this value will not change the model, but it will change the outcome, the allowable impact. Providing a more substantiated minimum contact area would therefore be desired. If in a certain situation it can be substantiated that maximum 2 mm plastic indentation is allowed, this would significantly increase the allowable impact. Furthermore, the occurrence of some marginal plastic deformation would, in reality, require energy from the impact. In the model, this energy

[4] This value is calculated exact using the area calculation for a circle segment $A = R^2 \arccos(1 - b/R) - (R - b)\sqrt{R^2 - (R - b)^2}$ (`https://en.wikipedia.org/wiki/Circular_segment`).

remains in the elastic stress wave. This is a conservative effect of the current modelling of this plastic deformation, as the elastic wave energy is overestimated.

The strain approximation (Equation 5.10) as derived in subsection 5.2.1 differs from the actual definition of axial strain, which is $\partial u/\partial x$ in this case. The actual strain is a differential parameter, whereas the approximation is cumulative over time. The latter of which has the limitation that the strain at a certain non-zero instance of time, is actually also determined by the approximation at the instances before it. This is what makes it cumulative. If in a hypothetical situation the actual strain would be constant in a certain time interval, both strain approximation and definition would be equal. As is observed, however, the actual strain will not be constant, so the approximation will not be equal to the actual strain as per definition. The difference between differential expression and the cumulative one also leads to the fact that the approximation is not consistently conservative or overly optimistic. It depends on what time instance which one would results in the higher stress. Figure 5.4 shows the discrepancy between strain definition and approximation for the collinear impact case, in order to indicate how much they differ. It is observed that the approximation, as just explained, is not necessarily conservative. In fact, considering this example (Figure 5.4), the strain approximations does actually underestimate the stress compared to the actual stress from $t = 0$ s until $t \approx 3$ ms. On the other hand, the approximation results in an overestimation of maximum contact stress in the example presented in Figure 5.13. This strain approximation is a limitation of the model, and should therefore be considered. Also, it is not necessarily the case that this discrepancy is of equal order for all other situations. Still, Figure 5.4 does indicate that the approximation, while underestimating the stress in the beginning, still provides a decent approximation, which is also emphasized while discussing the results obtained from the models. Moreover, when the discrepancy between actual and approximated stress is the largest (just after the instance of impact, while the force still develops with a steep slope), the minimum contact area is governing allowing the actual stress to be calculated.

Finally, the effects of material damping are demonstrated. Although the precise implementation of the material damping is questionable, the results indicate its potential significant influence on the maximum contact stress. First, the critical damping is currently calculated from an expression applicable for the first longitudinal mode of vibration of a rod. Actually, the damping is proportional to the frequency, so that higher modes of vibration would be exposed to more damping than the first mode. Therefore, this would make for a conservative critical damping calculation in the contact model. The actual applied damping in the model is not only dependant on this critical damping, but also on a damping ratio for steel. Determining an accurate damping ratio for the system in this thesis is not straight forward, and the examined literature only provides wide ranges of ratios. Therefore a value was approximated from these ranges as $\xi = 3\times10^{-4}$ in order to proceed with. More so, the applicability of the damping for this highly transient behaviour remains uncertain. Approximating the maximum contact indentation stress taking material damping into account more accurately would require more knowledge. Still, the results obtained including material damping demonstrate the significant increase of allowable impact, and therefore is an important recommendation for successive research.

5.6.2. Global model

The transverse vibrations in the global model are described by an Euler-Bernoulli beam. One of the assumptions in this beam theory is that the bending stress is distributed linearly over the cross-section of the beam. Close to the interface, therefore, the imposed moment and shear would theoretically cause a linearly distributed bending stress, but this will in reality not be the case. Theoretically, the maximum compression stress caused by the bending moment will be equal in magnitude to the tension stress on the other side. In reality, this will not be true, as a tension at the free ends at the interface of both structures is not possible. Further away from the interface, the bending stress will be more linearly distributed due to redistribution of stresses over the cross-section.

In addition to what already was discussed in section 4.5, boundary / soil conditions for the transverse vibration could also be improved. Currently, no transverse soil conditions are considered (currently the transverse motion of the bottom tip of the substructure is fixed), while it is expected that these will extract energy from the flexural wave propagation and thus also decrease the reflections. Therefore, the current model is conservative, but increasing accuracy of the boundary conditions could lower the

predicted stresses and accelerations in the system.

Another limitation is that accuracy of the model decreases over time, partly due to the limits of the geometrical relation that determines $R_{e,e}$, and partly because rotation of the WTG is not included. After a longer time period than 0.05 s, it is possible that the WTG will lose contact with the substructure, although this is physically not necessarily the case due to neglected forms of damping in the system.

The results obtained from the oblique models represent rough approximations of the stresses and accelerations. Considering all the assumptions as just discusses, it can, unfortunately, not be confidently stated that the results present conservative approximation. Most of the assumptions yield conservatism, but it is hard to determine whether they sufficiently compensate the non-conservative assumptions. This is a limitation of the oblique models as they currently are, and therefore should be regarded when interpreting the results.

5.7. Conclusion

The oblique impact model was constructed in order to take into account a non-zero oblique impact angle. The functionality of it is twofold; describing global stresses and accelerations and approximating the maximum contact stress. Two dedicated models are constructed, the global and contact model, and the global model is coupled to the contact model by the force eccentricity determined in the latter. For the examination of the global stresses and accelerations, the collinear impact model is appended with classical beams describing the transverse motions. In this way, an oblique-impact-induced bending moment and shear force can be imposed at the interface, influencing the global response significantly.

The contact model (subsection 5.2.1) offers the ability to approximate the contact indentation stresses shortly after the instance of impact. It approximates the maximum peak stress at the location where the contact starts as function of α and V_i. Considering the stress requirement (determined in chapter 3), allowable impact is obtained expressed in allowable impact speed V_i as function of α. Various important limitations and findings of this model and its limitation were discussed in section 5.6. The most important conclusion of the limitations is that the model does not necessarily yield conservatism in the results obtained, but still approximates the contact stress reasonable well. Also the importance of material damping was identified.

The global model (subsection 5.2.4) is able to describe global stresses and accelerations occurring due to the oblique impact for variable oblique angle α and impact speed V_i. Considering the stress requirement, allowable impact in terms of V_i and α were obtained limited by the global stresses not exceeding the yield stress. It was also demonstrated that the RNA acceleration requirement imposes even more stringent allowable impact velocity: for the maximum oblique angle, the allowable impact speed is 0.09 m/s. This indicates that the RNA acceleration currently limits the allowable impact. Several important limitations concerning the oblique impact global model and contact model were identified and discussed in section 5.6.

The results for the allowable impact limited by the stress requirement for both contact and global stress are presented in Figure 5.18. The allowable impact is presented in terms of oblique impact angle α and impact speed V_i. The area under the curve represents the allowable region. The results indicate that only for very small oblique angles the global stress is governing. The maximum allowable impact velocity as function of oblique impact angle limited by the allowable acceleration requirement of 1.5 g is presented in Figure 5.19.

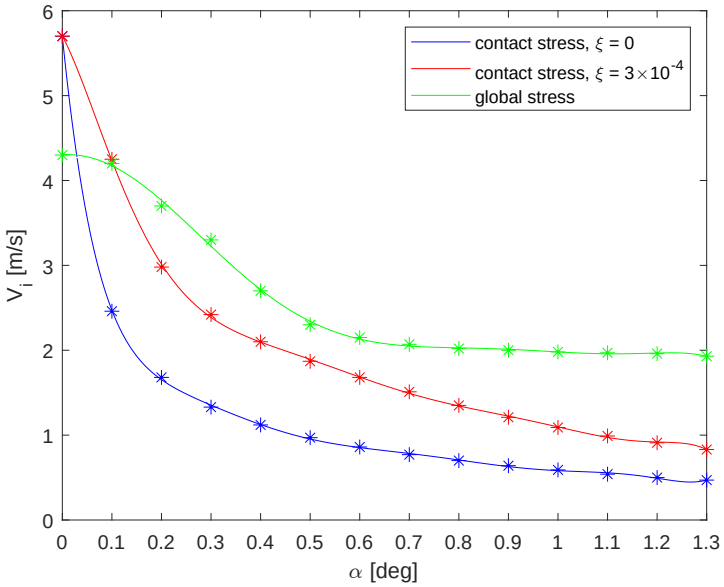

Figure 5.18: Maximum impact velocity V_i as function of oblique impact angle α limited by the maximum global and contact stress to be equal to the yield stress, $\sigma_{i,max} = \sigma_{g,max} = 335$ MPa. The area under the curves is the 'safe' area, whereas the area above the curves correspond to failure of structural integrity. The * symbol marks the obtained data from the model from which the fitted curve it constructed.

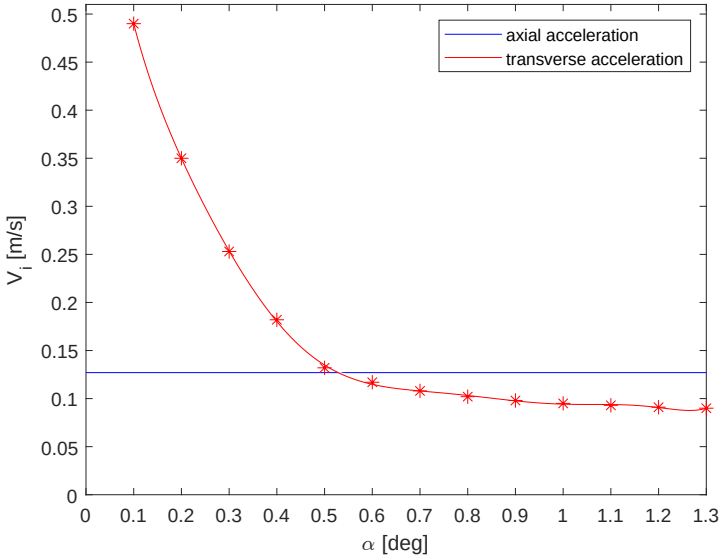

Figure 5.19: Maximum impact velocity V_i as function of oblique impact angle α limited by the maximum axial and transverse acceleration of 1.5 g (approximately 14.7 m/s^2). The area under the curves is the 'safe' area, whereas the area above the curves correspond to failure of structural integrity. The * symbol marks the obtained data from the model from which the fitted curve it constructed. A value for the transverse acceleration for the case of zero oblique impact angle is not included, as this would theoretically be infinitely high.

Considering all the assumptions made, the results only roughly approximate the real maximum occurring stresses and RNA accelerations. Therefore, allowing impact close to the limit would be questionable. On the contrary, when it is known for instance that the set-down speed V_i will be at maximum 0.1 m/s and the oblique angle α will not exceed 1°, these results demonstrate with quite some confidence that this would not cause a failure of structural integrity of the WTG and substructure and their flanges considering the yield stress requirement. It must be noted that the acceleration requirement, now defined by a maximum of 1.5 g, is much more stringent in this case, limiting the allowable impact.

6

Conclusion

The broader research field of offshore wind installation, of which the problem researched in this thesis is a part, is one that will only continue to draw more and more attention in the decades ahead. As a consequence of increasing awareness of the severity of global warming for life on earth, renewable energy sources have gained elevated interest. Of these, offshore wind is one of the most popular and fast-growing source. Wind turbines become increasingly larger, and the available space for offshore wind farms shifts to deeper waters. Hence, installation using the SSCV Thialf becomes increasingly competitive. As explained in chapter 1, the set-down stage of wind turbine installation, in which the WTG is installed onto the substructure, is a critical step in the installation sequence of offshore WTG's. The disadvantage of WTG installation with a floating vessel is that the motions of the WTG, while lifted, are partly unpredictable. This can cause significant impact between WTG and substructure during touch-down. Therefore, knowledge about the allowable impact is highly valued, as it determines the operational window. Following from this, the problem under consideration in this thesis was formulated in section 1.2. The objective of this research is to determine the allowable impact ensuring sufficient structural integrity. The main research question arising from this problem statement and objective was formulated as: ***"During WTG-substructure touch-down, what is an convenient-to-check acceptance criterion for the landing loads that ensures sufficient structural integrity of the impacting structures?"***.

Aiming to determine the impact, it was first evaluated in chapter 2 how the impact and the impacting structures can be modelled with both convenience and sufficient accuracy. Several models were discussed, and the pro's and cons qualified. It was concluded to proceed with classical rod theory and Rayleigh-Love rod theory to model the collinear impact model with, and the classical beam theory to complement the oblique impact model by accommodating bending and shear (by describing transverse motions). Various effects such as stress wave propagation, material behaviour and stress concentrations were examined.

In chapter 3 the structural integrity requirements were investigated. After all, without requirements, no acceptance criteria can be formulated. The focus was on codes and standards that are commonly practiced in the offshore wind industry, but also client specific requirements, such as maximum accelerations were discussed. The most important conclusion was that in this thesis, the design stress shall not exceed the yield stress. In reality, this does not have to be the case, as specific codes can require load or material factors to be applied in accordance with the LRFD design method. The implementation of load or material factors, however, does not affect the models constructed in this thesis, and can easily be included accordingly. Besides the maximum stress requirement, it was concluded that in this thesis a maximum allowable RNA acceleration of 1.5 g is assumed. This value, however, heavily depends on the turbine manufacturer. It should be noted that in this thesis, the focus is on the stress requirement, as was determined in chapter 1, but the RNA accelerations turned out to be the limiting factor for the allowable impact.

The collinear impact model was constructed in chapter 4. It forms the basis for the oblique impact

model, and it provides insight into the influence of parameters such as a variable cross-sectional area, RNA mass, soil conditions and lateral inertia. The results were successfully cross-checked with a corresponding FEM analysis, increasing confidence in the results obtained. Similarly, it demonstrated that the FEM model works properly, as its results comply with the models and the theory. It was also shown that stress wave reflections from the boundaries are rather significant, and undoubtedly need to be considered when obtaining maximum occurring stress in the system. For instance, in the case study performed in subsection 4.4.4 is was demonstrated that the maximum occurring stress was, for most part due to reflections, about three times higher than the stress induced by the impact at the interface. It was also demonstrated that the maximum stress does not necessarily occur at the interface. In section 4.5 is was discussed that the collinear impact model yields conservative stress approximations.

In reality the collinear impact is highly improbable, as the WTG will almost certainly impact the substructure with a non-zero oblique angle α. (explained in chapter 1). The contact area during impact will now be highly variable, and is initially very small. Hence, it was expected that contact stresses in the oblique impact are significantly higher than those in the collinear impact. This expectation led to the demand for a model that accommodates for contact stresses, and also describes a different global response. After all, the oblique impact causes an imposed moment and shear force at the interface, as the contact force will act with an eccentricity with respect to the center of the cross-section. The oblique impact, presented in chapter 5, consists of two dedicated models, being the contact model and the global model. These are one-way coupled, as the eccentricity that determines the imposed moment in the global moment is derived in the contact model. The fundamental assumption of the contact model (subsection 5.2.1) is that the force signal is obtained from the collinear impact and assumed as input. This model is able to approximate the maximum contact indentation stress. One problem that arose is that a singularity at $t = 0$ s occurred. This would theoretically result in infinitely high stresses. This problem was solved by assuming a non-zero minimum contact area, based on allowing a marginal amount of plastic deformation (1 mm currently). It was found that the influence of material damping on the contact stresses is significant, yet difficult to determine its accuracy of applicability on the impact under consideration. Applying material damping more confidently requires more research, but would be highly recommended (This will be more thoroughly explained in chapter 7). Assuming damping for the first longitudinal mode of vibration, a conservative estimate (although it is not known whether the damping ratio ξ was also taken conservative) was done to investigate the influence. This showed maximum stresses nearly twice as low compared to the zero damping case. When no further information about material damping is known, the zero damping case serves as a good conservative estimate. Considering all assumptions made in this contact model, it can be confidently concluded that it approximates an order of magnitude of maximum contact stresses, but unfortunately it is not concluded that the model yields conservative stress approximations. A more detailed discussion about the underlying assumptions, limitations and findings was presented in section 5.6. Especially the one-way coupling instead of an iterative coupling and the strain approximation (Equation 5.10) simplifications are not necessarily conservative. On the other hand, other assumptions, such as the collinear impact model force input and the zero material damping case are conservative. It is hard to determine whether all assumptions combined result in consistent conservative approximations, and improvement of the models or validating the obtained results would be required to examine the overall conservatism of the contact model. This is a significant limitation of the current contact model, and should therefore be considered while interpreting the results.

The eccentricity $R_{e,e}$ calculated in the contact model determines the moment that is imposed at the interface. This is the input for the global model, presented in subsection 5.2.4. Appending with a classical beam, transverse motions can be described in addition to the axial vibrations. This allows for flexural waves (bending) to propagate through the structures as well. Performing the same case study as presented for the collinear impact, it was demonstrated that maximum occurring stresses could easily be twice as high when bending stresses were taken into account. One effect that is not included in the model, is the rotation of the WTG after impact. This effect could significantly reduce the imposed moment, as the eccentricity reduces much faster due to the rotation. The global models allows for case-specific stress approximations, where parameters like the RNA mass, tower length, soil stiffness and damping and variable cross-sectional area are all easily modified. The assumptions underlying this model where thoroughly discussed in section 5.6.

Considering the results presented in Figure 5.18, the global stress is only limiting the allowable impact (considering the stress requirement) when the oblique impact angle is very small. For the maximum possible oblique angle α, the case without material damping ($\xi = 0$) approximates an allowable impact speed of $V_i = 0.47$ m/s. Common practise in WTG installation learns us that this speed is already rather high. For instance, if during the set-down stage a maximum vertical set-down speed of 0.1 m/s can be guaranteed, these results do show rather confidently that no damage to the structural integrity governed by the stress requirement defined in this study is expected. Logically, this holds for inputs assumed (such as WTG and substructure geometry), and for example, the contact model allowed for maximum 1 mm plastic deformation. In pursuance of more accurate stress approximations, recommendations are formulated on how to improve the model in chapter 7. The approximated accelerations of the RNA presented in subsection 4.4.5 and subsection 5.5.3 results in significantly more stringent allowable impact. Where the worst case scenario regarding the stress requirement limits the allowable impact velocity to 0.47 m/s, the maximum acceleration requirement yields a limit of approximately 0.09 m/s. This indicates that, although the acceleration requirement depends on the turbine manufacturer, the acceleration requirement of the RNA currently governs the maximum allowable impact. This is an essential finding of this thesis. The RNA point mass assumption and the conservative implementation of damping in the system (for example neglecting material damping and distributed soil damping) ensure that the RNA acceleration approximations are sufficiently conservative.

Returning to the research question, the acceptance criterion is expressed most conveniently in terms of impact speed V_i and oblique impact angle α. The results are presented both limited by the stress requirement and acceleration requirement respectively in Figure 5.18 and Figure 5.19. These kinematic parameters are convenient to check in hydro-dynamic global models of the installation procedure.

The insights and results gained during the research are valuable for HMC, as they present approximations for occurring stresses in the substructure and WTG, and accelerations in the RNA. The results allow HMC to determine in which conditions they are still confident about installing the WTG onto the substructure, and under which conditions not. On a higher level, this allows HMC to install WTG's more efficiently, strengthening their position in the offshore wind floating installation market, which is expected to only grow further in the future. Returning to the context this problem arose from, developments like this thesis enable faster and more efficient installation of wind turbines. This potentially ensures a faster and cheaper realization of green energy sources, speeding up the progress towards a CO2 neutral energy system, which is an important part of the ambitious climate goals set in the 2016 Paris Agreement.

7

Recommendations

Based on the findings of the thesis, recommendations for successive research are formulated in this chapter. A relevant finding, for instance, is that conservatism of the results obtained from the contact model (subsection 5.2.1) cannot be assured due to the simplified approach currently utilized. This is a significant limitation, and a recommendation is formulated that could reduce or eliminate this limitation. A more extensive examination of these findings, opportunities or limitations was presented in the discussions section 4.5 and section 5.6. In this chapter, the most important recommendations following from these findings are presented.

Contact model one-way coupling

In section 5.6 it was discussed that a significant limitation of the contact model is that it assumes the one-way coupling between force input, force eccentricity and imposed moment. It was also explained that this simplification does not necessarily result in conservatism of the results, allowing for a potential underestimation of approximated contact stresses. This potential underestimation limits the model, as conservatism of the obtained contact stresses cannot be confidently assured.

Currently, the force at the interface is obtained from the collinear impact model. Together with the geometric relations and other underlying assumptions, it determines the contact stress and force eccentricity $R_{e,e}$. This eccentricity combined with the force input determines the imposed moment at the interface. This approach inherently assumes that the calculated contact stress is independent from the imposed moment. In reality, this is not true, as the moment contributes to the contact stress as well. In fact, the contact stress, bending moment, impact force, contact area and force eccentricity are all mutually dependant. Obtaining the equilibrium value of these parameters per time step would, therefore, require an iterative calculation per time step. The implementation of this iterative contact definition is expected to be rather complex, and requires additional knowledge about contact mechanics and contact definition (for example via Lagrange multipliers). Failing to assure sufficient conservatism in the results obtained entails a significant limitation of the contact model, and therefore this thesis. Therefore, the consideration of the mutual dependency is recommended.

Material damping

One aspect that was not considered in the global models, but was included in the contact model, is material damping. Although the current method of applying material damping is questionable and requires more knowledge in order to be more accurate, the results obtained from the contact model both with and without material damping included demonstrate the significant influence of material damping on the maximum stress. Because this influence is substantial, taking into account material damping more accurately could result in significantly less stringent allowable impact. For instance, considering the results presented in Figure 5.7 and Figure 5.8, it is observed that the maximum stress occurring in the case without damping is nearly twice as high compared to the case in which damping is included ($\xi = 3 \times 10^{-4}$).

Currently the damping is based on the critical damping corresponding to the first longitudinal mode of vibration, which, as explained in subsection 5.2.3, is conservative. On the other hand, it remains unclear

how applicable this expression is in a highly transient impact, as a broad spectrum of frequencies is excited in such an impact. Investigating this accuracy of application is therefore recommended. Also, implementing material damping more accurately for this impact is recommended. Besides the implementation of the critical damping, obtaining a more accurate value of the damping ratio of steel is recommended. Currently, the value for the damping ratio ξ is estimated based on ranges obtained from various literature.

The phenomenon of material damping was not taken into account in the global models. The significant influence of the material damping as observed in the results obtained from the contact model, therefore, implicate that including it properly in the global models is worth investigating. Potentially, this could result in lower stresses and accelerations in the WTG and substructure, and hence result in higher allowable impact.

Accelerations

One of the most important findings of the allowable impact results limited both by the stress requirement and acceleration requirement, is that the latter results in significantly more stringent allowable impact. The maximum RNA acceleration therefore limits the allowable impact. Considering the most severe case, a maximum impact velocity of 0.09 m/s is allowed, which is rather stringent as realistic set-down speeds are in this order. For this reason, it is recommended to further investigate and improve the acceleration modelling and requirement, in order to obtain a less stringent allowable impact regarding the acceleration requirement.

First of all, the maximum acceleration requirement is not as properly defined as the stress requirement, as maximum accelerations are prescribed by the turbine manufacturer and not any classification society. Therefore this requirement is dependant on the turbine manufacturer. Currently, a maximum acceleration of 1.5 g is assumed. Defining a more substantiated acceleration requirement therefore is recommended, as less stringent acceleration requirements could significantly improve the allowable impact. For instance, what equipment exactly is imposing this requirement, and can the requirement be less stringent by incorporating for example some RNA geometry or if possible some equipment suspension. Moreover, the RNA is currently modelled as point mass, which results in conservative predicted accelerations. Including the RNA geometry could potentially result in lower accelerations of the limiting equipment. How this should be done is not yet investigated, but is worth considering in successive research.

Global model accuracy

Soil conditions

Currently the soil conditions are implemented in the global models rather simplified. Various sources of stiffness and damping are not taken into account, such as water damping and distributed soil conditions alongside the substructure below mudline, resulting in a conservative implementation of those conditions. While conservative, implementing more sophisticated soil conditions could result in significantly lower stress wave propagation and reflections. This potentially results in lower maximum stresses and accelerations in the system, hence more favourable allowable impact. This can also potentially eliminate the currently emerging disconnection between WTG and substructure after impact in the collinear impact case (this phenomenon was discussed in subsection 4.4.4). For these reasons, it is recommended to improve the accuracy of the implemented soil conditions.

Rigging arrangement

Also the rigging arrangement is currently implemented in the models in an oversimplified manner. The whole rigging arrangement is now modelled as springs, representing the LLT and cable stiffness. As explained in chapter 1 and section 4.5, the actual rigging arrangement entails much more components, such as a passive heave compensation system. In section 4.5 it was also explained that gravity should be included in order to be able to include this rigging arrangement more accurately. Improving the rigging arrangement modelling results in a more accurate system representation in general, as it takes into account sources of inertia, damping and stiffness that are currently simply ignored. It is hard to predict its influence on the maximum stresses and accelerations in the system, and therefore alone would be an improvement, and is therefore recommended.

Rotation & slip

Another recommendation considers the WTG rotational movement and slip due to an oblique impact. Right now, these degrees of freedom are restricted, which is conservative as explained in section 5.6. The induced moment causes the WTG to rotate such that the contact area will increase (and thus the force eccentricity $R_{e,e}$ decrease) faster than the model predicts. The exclusion of rotation is conservative, but including it would be more accurate. This potentially provides for lower maximum contact stresses, and thus higher allowable impact. Including these degrees of freedom in the models, for that reason, potentially results in more favourable allowable impact, and is consequently recommended.

Oblique model validation

Due to limited time, it was decided that the global results were not cross-checked with results obtained from FEM. Axial vibrations were validated in the collinear impact model, but the bending moment, which globally entails the biggest difference between oblique and collinear impact, is not. The FEM cross-check of these results is recommended to increase the confidence in results obtained from the oblique impact global model.

Considering the validation of the results obtained from the contact model, it is recommended to further investigate how to use FEM to validate these. Right now, a singularity occurs at the location of interest, resulting in increased stress for decreased mesh size. After the singularity (first peak in stress results), the stress does converge for decreasing element size, and shows a similar shape as those obtained from the contact model. Also, they converge towards a stress level in the same order of magnitude. It would also be very valuable to validate the results obtained from the contact model with test data.

Flange detail and positioning tolerance

Due to a lack of time, it was decided to not consider the positioning tolerance as explained in chapter 1. In section 4.5 is was explained that a non-zero positioning tolerance would result in higher maximum stresses at the interface considering collinear impact. The influence of this non-zero positioning tolerance on the oblique impact model has not been identified, and therefore it is recommended to investigate the effects of this tolerance on the maximum contact stress, as it cannot be ruled out that it does not impose more stringent allowable impact.

For the same reason the positioning tolerance was not considered, the precise flange geometry was not taken into account. In section 2.4 it was explained that a SCF could potentially occur in the flange neck, and therefore result in significantly higher peak stresses in the flange. For the collinear impact, this SCF could potentially result in the limiting stress, determining the allowable impact. For the oblique impact contact model it is not expected that this SCF will govern the maximum occurring stress. This is due to the maximum stress currently occurring already in a highly concentrated and small area. As the precise effects of the flange geometry on potential stress concentrations is not identified, but it can be existent in reality, it is recommended to investigate the potential stress concentrations in successive research.

References

Achenbach, J. D. (1975). *Wave Propagation in Elastic Solids*. Elsevier.

Bachmann, H., Ammann, W. J., Deischl, F., Eisenmann, J., Floegl, I., Hirsch, G. H., Klein, G. K., Lande, G. J., Mahrenholtz, O., Natke, H. G., Nussbaumer, H., Pretlove, A. J., Rainer, J. H., Saemann, E.-U., and Steinbeisser, L. (1995). Vibration Problems in Structures. *Vibration Problems in Structures*.

Barber, J. (2018). *Contact Mechanics*, volume 250 of *Solid Mechanics and Its Applications*. Springer International Publishing, Cham.

Berkowitz, H. M. (1963). Longitudinal Impact of a Semi-Infinite Elastic Cylindrical Shell. *Journal of Applied Mechanics*, 30(3):347–354.

British Standards Institution (2005a). Eurocode 3 EN 1993-1-1: Design of steel structures. Technical report, BSI, London.

British Standards Institution (2005b). Eurocode EN 1990: Basis of structural design. Technical report, BSI, London.

British Standards Institution (2006). Eurocode 3 EN 1993-1-5 Design of steel structures - Part 1-5: Plated structural elements. Technical report.

British Standards Institution (2007). Eurocode 3 EN 1993-1-6: Design of steel structures - Part 1-6: Strength and stability of shell structures. Technical report.

Cremer, L., Heckl, M., and Petersson, B. A. (2005). Structure-borne sound: Structural vibrations and sound radiation at audio frequencies. *Structure-Borne Sound: Structural Vibrations and Sound Radiation at Audio Frequencies*, pages 1–607.

Deeks, A. J. and Randolph, M. F. (1993). Analytical Modelling of Hammer Impact for Pile Driving. *International Journal for Numerical and Analytical Methods in Geomechanics*, 17(5):279–302.

DNV AS (2017). DNV-ST-0054 Transport and installation of wind power plants. Technical report.

DNV AS (2018). DNV-ST-N001 Marine operations and marine warranty. Technical report.

DNV AS (2019a). DNV-OS-C101 Design of offshore steel structures, general-LRFD method. Technical report.

DNV AS (2019b). DNV-RP-C203 Fatigue design of offshore steel structures. Technical report.

DNV AS (2019c). DNV-RP-C208 Determination of structural capacity by non-linear finite element analysis methods. Technical report.

DNV AS (2021). DNV-ST-0126 Support structures for wind turbines. Technical report.

Galambos, T. V. and Ravindra, M. (1981). Load and Resistance Factor Design. *Engineering Journal, AISC*, 18(3).

Graff, K. F. (1975). *Wave Motion in Elastic Solids*. Dover publications inc.

Han, S. M. and Benaroya, H. (2002). *Nonlinear and Stochastic Dynamics of Compliant Offshore Structures*, volume 98. Springer Science & Business Media.

Heerema Marine Contractors, H. (2021). Internal sources.

International Energy Agency (2021). Renewables 2021 - Analysis and forecast to 2026.

Kolsky, H. (1964). Stress Waves in Solids. *Journal of Sound and Vibration*, 1(1):88–110.

Meijers, P. C., Tsouvalas, A., and Metrikine, A. V. (2017). The Effect of Stress Wave Dispersion on the Drivability Analysis of Large-Diameter Monopiles. *Procedia Engineering*, 199:2390–2395.

Meijers, P. C., Tsouvalas, A., and Metrikine, A. V. (2018). A non-collocated method to quantify plastic deformation caused by impact pile driving. *International Journal of Mechanical Sciences*, 148:1–8.

Metrikine, A. V. and Vrouwenvelder, A. C. W. M. (2018). Dynamics of Structures - CT4140 Part 2 Wave Dynamics. Technical report.

Musial, W., Spitsen, P., Beiter, P., Duffy, P., Marquis, M., Cooperman, A., Hammond, R., and Shields, M. (2021). Offshore Wind Market Report: 2021 Edition. Technical report, National Renewable Energy Lab.(NREL), Golden, CO (United States).

Nashif, A. D., Jones, D. I., and Henderson, J. P. (1985). *Vibration damping*. John Wiley & Sons.

NORSOK (2004). N-004 Design of steel structures. Technical report.

NORSOK (2020). N-001 Integrity of offshore steel structures. Technical report.

Parola, J. F. (1970). *Mechanics of impact pile driving*. University of Illinois at Urbana-Champaign.

Pilkey, W. D. (1997). *Peterson's stress concentration factors*. John Wiley & Sons, second edition.

Ramirez, L., Fraile, D., and Brindley, G. (2020). Offshore Wind in Europe. Technical report, WindEurope.

Smith, E. (1960). Pile-Driving Analysis by the Wave Equation. *Transactions of the American Society of Civil Engineers*, 127(1):1145–1171.

Smith, E. A. L. (1950). Pile driving impact. Proceedings, Industrial Computation Seminar.

Smith, W. F. and Hashemi, J. (2006). *Foundations of materials science and engineering*. Mcgraw-Hill Publishing.

SNAME (1950). Nomenclature for treating the motion of a submerged body through a fluid. *The Society of Naval Architects and Marine Engineers, Technical and Research Bulletin*, (1950):1–5.

Soares-Ramos, E. P., de Oliveira-Assis, L., Sarrias-Mena, R., and Fernández-Ramírez, L. M. (2020). Current status and future trends of offshore wind power in Europe. *Energy*, 202:117–787.

Trubat, P. and Molins, C. (2019). Rheological damping of slender rods. *Marine Structures*, 67:102–639.

Tsetas, A., Tsouvalas, A., and Metrikine, A. V. (2021). Installation of Large-Diameter Monopiles: Introducing Wave Dispersion and Non-Local Soil Reaction. *Journal of Marine Science and Engineering*, 9(3):313.

Vugts, J. H. (2013). *Handbook of Bottom Founded Offshore Structures: Part 1. General features of offshore structures and theoretical background*, volume 1. Eburon Uitgeverij BV.

Vuik, C., Vermolen, F. J., Gijzen, M. B., and Vuik, M. (2006). *Numerical Methods for Ordinary differential equations*. VSSD.

A

WTG and substructure properties

A.1. WTG dimensions

The WTG that is taken as reference turbine in this thesis is the ‘HMC 17 MW’ turbine. This turbine does not exist in reality, but is extrapolated from existing turbines in order to prepare for the future offshore wind market. This turbine arrangement is designed by Heerema Marine Contractors, and all dimensions are internally agreed upon to be realistic for a 17 MW turbine. Figure A.1 shows some of the important global dimensions, including the location of the center of gravity.

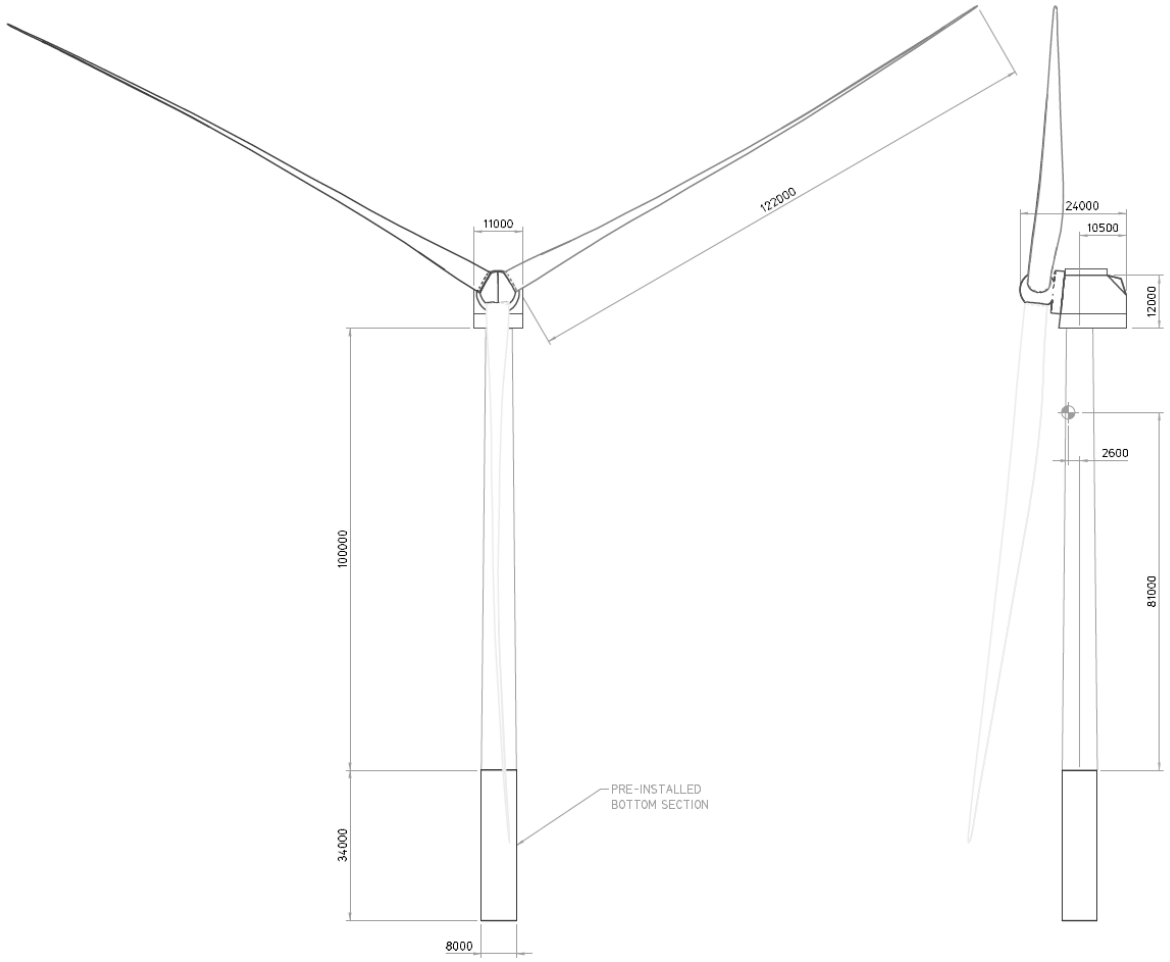

Figure A.1: HMC 17 MW reference turbine, dimensions in mm (Heerema Marine Contractors, 2021).

Table A.1: HMC 17 MW reference turbine masses.

Component	Symbol	mass [10^3 kg]
Nacelle	m_{RNA}	818
Tower		813
Blades		219
Total	m_{WTG}	1850

A.2. Flange geometry

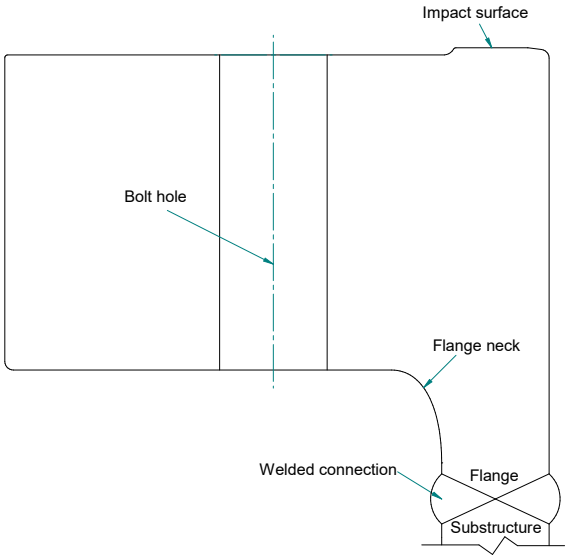

Figure A.2: Typical flange cross section.

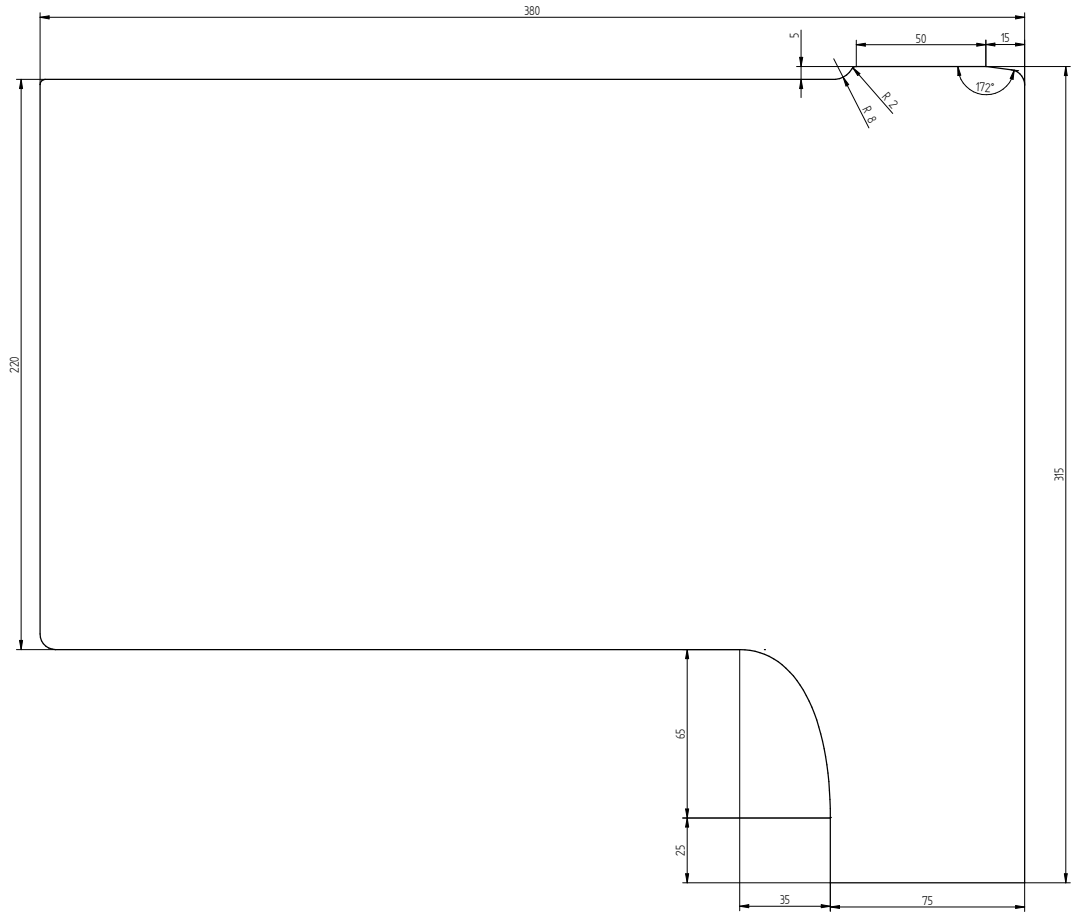

Figure A.3: Typical flange dimensions.

A.3. Material properties

The material properties of the WTG flange and substructure flange are taken from EN norms. These properties are listed in Table A.2

Table A.2: Material properties of S355 steel (British Standards Institution, 2005a).

Parameter	Symbol	Value	Unit
Yield stress	σ_y	335	MPa
Poisson's ratio	ν	0.3	-
Density	ρ	7850	kg/m^3
Young's modulus	E	210	GPa

B

Finite Difference Method

B.1. Method

The method that is utilized to solve the governing differential equations in chapter 4 and chapter 5 is called the *finite difference method* (FDM). The trick in this method is to approximate spatial derivatives numerically, for discretized elements, with so called *finite differences*. Knowledge presented in this appendix is based on the book "numerical methods for ordinary differential equations" from Vuik et al. (2006). In this thesis central differences are used, as their truncation error is smaller compared to those of forward or backward differences. According to Vuik et al. (2006), the truncation error for central differences is in the order of $\mathcal{O}(\Delta x^2)$. The purpose of approximating spatial derivatives with differences, is to write the set of partial differential equations (PDE) as a set of ordinary differential equations (ODE), where the latter is much more convenient to solve. The spatial domain needs to be discretized by introducing N nodes, so that there are N-1 elements in between those nodes. The length of one element, so the distance between two nodes, is denoted with Δx.

The advantage of the FDM compared to, for instance, the fast Fourier transform, is that it allows for the boundary conditions to be included in the system of equations. In this appendix, a full derivation of the system of equations, including the boundary conditions, is presented for the classical rod model (wave equation). Similar derivations can be performed for the other models used, such as the Rayleigh-Love rod and Euler-Bernoulli beam, but those are not presented as they would not result in fundamentally different insights. The derivation of the system of equations is done in section B.2 and the incorporation of the boundary conditions in section B.3. The expressions for the central differences are

$$\frac{\partial u_n}{\partial x} = \frac{u_{n+1} - u_{n-1}}{2\Delta x}, \tag{B.1}$$

$$\frac{\partial^2 u_n}{\partial x^2} = \frac{u_{n-1} - 2u_n + u_{n+1}}{\Delta x^2}, \tag{B.2}$$

$$\frac{\partial^3 u_n}{\partial x^3} = \frac{-u_{n-2} + 2u_{n-1} - 2u_{n+1} + u_{n+2}}{\Delta x^3}, \tag{B.3}$$

$$\frac{\partial^4 u_n}{\partial x^4} = \frac{u_{n-2} - 4u_{n-1} + 6u_n - 4u_{n+1} + u_{n+2}}{\Delta x^4}, \tag{B.4}$$

in which u_n is the longitudinal displacement in x-direction, at discrete node n with domain $n \in [0, N]$.

B.2. Equation of motion

The wave equation for the classical rod is written as

$$\frac{\partial^2 u}{\partial x^2} = \frac{1}{c_0^2}\frac{\partial^2 u}{\partial t^2}, \tag{B.5}$$

and, after substitution of the central differences it reads

$$\frac{\partial^2 u_n}{\partial t^2} - c_0^2 \frac{u_{n-1} - 2u_n + u_{n+1}}{\Delta x^2} = 0. \tag{B.6}$$

Writing down this equation for each node, a system of equations is obtained. It reads

$$\mathbf{M}\ddot{\mathbf{u}} + \mathbf{K}\mathbf{u} = 0. \tag{B.7}$$

with $\mathbf{M}$ and $\mathbf{K}$ being the mass and stiffness matrix respectively, both of size N×N. The $\mathbf{u}$ vector contains the u per node. Although not present in this equation of motion, a damping matrix $\mathbf{C}$ is as well added as it is required to incorporate the soil damping term later on. The system of equations now reads

$$\mathbf{M}\ddot{\mathbf{u}} + \mathbf{C}\dot{\mathbf{u}} + \mathbf{K}\mathbf{u} = 0. \tag{B.8}$$

The $\ddot{\mathbf{u}}$ term can be isolated, so that

$$\ddot{\mathbf{u}} = -\mathbf{M}^{-1}\left(\mathbf{C}\dot{\mathbf{u}} + \mathbf{K}\mathbf{u}\right). \tag{B.9}$$

The utilized ODE45 integrator function in MATLAB requires the system of equations to be written in state-space form, so that the second order differential equations reduces to two first order sets of differential equations. This state-space notation reads

$$\begin{bmatrix}\dot{\mathbf{u}} \\ \ddot{\mathbf{u}}\end{bmatrix} = \begin{bmatrix}\mathbf{0} & \mathbf{1} \\ -\mathbf{M}^{-1}\mathbf{K} & -\mathbf{M}^{-1}\mathbf{C}\end{bmatrix} \times \begin{bmatrix}\mathbf{u} \\ \dot{\mathbf{u}}\end{bmatrix}, \tag{B.10}$$

in which the matrices are as follows:

$$\mathbf{M} = \begin{bmatrix}1 & & 0 \\ & \ddots & \\ 0 & & 1\end{bmatrix}, \tag{B.11}$$

$$\mathbf{C} = \begin{bmatrix}0 & & 0 \\ & \ddots & \\ 0 & & 0\end{bmatrix}, \tag{B.12}$$

$$\mathbf{K} = \begin{bmatrix}K_0 & K_1 & 0 & \cdots & 0 \\ K_1 & K_0 & K_1 & 0 & \vdots \\ 0 & \ddots & \ddots & \ddots & 0 \\ \vdots & 0 & K_1 & K_0 & K_1 \\ 0 & \cdots & 0 & K_1 & K_0\end{bmatrix}, \tag{B.13}$$

with

$$K_0 = \frac{2c_0}{\Delta x^2}, \tag{B.14}$$

$$K_1 = -\frac{c_0}{\Delta x^2}. \tag{B.15}$$

From the $\mathbf{K}$ matrix it can be observed that it does not represent the equations of motion completely at the first and last row, as the nodes u_{-1} and u_{N+1} are missing. Via this, the boundary conditions will be applied, as will be explained next.

B.3. Boundary conditions

So called 'ghost' nodes are introduced to implement the boundary conditions. These ghost nodes (u_{-1} and u_{N+1}) are not existent in reality, but they will be implemented to mathematically arrive at an expression that both; does not contain the ghost node anymore, and implements the boundary condition. Not all boundary conditions will be written out in this appendix, but solely those for the RNA mass and the soil conditions. First, the RNA mass boundary condition is derived. The boundary condition including the RNA mass as inertia at the top (derived in Equation 4.4), that is to say at u_0, can be written implementing central differences as

$$-EA\frac{u_1-u_{-1}}{2\Delta x}-m_{RNA}\ddot{u_0}=0. \tag{B.16}$$

Via this relation, the ghost node u_{-1} can be isolated. This reads

$$u_{-1}=u_1-\frac{2\Delta x}{EA}m_{RNA}\ddot{u_0}, \tag{B.17}$$

which is used to substitute where the ghost node u_{-1} is required. Similarly the boundary conditions (derived in Equation 4.6) at the bottom of the substructure u_N are derived. This results in the boundary condition

$$-EA\frac{u_{N+1}-u_{N-1}}{2\Delta x}-k_s u_N-c_s\dot{u}_N=0, \tag{B.18}$$

which results in the expression for the ghost node to be

$$u_{N+1}=u_{N-1}-\frac{2\Delta x}{EA}k_s u_N-\frac{2\Delta x}{EA}c_s\dot{u}_N. \tag{B.19}$$

Implementing these on the first and last row of the $\mathbf{M}$, $\mathbf{C}$ and $\mathbf{K}$ matrices gives the matrices including the boundary conditions. For the first row, the implementation is demonstrated. The equation of the first row of the stiffness matrix $\mathbf{K}$ reads

$$K_1u_{-1}+K_0u_0+K_1u_1=0. \tag{B.20}$$

Substituting u_{-1} as just derived yields

$$-\frac{2c_0}{EA\Delta x}m_{RNA}\ddot{u}_0+K_0u_0+2K_1u_1=0, \tag{B.21}$$

from which the inertia term ends up in the mass matrix $\mathbf{M}$, and not in the stiffness matrix $\mathbf{K}$. Performing similar derivations for the other conditions results in the following matrices that include the boundary conditions.

$$\mathbf{M}=\begin{bmatrix}1-\frac{2c_0}{EA\Delta x}m_{RNA} & 0 & \cdots & 0\\ 0 & 1 & & \vdots\\ \vdots & & \ddots & 0\\ 0 & \cdots & 0 & 1\end{bmatrix}, \tag{B.22}$$

$$\mathbf{C}=\begin{bmatrix}0 & & & 0\\ & \ddots & & \\ & & 0 & 0\\ 0 & & 0 & -K_1\frac{2\Delta x}{EA}c_s\end{bmatrix}, \tag{B.23}$$

$$\mathbf{K}=\begin{bmatrix}K_0 & 2K_1 & 0 & \cdots & \ddots\\ K_1 & K_0 & K_1 & 0 & \vdots\\ 0 & \ddots & \ddots & \ddots & 0\\ \vdots & 0 & K_1 & K_0 & K_1\\ 0 & \cdots & 0 & 2K_1 & K_0+\frac{2c_0}{\Delta xEA}k_s\end{bmatrix}. \tag{B.24}$$

All boundary conditions as presented in this thesis are implemented similarly. The boundary conditions for the transverse vibrations (Euler-Bernoulli beam theory) require a lot more work to be implemented, as two boundary conditions are required per boundary or interface. Consequently, two ghost nodes are existent and implementing the boundaries properly requires quite some substitutions, although in essence similar to the demonstrated example. Also the moment and shear as imposed at the interface in the oblique impact global model are implemented following this procedure. Moreover, the implementation of the Rayleigh-Love rod theory, and the variable area require more work, as their equations of motion are significantly more complex.

The spatial part is now defined properly. For the temporal part, two initial conditions need to be defined. One condition is the initial velocity of the WTG, which is non-zero for $0 \leq x \leq L_1$ where L_1 is the length of the turbine, as defined earlier. The initial velocity condition reads:

$$\frac{\partial u(0,t)}{\partial t} = \begin{cases} V_i & 0 \leq x \leq L_1 \\ 0 & L_1 < x \leq L \end{cases} \tag{B.25}$$

where $L = L_1 + L_2$. The second initial condition is that of no initial displacement, written as $u(x,0) = 0$.

C

Finite Element Method

The selected method to validate the results obtained from the constructed models with, is the finite element method (FEM). This method is used to numerically solve differential equations. The model that is created consists of finite elements, constructed using spatial discretization, which is implemented by creating a so-called 'mesh'. FEM is commonly practised in the field of (structural) engineering, particularly for static problems. The problem under consideration in this thesis is dynamic, thus a dynamic FEM analysis is required to validate the dynamic, transient behaviour. Consequently, the analysis will be explicit, whereas for static problems, implicit solving is commonly used. The FEM software that is practised in this thesis is Dassault Systemes® Simulia ABAQUS 2021, hereafter called Abaqus. The relevant settings that are implemented, are presented in subsection C.1.1 and subsection C.2.1, for the collinear impact and oblique impact model respectively.

Generally speaking, results tend to be more accurate when the mesh size is decreased, but this automatically increases the computational time considerably. Therefore, it is common practice in FEM to perform a mesh convergence study. The objective of such a study is to arrive at a mesh size which is both; rough enough to minimize computational time, and fine enough to show converged stress, that is to say that an even finer mesh does not show substantial different results. This is only possible when a decreasing mesh size indeed does converge towards a value, where this is not necessarily always the case.

C.1. Collinear impact

The FEM model constructed to perform the cross-check with the collinear impact model is an axi-symmetric model. The general settings of this FEM model are presented in subsection C.1.1 for the case in which the structures are modelled as tubulars. Unless mentioned otherwise, presented settings concern the tubular model. The tubular (also referred to as shell) model is chosen to perform the cross-check with, as it represents the actual geometry of a monopile and WTG tower most accurate. However, also a FEM model is constructed in which both WTG tower and substructure are modelled as rod, because those are more accurately described by the classical and Rayleigh-Love rod theory. The distinctions of these models are discussed in subsection C.1.2. Subsequently, mesh convergence is investigated and shown in subsection C.1.3 and subsection C.1.4.

C.1.1. General settings

The modelling space in which the part is constructed is axi-symmetric. The part type is deformable, with solids as shape. The base feature is revolution. For the material, the steel is modelled with a uniformly distributed density of 7850 kg/m^3. The elasticity is isotropic with a Young's modulus of 210 GPa and a Poisson's ratio of 0.3. The impact consists of three steps, the first being the initial step, the second the velocity step and the last the impact step itself. The latter two are of the type dynamic and explicit and the first of type initial. The interaction between tower and substructure is defined with an explicit surface-to-surface contact constraint. The mechanical constraint formulation is the penalty contact method, and the sliding formulation is finite sliding. Two load boundary conditions are implemented, the first one being the initial velocity condition, which defines that the tower has an initial velocity of V_i.

The second load describes the soil conditions at the bottom tip of the substructure. For the case in which a fixed boundary is assumed, a full displacement and rotation fix is imposed. For the case in which soil damping and stiffness is considered, a spring is employed, solely in vertical direction, ensuring that other degrees of freedom are still fixed. The spring has both damping and stiffness properties.

The tower and substructure are meshed with a global mesh seed of 0.1 m, which is validated with the global stresses obtained from the collinear MATLAB models, in order to ensure an appropriate mesh. A seed edge is applied over the thickness of the tubular wall, to ensure there are three elements over the thickness of the wall. This causes the elements size in radial direction to be 25 mm in the tubular model. This mesh is also illustrated in Figure C.1. The model is run via a job. This job has the settings; Abaqus explicit precision is double analysis only, and the nodal output precision is full. Data is extracted from the simulation using history output, and has a sampling frequency of 200 kHz.

C.1.2. Models

Several distinct models are constructed in using FEM. As is explained in subsection 4.4.1, the chosen model to perform the cross-check with is the tubular FEM model. For this model the settings were presented. The main reason why this is the governing FEM model, is that it represents the actual geometry of a monopile and WTG tower the most accurate. On the other hand, the analytical models assume the structures to be rods. For this reason, also a FEM model is constructed taking into account the geometry of a rod, in order to compare with both the FEM tubular model and the analytical models (classical rod and Rayleigh-Love rod). Moreover, distinct models are constructed both considering and disregarding lateral inertia (via Poisson's ratio) to compare with both the analytical classical rod and Rayleigh-Love rod theory.

It is of importance to set the cross-sectional area equal to the tubular model, as this would result in equal impact force. Therefore the rod has a diameter corresponding to the same cross-sectional area as the tubular geometry. For the case in which no Poisson's ratio, thus lateral inertia is assumed (corresponding to the classical rod theory), this is satisfactory. However, for the case in which it is considered (corresponding to the Rayleigh-Love rod), also the rotational moment of inertia influences the stress occurring. This rotational moment of inertia is not only dependant on the cross-sectional area, but also on the radius of gyration which will be considerably different for the FEM rod compared to the Rayleigh-Love rod theory. As a consequence, the FEM rod model including lateral inertia does not fully correspond to the Rayleigh-Love analytical model, as the latter's lateral inertia characteristics are compliant with an actual tubular structure.

C.1.3. Convergence for global stress

Global convergence of the mesh does not have to be further investigated, because the results of the FEM model with 0.1 m mesh size complies with the results obtained from the simplest collinear impact model. That is to say, the collinear impact model with fixed and free boundary conditions. The FEM results obtained from this model fully comply with the results obtained from the collinear impact model, and the theory. All occurring effects are easily explained. This ensures full confidence in the results obtained in this simplest case, allowing it to function as a benchmark. These results are shown in Figure 4.2, where also the compliance of the FEM models is demonstrated. It should be noted that this full confidence in the mesh of the FEM model is only valid for global stress. This changes when detailed results at the interface are considered, as will be explained below.

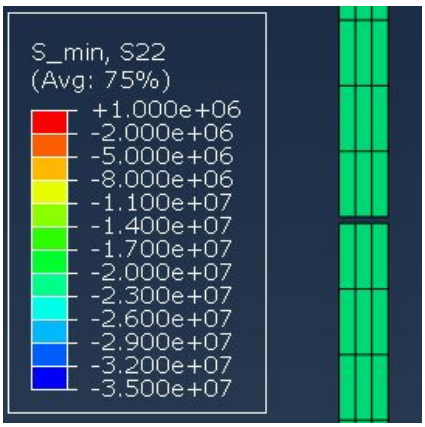

Figure C.1: Global mesh with a size of approximately 100 by 25 mm. S_min represents the minimum stress in vertical direction per element for the initial impact (reflections excluded) in Pa.

C.1.4. Convergence for local stress

A convergence study is performed for the stress close to the interface. Goal of this study is not so much about the occurring stress at the interface for the collinear impact, but more about investigating what mesh size is capable of describing local stress at a specific location through the thickness of the wall. This is of importance for the contact indentation stress in the oblique impact model, in which a peak stress at

a specific location is of interest. Consequently, the mesh close to the interface will be varied in order to arrive at a mesh size that shows converged results. Considering their redundancy, reflections are excluded in this mesh convergence study.

As discussed in previous section, results describing the simplest collinear impact model are confidently accurate. This will act as a benchmark in this convergence study. According to the collinear impact model, the peak impact stress at the interface should be in the order of 26 MPa. This can as well be observed in Figure 4.2. Let us start with the results for the global mesh, which means no finer mesh is applied close to the interface. Figure C.1 shows the results. The stress that is shown is the maximum stress occurring per element, in a time-span without any reflections (0.01 s). It is observed that the stress at the interface is in the order of 20-23 MPa, which is significantly lower than the benchmark of 26 MPa. Therefore, a finer mesh is required. Figure C.2 shows a finer meshing of the substructure.

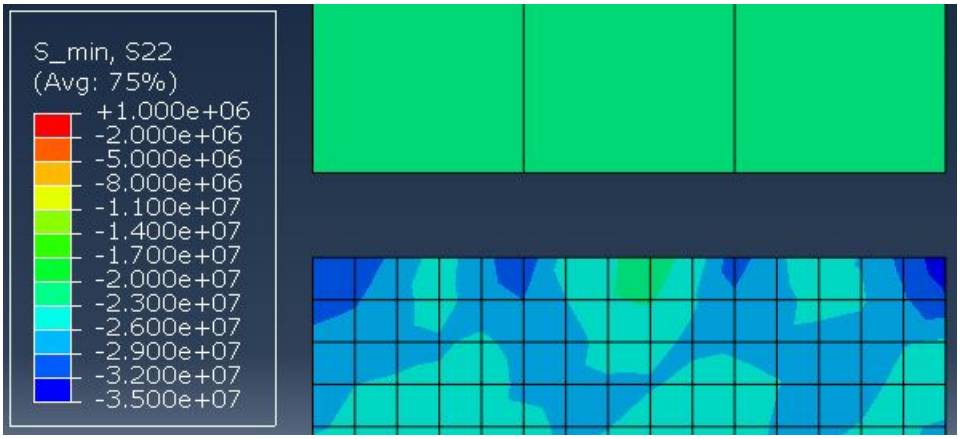

(a) Substructure 5 mm mesh.

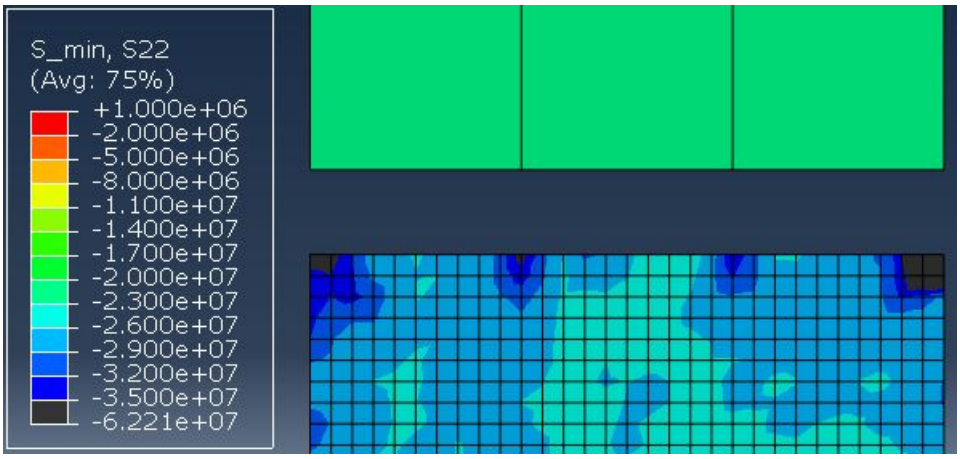

(b) Substructure 2.5 mm mesh.

Figure C.2: Minimum stress per element occurring in a time window of 0.01 s. Decreased mesh size for the substructure.

From these results, it is concluded that a decrease in mesh size does improve the occurring stress, because on average, the occurring stress at the interface of the substructure is now in the order of 27 MPa. However, another problem arises, being a non-realistic stress distribution over the wall thickness. Around the location where the nodes from the tower mesh will contact the substructure, peak stresses of 60 MPa arise. To solve this problem, the tower mesh needs to be meshed finer accordingly. Figure C.3 shows results obtained for equal meshing of tower and substructure. For the sake of a clear sight of the stress, the meshing itself is not shown anymore.

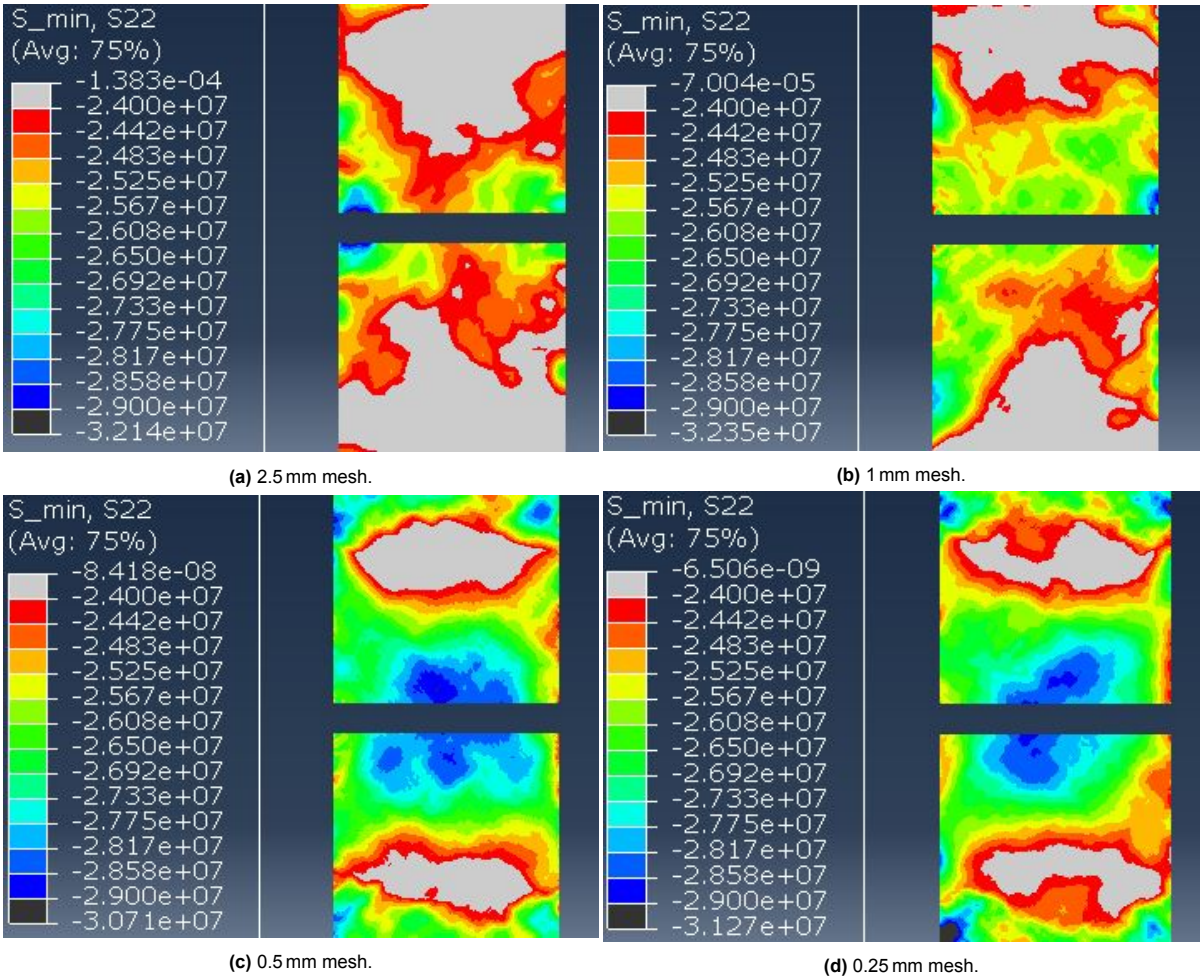

(a) 2.5 mm mesh.

(b) 1 mm mesh.

(c) 0.5 mm mesh.

(d) 0.25 mm mesh.

Figure C.3: Minimum stress per element occurring in a time window of 0.01 s for several mesh sizes. Convergence clearly starts from a mesh size of 0.5 mm.

It can be observed that the 0.5 mm and 0.25 mm mesh converge notably, within a range of approximately 1 MPa. The observation of slightly higher stresses closer to the center of the wall thickness can be explained. Both the 0.5 mm and 0.25 mm mesh show a slightly higher peak stress close to the interface in the center of the material than towards the edge. This can be explained by the fact that material closer to the center is more 'trapped' by material at both sides, enabling it to act more stiff since it can less easily deform towards the sides. The material closer to the edge can more easily deform towards the outside, as less material is in place to resist this deformation.

Figure C.4 shows a comparison between the classical rod stress, the Rayleigh-Love rod stress and the stress of the top row of elements of the substructure from the considered meshes. The stress in the top row of elements is obtained by averaging all elements. All top row averaged stresses for the considered mesh sizes result in similar curves, which are close to the classical rod stress for a Δx of 0.1 m. As explained in subsection 5.2.3, the slope of the stresses obtained from the wave equation and RL model are dependent on Δx due to the numerical solution method. From Figure C.4, it can be concluded that all considered mesh sizes, result in converged stress averaged over the top row of elements. Figure C.3 shows, however, that particularly the 2.5 mm and 1 mm mesh show considerable different results compared to the 0.5 mm and 0.25 mm mesh, when the stress is not averaged over the wall thickness.

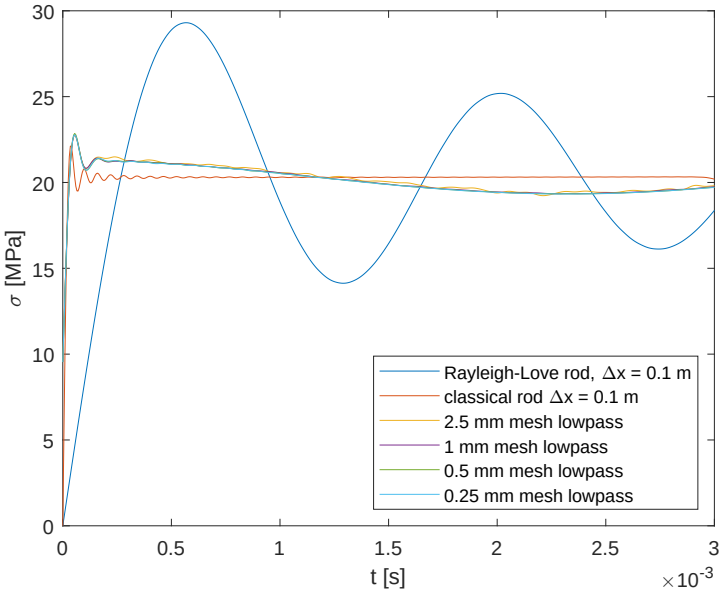

Figure C.4: Mesh comparison with classical and Rayleigh-Love rod. Frequencies above 1500 Hz are filtered out of the FEM results, using a lowpass filter in MATLAB.

Concluding, the 0.5 mm mesh is considered converged sufficiently well. In order to first get the oblique impact model run correctly with minimal run time, a rougher mesh of 5 mm is used. Unfortunately, it will be determined in subsection C.1.3 that a mesh size of 0.5 mm is not workable, and a rougher mesh of 1 mm is used as finest mesh.

C.2. Oblique impact

The FEM model that is constructed to simulate the oblique impact with will be three-dimensional. In order to minimize the amount of elements, a so-called 'half-model' is created with a symmetry constraint applied on the vertical cross-section of the structures. This is justified by the fact that, as explained in chapter 1, there will be one rotation about one axis, so that there can be constructed a vertical symmetry-plane. The half model constructed to validate the oblique impact with, deviates from the axi-symmetric model. In subsection C.2.1 it is explained where the settings differ from the axi-symmetric model, and the progress towards a trustworthy meshing is presented in subsection C.1.3.

C.2.1. General settings

The general settings used for the oblique impact FEM half model are for most part identical to those in the collinear impact FEM axi-symmetric model as presented in subsection C.1.1. Settings that deviate will be explained. The modelling space of the parts is now 3D instead of axi-symmetric, and for the biggest part, the tower and substructure are now constructed of shell shape base feature instead of solids. The area close to the interface (within 8 m height) remains constructed of solids. Additional interactions are applied, being a shell-to-solid constraint to fix the shell structures to the solid structures. The different solids parts, used to easily variate mesh size, are tied to one another using a tie constraint. Where the FEM model for the collinear impact is axi-symmetric, this half model has one symmetry plane. This symmetry is imposed using a symmetry boundary condition in the direction normal to the symmetry plane, applied on all surfaces located on the symmetry plane. The meshing of the parts will be explained in subsection C.2.2.

C.2.2. Mesh for contact model

In order to further limit computational time of the model, not only solid elements are used. Shell elements are applied everywhere except within 8 m height from the interface. The solid part and shell part are tied together using a shell-to-solid constraint. This constraint ties nodes from the solids to the closest nodes from the shell elements. It is shown that this shell-to-solid constraint does not (marginally at maximum) influence the propagating stress signal, although it can reflect high-frequency distortion.

This distortion is shown in Figure C.5, where it can be clearly observer that high-frequency distortion only exists when a reflection of the shell-to-solid constraint arrives.

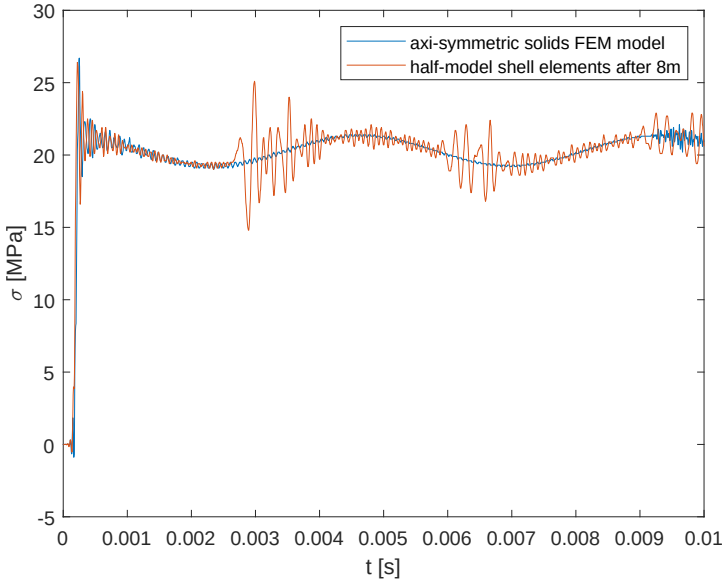

Figure C.5: High-frequency distortion reflected by shell-to-solid constraint. Stress is obtained as cross-sectional average over elements at 1 m below the interface. The time between incident stress wave and distortion is around 0.0025 s, which means a travelled distance of 13 m considering the stress wave speed of approximately 5200 m/s.

This distortion is a reason to keep a considerable distance between interface and the shell elements. However, as will be shown later, this distortion is not found back into the results obtained for the stress in one element for the oblique impact case. Furthermore, Figure C.5 also illustrates that the 3D half-model gives very similar results as the axi-symmetric model, which is logically expected.

Another method to reduce the number of elements, without using shell elements closer to the interface, is by applying a rougher mesh further away from the interface. This is often done by applying biased meshing, so that the mesh gradually gets finer. As this proved to be inconvenient in three dimensions, a solid-to-solid tie constraint will be used to tie different part to each other. Different parts, after all, allow for part-specific meshing, without the need for 3D mesh biasing. A marginal distortion can be observed for the solid-to-solid tie constraint, as is shown in Figure C.6, but this can be considered negligible. Be aware that the distortion from the shell-to-solid constraint is still featured in the figure.

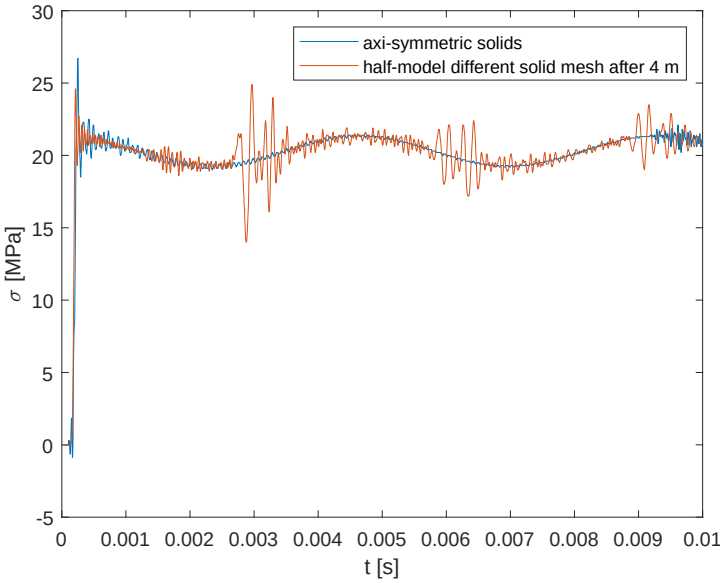

Figure C.6: Distortion reflected by solid-to-solid tie constraint between two parts with different mesh size. Stress is obtained as cross-sectional average over elements at 1 m below the interface. The time between incident stress wave and distortion is around 0.0012 s, which means a travelled distance of 6 m considering the stress wave speed of approximately 5200 m/s. This 6 m corresponds to the distance between location of sampling and the location of the solid-to-solid constraint, which is located 4 m below the interface.

Based on these results, it is concluded that using different parts in order to reduce mesh size close to the impact surrounding is justified. Figure C.7 shows an example of different parts, with decreased mesh size closer to the impact area.

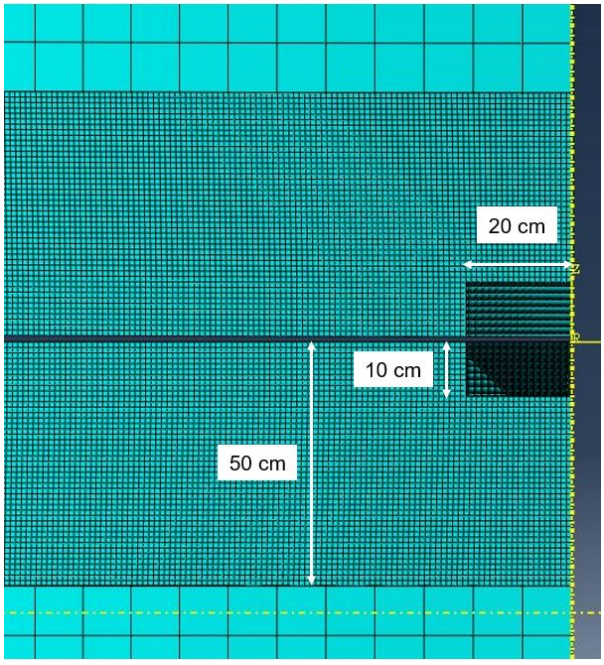

Figure C.7: Tied parts with different mesh size.